Technische Universiteit Eindhoven University of Technology

Department of Mechanical Engineering
Dynamics and Control Research Group

Dynamic behavior of thrust air bearings

R.H.M. Franssen

D&C 2016.011

Master's thesis

Coaches:	dr. ir. R.H.B. Fey[2]	Commitee:	prof. dr. H. Nijmeijer[2]
	P. de Jong, MSc[1]		dr. ir. R.H.B. Fey[2]
	dr. ir. W. Potze[1]		prof. dr. J.G.M. Kuerten[3]
			P. de Jong, MSc [1]
			dr. ir. W. Potze[1]

Supervisor: prof. dr. H. Nijmeijer[2]

[1]   Philips Innovation Services
     Mechatronics Technologies

[2]   Eindhoven University of Technology
     Department of Mechanical Engineering
     Research group Dynamics & Controls

[3]   Eindhoven University of Technology
     Department of Mechanical Engineering
     Research group Process Technology

Eindhoven, February 2016

Abstract

Air bearings are one of the key components in high precision systems and their function is to allow relative motion with reduced friction and wear. Several instances in literature describe the model of a journal bearing that is valid for large displacements. However, little is known on the modeling of large displacement behavior of thrust air bearings. This study aims to develop and validate a model that can be used to describe the large displacement behavior of thrust air bearings subjected to a time dependent external force.

The Reynolds equation is used to model the thin lubrication film and this is coupled with a dynamic model based on Newton's second law to obtain the thrust air bearing model. The solution of this model is obtained by first solving simplified versions of the model and subsequently increasing the difficulty. Eventually a solution of the thrust air bearing model is found by using the finite difference method and the Crank-Nicolson method.

Static measurements on an experimental setup show a large deviation of 5 μm compared with the model. This is probably caused by difficulties encountered in measuring the gap height due to bearing pad roughness, stiffness and tilt. Further there is an uncertainty due to an unknown influence of bearing tilt on the load carrying capacity. The measured resonance in the frequency response measurements coincides well. In this measurement it is seen that the fixtures holding the displacement sensors are not stiff enough, causing a deterioration of the measurement signal for certain frequencies. The measured maximum amplitude in the impulse response shows a small error. It is tried to validate the step response but no good measurement results are obtained due to an unwanted interaction between the hand of the experimenter and the air bearing setup.

The static load carrying capacity is compared with the results of an Ansys FEM model and shows a good agreement. Comparison of the developed model with a model that uses interpolated dynamic coefficients shows a small error in the maximum impulse response and is overall in a good agreement.

Considering the uncertainty due to error sources in the experimental setup it may be concluded that the developed model is able to describe the thrust air bearing gap height behavior. Further, the difference between the developed model and the interpolated coefficients model shows a good agreement for the analyses conducted in this study. Based on this results it may be concluded that both models can be used to study the air bearing gap height behavior. A better validation of the developed model can be obtained by investigating the influence of, or removing, the error sources identified in the experimental setup.

Acknowledgements

Contents

List of Figures

List of Tables

List of Symbols

Roman

Symbol	Description	Unit
A	Cross sectional area	$[\text{m}^2]$
A_{gap}	Cross sectional area of bearing gap after orifice edge	$[\text{m}^2]$
A_{in}	Cross sectional area of bearing gap at orifice edge	$[\text{m}^2]$
A_o	Cross sectional area of orifice	$[\text{m}^2]$
$\underline{c}_{hom}$	Vector containing coefficients for the homogeneous discretized problem	
$\underline{c}_{part}$	Vector containing coefficients for the particular discretized problem	
d	Dynamic damping coefficient	$[(\text{Ns})/\text{m}]$
$F_a b$	Force generated by the fluid film on the bearing surface	$[\text{N}]$
F_{ex}	Externally applied force	$[\text{N}]$
F_g	Gravitational force	$[\text{N}]$
f_i	Components of the prescribed body force, $i = x, y, z$	$[\text{m/s}^2]$
F_{part}	Particular force due to particular pressure distribution	$[\text{N}]$
$\underline{f}$	System of equations	
$\vec{F}$	Force vector	$[\text{N}]$
g	Gravitational constant	$[\text{m/s}^2]$
h	Air bearing gap height	$[\text{m}]$
h_g	Minimum gap height	$[\text{m}]$
h_r	Gap height under recess	$[\text{m}]$
I	Number of intermediate intervals in space	$[-]$
J	Number of intermediate intervals in time	$[-]$
bfJ	Jacobian matrix	
K	Dynamic stiffness	$[\text{N/m}]$
k	Dynamic stiffness coefficient	$[\text{N/m}]$
M	Air bearing mass	$[\text{kg}]$
$\dot{m}$	Mass flow	$[\text{kg/s}]$
$\dot{m}_{gap}$	Mass flow under air bearing directly after orifice edge	$[\text{kg/s}]$
$\dot{m}_{in}$	Mass flow under air bearing directly at orifice edge	$[\text{kg/s}]$
$\dot{m}_o$	Mass flow directly after orifice	$[\text{kg/s}]$
p	Pressure	$[\text{N/m}^2]$
p_a	Ambient pressure	$[\text{N/m}^2]$
$p_{i,j}$	Pressure at spatial grid point i and time grid point j	$[\text{N/m}^2]$
p_o	Pressure under orifice	$[\text{N/m}^2]$
p_s	Supply pressure	$[\text{N/m}^2]$
$\underline{p}_{hom}$	Homogeneous pressure distribution	$[\text{N/m}^2]$
$\underline{p}_{part}$	Particular pressure distribution	$[\text{N/m}^2]$
p_w	Pressure under slider bearing	$[\text{N/m}^2]$

Q	Lubricant flow	[kg/s]
r	Cylindrical radial component	[−]
r_i	Radius at spatial grid point i	[m]
R_1	Orifice radius	[m]
R_2	Outer bearing radius	[m]
$\mathbf{R}_{hom}$	Matrix containing coefficients for the homogeneous discretized problem	[−]
$\mathbf{R}_{part}$	Matrix containing coefficients for the particular discretized problem	[−]
R_e	Reynolds number	[−]
R_s	Specific gas constant	[J/(kgK)]
R_x	Reynolds number in x direction	[−]
R_y	Reynolds number in y direction	[−]
R_z	Reynolds number in z direction	[−]
S	Stiffness	[N/m]
t	Time	[s]
T	Temperature	[K]
$T_{i,j}$	Stress tensor component with $i = x, y, z$ and $j = x, y, z$	[N/m^2]
u	Velocity in x direction	[m/s]
U_0	Velocity of bearing surface at $z = 0$ in x	[m/s]
U_h	Velocity of bearing surface at $z = h$ in x	[m/s]
u_r	Radial fluid velocity	[m/s]
V	Volume	[m^3]
v	Velocity in y direction	[m/s]
V_0	Velocity of bearing surface at $z = 0$ in y	[m/s]
V_h	Velocity of bearing surface at $z = h$ in y	[m/s]
$\underline{v}$	Velocity vector	[m/s]
$\vec{V}$	Body velocity vector	[m/s]
w	Velocity in w direction	[m/s]
W	Load carrying capacity	[N]
W_0	Velocity of bearing surface at $z = 0$ in z	[m/s]
W_a	Load carrying capacity due to ambient pressure	[N]
W_{abs}	Load carrying capacity under air bearing surface	[N]
W_h	Velocity of bearing surface at $z = h$ in z.	[m/s]
W_{ih}	Load carrying capacity under orifice	[N]
W_{num}	Numerical load carrying capacity	[N]
x	Cartesian x coordinate	[−]
$\underline{x}$	Position vector	[m]
$\vec{x}$	Air bearing position vector	[m]
y	Cartesian y coordinate	[−]
z	Cartesian and Cylindrical z coordinate	[−]

Greek

Symbol	Description	Unit
ε	Eccentricity in journal bearing, numeric stop criterion	[m]
κ	Adiabatic expansion coefficient	[−]
μ	Viscosity	[kg/(ms)]
$\nabla(\cdot)$	Gradient operator	

$\nabla \cdot (\cdot)$	Divergence operator	
ω	Frequency or rotational velocity	[rad/s]
ρ	Density	[kg/m^3]
σ_s	Squeeze number	[−]
θ	Cylindrical azimuthal coordinate	[−]

Sub/Superscripts

Symbol	Description
$(\cdot)_a$	Subscript to denote ambient environment
$(\cdot)_{ad}$	Subscript to denote additional mass
$(\cdot)_b$	Subscript to denote bushing
$(\cdot)_{cs}$	Subscript to denote counter surface mass
$(\cdot)_g$	Subscript to denote linear guide mass
$(\cdot)_{in}$	Denotes air bearing gap inlet at orifice
$(\cdot)_o$	Subscript to denote orifice
$(\cdot)_r$	Subscript to denote recess or radial component
$(\cdot)_s$	Subscript to denote supply or Shaft
$(\cdot)_w$	Subscript to denote wedge
$\overline{(\cdot)}$	Dimensionless version of $(\cdot)$
$(\cdot)_*$	Denotes factor to make $(\cdot)$ dimensionless
$(\cdot)_\theta$	Azimuthal component of vector $(\cdot)$
$(\cdot)_z$	Height componont of vector $(\cdot)$

Chapter 1

Introduction

One of the key components in high precision systems are thrust air bearings. The main function of air bearings is to enhance a relative motion and reduce friction between two solid surfaces [37]. The two solid surfaces are not in contact due to an air film that is maintaining a clearance between them. If the air bearing is subjected to a temporarily external force it is important that the two surfaces do not touch in order to maintain the smooth motion, the low friction and avoid damage to the smooth bearing surfaces. Further, to guarantee sufficient accuracy of the high precision system, it is desirable that the clearance between the two surfaces quickly recovers to the original height. In order to guarantee that the clearance between the bearing surfaces is maintained for a certain load, the dynamic behavior of the bearing gap height is modeled in the design process of the air bearing.

A general approach to assess the dynamic behavior of air bearings subjected to external forces is to compute the transient response with the use of the dynamic coefficients of the air bearing based on the Reynolds equation for lubricant flow [9]. However, the dynamic coefficients are obtained by linearizing the problem which means that the computed solution is only valid for small displacements around the equilibrium clearance of the bearing. The change in gap height is often larger than the valid region of this linear model. Therefore, this model is not appropriate to assess if the bearing surfaces will touch.

Another modeling method that is used during the design process, is to use the dynamic coefficients over a range of equilibrium gap heights. At the initial equilibrium gap height of a transient simulation a valid set of dynamic coefficients is selected. If the gap height of the air bearing is outside the valid region of that particular set of dynamic coefficients, dynamic coefficients belonging to the newly calculated gap height are used [22]. A variant of this model is to interpolate the computed dynamic coefficients to estimate a valid set of coefficients at every computed air bearing height during the simulation. The main advantage of this model is that the computation time of a transient air bearing clearance solution is fast compared to solving the non-linear Reynolds equation [22]. A disadvantage is that still a simplified linear problem is used and a linearization error will be made with this method compared to the non-linear problem. The most accurate solution can be obtained by solving a model based on the non-linear Reynolds equation which generally needs a longer computation time.

A model that uses multiple sets of dynamic coefficients to simulate the air bearing clearance for large displacements has been intensively studied for journal air bearings [22], [23], [24]. Also, much literature can be found on the modeling and solving of a non-linear model for journal air bearings subjected to large displacements [17], [1]. However, little is known about the modeling of thrust air bearings using the non-linear Reynolds equation and the large displacement gap height behavior of these bearings. Furthermore, it is unknown how large the approximation error is of a model that uses interpolated dynamic coefficients compared to a model that utilizes the non-linear Reynolds equation. This leads to the following objectives for this thesis:

1. Develop a mathematical model to determine the time dependent bearing gap in the air

---

bearing when the applied load changes from a steady-state to a time dependent load, using the transient non-linear Reynolds equation for lubricant flow.

2. Extend the developed mathematical model with the effect of the inertia of the bearing parts on their motion.

3. Validate the developed model experimentally for static loads, harmonic loads, impulsive loads, and step loads.

4. Assess the accuracy of the approximation method that uses interpolated dynamic coefficients for an impulsive load case by comparing the response with the response based on the full non-linear model, see objectives 1 and 2.

This report has the following outline. Chapter 2 discusses air bearings in general, from classification and application to modeling and stability assessment. Chapter 3 focuses on the derivation of the thin film approximation to model the lubricant fluid film in a thrust bearing. The resulting equation is the well-known Reynolds equation often used in modeling lubrication problems. This model is experimentally validated in chapter 5 for a static, a step and an impulse load case including the frequency response. Chapter 6 correlates the results obtained by the presently proposed non-linear air bearing model with those obtained by several other models, such as the model that uses linearized dynamic bearing coefficients. Finally, in chapter 7, the conclusions and recommendations are presented.

Chapter 2

Air bearings

Air bearings are used in many applications, each with its own design. For the design of air bearings different modeling techniques are used to determine the load carrying capacity and stability. This chapter gives an overview of the air bearing applications and designs. Also an overview is given of several air bearing modeling methods including the stability analyses. Finally, the air bearing configuration that is investigated in this study is presented together with a global overview of the developed simulation model. Appendix A presents the literature search used in this chapter.

2.1 Applications and design

Air bearings are part of the fluid film bearing family that uses gaseous, liquid, or solid lubrication films. Fluid film bearings are used to allow a smooth relative motion between two solid surfaces with reduced friction and wear [37]. This reduction in friction and wear is caused by the lubrication layer between the two moving parts. If the lubrication layer is generated due to the relative motion of the two bearing surfaces, then the bearing is called hydrodynamic. Hydrostatic bearings however, use an external lubrication source to create a lubricant layer and can carry loads even if the two bearing surfaces do not experience a relative motion.
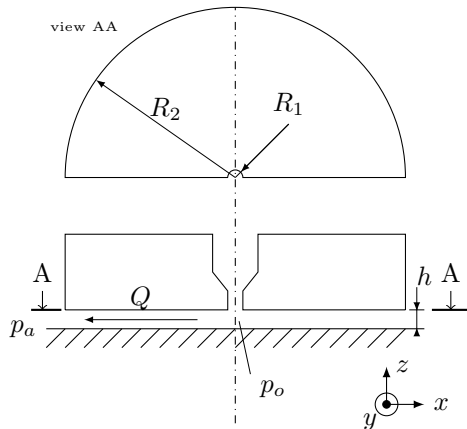
Figure 2.1: Schematic drawing of a hydrostatic thrust bearing.
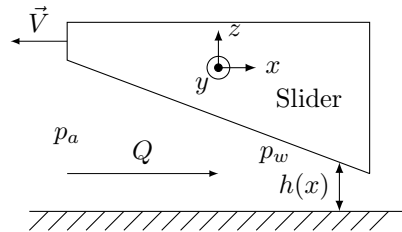
Figure 2.2: Schematic drawing of a hydrodynamic thrust bearing.

Hydrostatic thrust bearings are bearings that allow a translational motion while carrying a load. Such a bearing has for example one or multiple supply holes that supplies the lubricant to the bearing gap with pressure p_o, as shown in Figure 2.1. Due to the pressure difference between the

---
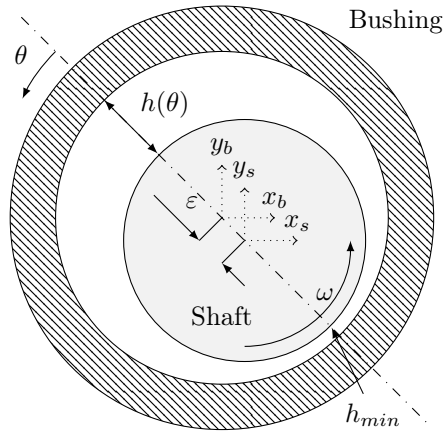
Figure 2.3: Schematic drawing of a hydrodynamic journal bearing.
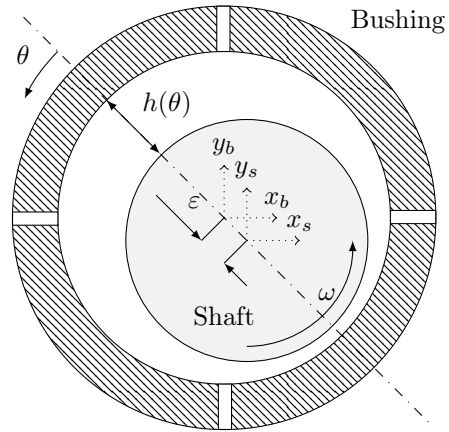
Figure 2.4: Schematic drawing of a hydrostatic journal bearing.

orifice pressure p_o and the ambient pressure p_a, a lubricant flow Q and pressure profile will exist underneath the bearing. The increased pressure under the bearing pad exerts a force that provides the bearing a load carrying capacity [28]. These types of bearings are often used in high precision systems.

Slider bearings are hydrodynamic bearings that allow a in-plane translation and have a wedge form as depicted in Figure 2.2. The wedge forces the lubricant into a small gap due to the relative motion between the bearing surfaces. Because the lubricant is forced under the wedge an increased pressure p_w will occur that exerts a force on the slider [50]. This principle is applied in the design of hard disk drives (HDD) read heads to ensure that the read head hovers above the hard disk [11] [41] [16] [40]. Another hydrodynamic linear bearing is the squeeze film bearing. This type of air bearing has a flexible bearing surface that can be actuated in a vibrating motion, which causes a time averaged positive pressure along the bearing pad [25] [48] [39].

Journal bearings allow rotational motion and carry loads perpendicular to the rotational axis. Hydrodynamic journal bearings consist of a circular bushing and shaft where the center axes of these components are generally aligned with a small eccentricity ε as shown in Figure 2.3. Due to the eccentricity, the bearing gap varies along the shaft circumference with the minimum gap in the direction of the eccentricity. The relative motion between shaft and bushing pressurizes the lubricant in the minimum gap causing a load carrying capable force [37]. These types of bearings are for example used in micro gas turbines [20].

Hydrostatic journal bearings are used if hydrodynamic bearings are not able to support the load, a precise radial position of the bearing is needed or to reduce bearing instabilities [43]. These bearings have lubrication sources distributed along the circumference of the bearing surface as shown in Figure 2.4 [1].

Figure 2.5 depicts several thrust air bearing design variations that increase the bearing stiffness or load carrying capacity. Figure 2.5 (a) shows a thrust bearing with a conical bearing gap. This conical gap gives a higher pressure in the bearing gap and an increase in load carrying capacity and stiffness. Figure 2.5 (b) depicts a porous air bearing that has a porous surface underneath the bearing that can be seen as a surface with an infinite number of orifices. This surface is able to create stiffness in the bearing but also to increase the load carrying capacity because the air is supplied all over the surface resulting in an higher pressure distribution.

Figure 2.5 (c) shows a thrust bearing with orifice and recesss. The orifice is responsible for the creation of stiffness in the bearing because it makes the pressure under the orifice p_o a function of the bearing gap h_r. Stiffness is defined as a change in force over a change in distance

$$S = \frac{dF}{dz} = \frac{dF_{ab}}{dh_r} \tag{2.1}$$
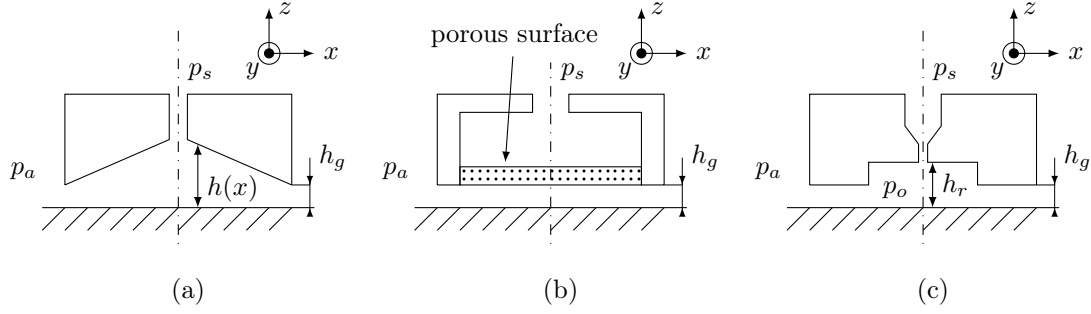
Figure 2.5: Load carrying capacity and stiffness enhancing air bearing design variations: (a) conical gap (b) orifice & recess (c) porous surface.

where S denotes stiffness, F a vertical force, z the vertical distance, F_{ab} the vertical fluid force subjected on the air bearing mass and, h_r the bearing gap height of the bearing. If the height of the air bearing gap changes, the pressure under the bearing pad does also change because of the orifice, resulting in a different load capacity F_{ab}. Hence, the orifice creates stiffness in the air bearing. The recess can be used to allow for a large pressure under the air bearing resulting in an increased load carrying capacity. Note that all of the above design variations can also be applied on journal bearings.

2.2 Modeling

The first step in the design of an air bearing is the development of a mathematical model to predict the bearing characteristics like load carrying capacity and stiffness. In this section first the different mathematical model components are introduced. Second, a short overview is given of solution techniques used in literature to find a solution of the equation(s) belonging to the mathematical model.

2.2.1 Mathematical model

The mathematical model of the air bearing consists of two parts. The first part is the dynamic model describing the motion of the moving mass of the air bearing. The dynamic model is represented by the equation of motion of the air bearing, that is based on Newton's second law

$$\sum \vec{F} = M\ddot{\vec{x}}_G \tag{2.2}$$

where $\sum \vec{F}$ denotes the net force acting on the mass M, $\vec{x}_G$ is the position vector of the center of mass G of the moving mass and ¨ denotes the second derivative with respect to time.

The second part models the fluid or lubrication film that can be represented by several models. One of these models consist of the Navier-Stokes equation and the equation of continuity [47]. If further a thin film is assumed, the Reynolds equation can be derived [13]

$$\nabla \cdot \frac{\rho h^3}{12\mu} \nabla p = \nabla \cdot \frac{\rho h}{2} \vec{V} + \frac{\partial \rho h}{\partial t} \tag{2.3}$$

where ρ is the fluid density, h the fluid film height, μ the fluid viscosity, p is the fluid pressure, $\vec{V}$ is the relative velocity of the two bearing surfaces with respect to each other and t denotes time. Further, operator $\nabla \cdot (\cdot)$ denotes the divergence operator and $\nabla(\cdot)$ the gradient operator. The Reynolds equation omits fluid inertia in the Navier-Stokes equation because of the thin film assumption. This is elaborated further in chapter 3. Besides models based on the Navier-Stokes equations also other mathematical models can be used to model fluid films. For example, the linearized Boltzmann equation is used to model gas films because for ultra-thin films the flows

cannot be considered as continuum flows [34]. Therefore, the linearized Boltzmann equation is used in the modeling of hard disk drive sliders [11] [41]. Also, computer fluid dynamics techniques (CFD) are used to model fluid films for air bearings [19].

In order to get the mathematical problem well-posed there is an equal number of unknowns and equations needed. In (2.2), the net force $\sum \vec{F}$ often consists of the known gravity force and the unknown air bearing fluid film force F_{ab}. The position vector $\vec{x}_G$ is also unknown. The unknowns in the Reynolds equation are the pressure p and fluid film height h. Because h is linked to $\vec{x}_G$ this is considered as one unknown. This results in three unknowns, F_{ab}, $\vec{x}_G$, p, and two equations (2.2) and (2.3). The third equation follows from the fluid film pressing against the bearing surface resulting in

$$F_{ab} = \int_A p dA \qquad (2.4)$$

where A denotes the fluid film area below the air bearing mass. This equation couples the Reynolds equation to the dynamic model. Further, to solve the Reynolds equation (2.3), which is an elliptic partial differential equation, boundary conditions on the pressure are needed [6]. The solution of (2.2) and (2.3) requires also initial conditions.

A third part is needed in the air bearing model if the bearing contains a porous surface or orifice. In the case of a porous surface, Darcy's law is used to model the fluid mass flow through the surface which is used to determine the pressure at the porous surface. This pressure is then used as boundary condition in the solution of the Reynolds equation [5] [26]. For the modeling of an orifice, Bernoulli's equation for the mass flow through a hole is often used to compute the pressure underneath the orifice [1]. Modified versions of this orifice model are also used that correspond better to experimental observations, for example the orifice model by [14] or [38].

2.2.2 Numerical solution techniques

Different numerical integration techniques are used in literature to solve the equations of motion (2.2). The techniques vary from an explicit Euler method [45], [17] to the fourth-order Runge-Kuta method [25], [10]. An often used method to solve the Reynolds equation (2.3) is the finite difference method (FDM), for example in [17] and [1]. Another often used numerical solution method is the Finite Element Method (FEM) [10]. The solution techniques above can be used to find a full numerical solution of the non-linear Reynolds equation. Another much used solution method is based on linearization of the Reynolds equation by perturbation techniques. From the linearized Reynolds equation, frequency and height dependent dynamic coefficients are determined to assess the load carrying capacity and stability [9].

2.3 Stability

Air bearings are often equipped with conical gaps, recesses, or porous surfaces to increase the load capacity and stiffness. A drawback of these bearings is that they can exhibit unstable behavior referred to as pneumatic hammering. Pneumatic hammering is a self-excited vibration due to compressibility of gas, slow pressure recovery, and bearing inertia [51]. This phenomenon occurs if the air bearing gap contains a storage volume[15], as for example the recess in Figure 2.5 (c), and the bearing is externally pressurized. Another instability phenomenon that is encountered in journal bearings is whirl instability [15].

Stability is often assessed by applying a perturbation method on the Reynolds equation and determining the frequency dependent complex dynamic stiffness

$$K(\omega) = k(\omega) + j\omega d(\omega). \qquad (2.5)$$

Herein $k(\omega)$ is the stiffness coefficient, $d(\omega)$ is the damping coefficient with ω the angular frequency and j identifies the imaginary unit. It is observed by analysis and experiments that if the static damping $d(0)$ is positive, it will remain positive for all frequencies and tends to zero for infinite frequency [9]. This implies that any perturbation of the system will eventually damp out. If the static

stiffness is negative it will first become positive for increasing frequency and then tend towards zero for infinite frequency. For frequencies where the damping is negative pneumatic hammering will occur. This stability assessment is only valid for small perturbations about the equilibrium gap height because of the linearization executed using the perturbation method. Therefore, this assessment has to be performed for many gap heights in the working range of the air bearing.

If also the dynamic behavior for large displacements has to be evaluated, a method proposed in [22] can be applied. Herein the frequency dependent dynamic coefficients are used to model a local linear fluid film force during a transient simulation. The dynamic coefficients at the starting height of the air bearing are used to model the fluid film force. If the gap height gets to far away from this local linearization, then there is switched to a closer linear fluid film force model and the transient simulation is continued. Another option to assess the large displacement dynamic behavior is to numerically solve the non-linear Reynolds equation for a certain load case. In this way it is also possible to study the non-linear bearing characteristics using phase portraits, bifurcation diagrams, and Poincaré diagrams [7].

2.4 Thrust bearing with orifice restriction

In this study, the dynamic behavior of a flat single hole orifice thrust air bearing subjected to a vertical transient external force is investigated. Figure 2.6 shows this bearing schematically. It is assumed that the bearing is axially symmetric with an outer radius of R_2 and with an orifice radius of R_1. The mass of the bearing is equal to M. Air is supplied from the side of the bearing with a pressure p_s. The supplied air flows through the orifice and the pressure, just underneath the orifice hole, drops to p_o. Subsequently, the air flows to the air bearing gap inlet at the R_1 radius with pressure p_{in} from where it flows to the ambient air with pressure p_a ($p_s > p_o \geq p_{in} > p_a$). The height of the bearing gap is denoted by h and is assumed to be uniform along the bearing surface.
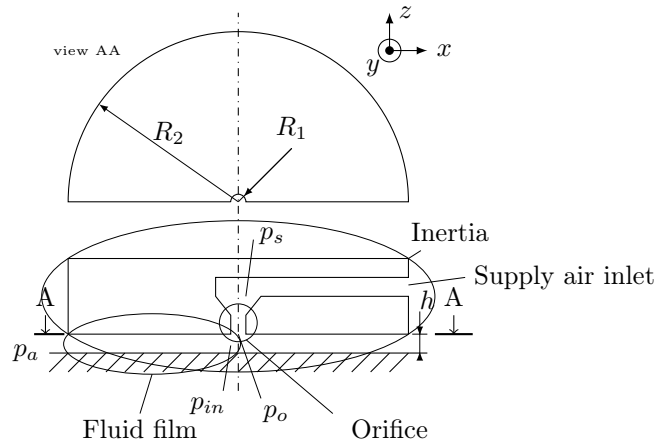
Figure 2.6: Schematic drawing of a flat single hole orifice thrust bearing.

The mathematical model of this bearing consists of three parts. First, the dynamics of the moving bearing part with mass M is described by (2.2). Second, a model of the orifice restriction. As pointed out in subsection 2.2.1, the orifice can be modeled by Bernoulli's equation for mass flow through a hole. However, [14] describes a modified equation to model the orifice that should better match experimental observations. Both orifice models are investigated in this study. In this case, the orifice is an essential component to create stiffness in the air bearing. This can be seen if the static Reynolds equation is considered in Cartesian coordinates

$$\frac{\partial}{\partial x}\left(\frac{\rho h^3}{12\mu}\frac{\partial p}{\partial x}\right) + \frac{\partial}{\partial y}\left(\frac{\rho h^3}{12\mu}\frac{\partial p}{\partial y}\right) = 0. \tag{2.6}$$

Because h is uniform it drops out of (2.6). This means that the pressure is independent of the gap height h and therefore also the fluid film force F_{ab} does not depend on h. Because the fluid film force does not change with a change in height there is no stiffness following the definition in (2.1). The orifice provides a relation between the height and the fluid film force resulting in a stiffness. Last, the fluid film force is modeled by the Reynolds equation (2.3) and (2.4).

2.5 Summary

In this chapter an overview on the types of air bearings and applications was given. Further, different types of models were given to model air bearings and the use of these model to assess stability of air bearings. Finally, the air bearing under consideration, a axially symmetric flat single hole orifice thrust air bearing, was presented. Also the components to model this air bearing were present

In the upcoming chapters these model components will be further elaborated. In the next chapter, a derivation of the Reynolds equation, one of the model components, will be presented and the assumptions made in this derivation will be discussed. Hence, the conditions of the air bearing will be discussed for which the developed mathematical model will be applicable.

Chapter 3

Lubrication approximation of fluid flow

The derivation of the thin film approximation for lubricant flow is presented in this chapter and is based on the work of [37] and [13]. First the dominating terms in the Navier-Stokes equation for a thin film flow are identified. Second, using these dominant terms the thin film approximation for a lubricant flow is derived. The resulting equation is called the Reynolds equation after Osborn Reynolds [30]. Third, the Reynolds equation is simplified for some special cases of fluid bearings. Finally, a summary of the derived equations is given.

3.1 Navier-Stokes equation

The starting point is Cauchy's equation of motion which can be obtained by applying Newton's second law on an infinitesimal fluid particle. This fluid particle is schematically drawn in Figure 3.1 and the balance of forces acting on it are

$$
\begin{aligned}
\rho \frac{du}{dt} \Delta V &= \Delta T_{xx} \Delta y \Delta z + \Delta T_{yx} \Delta x \Delta z + \Delta T_{zx} \Delta x \Delta y + \rho f_x \Delta V, \\
\rho \frac{dv}{dt} \Delta V &= \Delta T_{xy} \Delta y \Delta z + \Delta T_{yy} \Delta x \Delta z + \Delta T_{zy} \Delta x \Delta y + \rho f_y \Delta V, \\
\rho \frac{dw}{dt} \Delta V &= \Delta T_{xz} \Delta y \Delta z + \Delta T_{yz} \Delta x \Delta z + \Delta T_{zz} \Delta x \Delta y + \rho f_z \Delta V.
\end{aligned}
\tag{3.1}
$$

Here ρ is the fluid mass density, u, v, and w are the velocities of the fluid particle in the x, y, and z direction, respectively. ΔV is the volume of the fluid particle and is equal to $\Delta V = \Delta x \Delta y \Delta z$. T_{ij} is the stress component of the fluid particle in the j direction acting on the plane perpendicular to the i direction. $\rho f_x \Delta V$, $\rho f_y \Delta V$, and $\rho f_z \Delta V$ are the fluid body forces in the x, y, and z direction respectively. The operator $\frac{d}{dt}(\cdot)$ is the material derivative defined as

$$
\frac{d}{dt}(\cdot) = \frac{\partial}{\partial t}(\cdot) + u \frac{\partial}{\partial x}(\cdot) + v \frac{\partial}{\partial y}(\cdot) + w \frac{\partial}{\partial z}(\cdot).
\tag{3.2}
$$

The stress terms ΔT_{xx}, ΔT_{yx}, and ΔT_{zx} in the first equation of (3.1) can be written as

$$
\Delta T_{xx} = \frac{\partial T_{xx}}{\partial x} \Delta x, \quad \Delta T_{yx} = \frac{\partial T_{yx}}{\partial y} \Delta y, \quad \Delta T_{zx} = \frac{\partial T_{zx}}{\partial z} \Delta z.
\tag{3.3}
$$

Analogously, the change in stress in the other two equations in (3.1) are also expressed in derivatives of the components of the stress tensor. Substituting this in (3.1) and eliminating the common
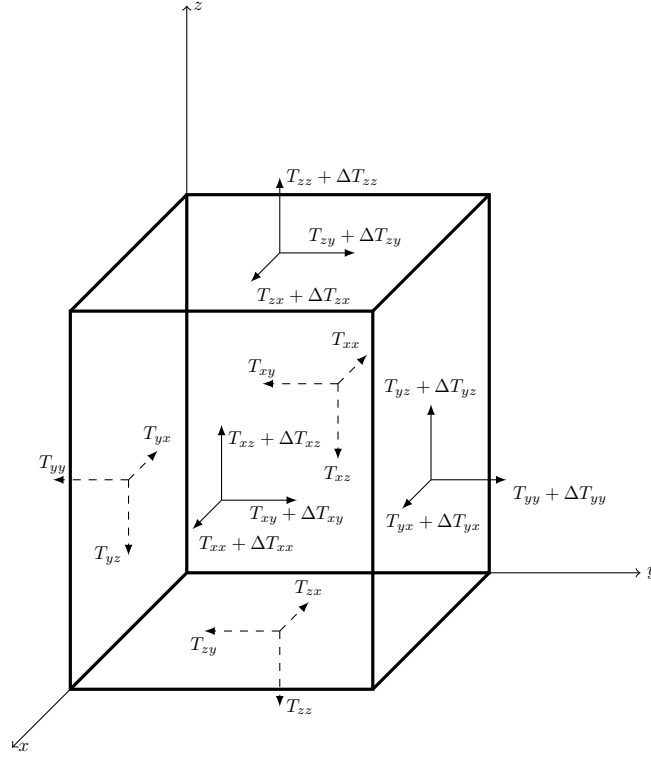
Figure 3.1: Surface stresses for a fluid particle.

term ΔV results in

$$
\begin{aligned}
\rho \frac{du}{dt} &= \frac{\partial T_{xx}}{\partial x} + \frac{\partial T_{yx}}{\partial y} + \frac{\partial T_{zx}}{\partial z} + \rho f_x, \\
\rho \frac{dv}{dt} &= \frac{\partial T_{xy}}{\partial x} + \frac{\partial T_{yy}}{\partial y} + \frac{\partial T_{zy}}{\partial z} + \rho f_y, \\
\rho \frac{dw}{dt} &= \frac{\partial T_{xz}}{\partial x} + \frac{\partial T_{yz}}{\partial y} + \frac{\partial T_{zz}}{\partial z} + \rho f_z,
\end{aligned}
\tag{3.4}
$$

which is known as Cauchy's equation of motion.

The Navier-Stokes equation is found by substituting the constitutive equation for an isotropic Newtonian fluid into (3.4). This constitutive equation relating stresses to strain rates is defined as [18]

$$
T_{ij} = -\left(p + \frac{2}{3}\mu \, \mathrm{div}(\underline{v}) \right) \delta_{ij} + 2\mu e_{ij}
\tag{3.5}
$$

where p is the pressure, μ is the shear viscosity of the fluid, $\underline{v}$ is the velocity vector, δ_{ij} is the Kronecker delta and the strain rate

$$
e_{ij} = \frac{1}{2}\left(\frac{\partial v_i}{\partial x_j} + \frac{\partial v_j}{\partial x_i} \right).
\tag{3.6}
$$

where v_i is the ith element of the velocity vector $\underline{v} = \begin{bmatrix} u & v & w \end{bmatrix}^T$ and x_i is the ith element of position vector $\underline{x} = \begin{bmatrix} x & y & z \end{bmatrix}^T$. Operator $\mathrm{div}(\cdot)$ is the divergence operator and is in a Cartesian coordinate system for the velocity vector defined as

$$
\mathrm{div}(\underline{v}) = \frac{\partial u}{\partial x} + \frac{\partial v}{\partial y} + \frac{\partial w}{\partial z}.
\tag{3.7}
$$

A fluid is called Newtonian if there is a linear relation between the viscous stress and strain rate. Equation (3.5) can be written in matrix notation as

$$
\begin{bmatrix} T_{xx} & T_{xy} & T_{xz} \\ T_{yx} & T_{yy} & T_{yz} \\ T_{zx} & T_{zy} & T_{zz} \end{bmatrix} = - \left(p + \frac{2}{3}\mu\mathrm{div}(\underline{v}) \right) I + 2\mu \begin{bmatrix} \frac{\partial u}{\partial x} & \frac{1}{2}\left(\frac{\partial u}{\partial y} + \frac{\partial v}{\partial x}\right) & \frac{1}{2}\left(\frac{\partial u}{\partial z} + \frac{\partial w}{\partial x}\right) \\ \frac{1}{2}\left(\frac{\partial u}{\partial y} + \frac{\partial v}{\partial x}\right) & \frac{\partial v}{\partial y} & \frac{1}{2}\left(\frac{\partial v}{\partial z} + \frac{\partial w}{\partial y}\right) \\ \frac{1}{2}\left(\frac{\partial u}{\partial z} + \frac{\partial w}{\partial x}\right) & \frac{1}{2}\left(\frac{\partial v}{\partial z} + \frac{\partial w}{\partial y}\right) & \frac{\partial w}{\partial z} \end{bmatrix}
$$

(3.8)

where I denotes the identity matrix. Substitution of (3.8) in (3.4) yields the Navier-Stokes equation in Cartesian coordinates for a Newtonian fluid

$$
\rho\left(\frac{\partial u}{\partial t} + u\frac{\partial u}{\partial x} + v\frac{\partial u}{\partial y} + w\frac{\partial u}{\partial z}\right) = -\frac{\partial p}{\partial x} - \frac{2}{3}\frac{\partial}{\partial x}\left(\mu\mathrm{div}(\underline{v})\right) + 2\frac{\partial}{\partial x}\left(\mu\frac{\partial u}{\partial x}\right)
$$
$$
+ \frac{\partial}{\partial y}\left(\mu\left(\frac{\partial u}{\partial y} + \frac{\partial v}{\partial x}\right)\right) + \frac{\partial}{\partial z}\left(\mu\left(\frac{\partial u}{\partial z} + \frac{\partial w}{\partial x}\right)\right) + \rho f_x
$$

(3.9)

$$
\rho\left(\frac{\partial v}{\partial t} + u\frac{\partial v}{\partial x} + v\frac{\partial v}{\partial y} + w\frac{\partial v}{\partial z}\right) = -\frac{\partial p}{\partial y} - \frac{2}{3}\frac{\partial}{\partial y}\left(\mu\mathrm{div}(\underline{v})\right) + 2\frac{\partial}{\partial y}\left(\mu\frac{\partial v}{\partial y}\right)
$$
$$
+ \frac{\partial}{\partial x}\left(\mu\left(\frac{\partial u}{\partial y} + \frac{\partial v}{\partial x}\right)\right) + \frac{\partial}{\partial z}\left(\mu\left(\frac{\partial v}{\partial z} + \frac{\partial w}{\partial y}\right)\right) + \rho f_y
$$

(3.10)

$$
\rho\left(\frac{\partial w}{\partial t} + u\frac{\partial w}{\partial x} + v\frac{\partial w}{\partial y} + w\frac{\partial w}{\partial z}\right) = -\frac{\partial p}{\partial z} - \frac{2}{3}\frac{\partial}{\partial z}\left(\mu\mathrm{div}(\underline{v})\right) + 2\frac{\partial}{\partial z}\left(\mu\frac{\partial w}{\partial z}\right)
$$
$$
+ \frac{\partial}{\partial x}\left(\mu\left(\frac{\partial u}{\partial z} + \frac{\partial w}{\partial x}\right)\right) + \frac{\partial}{\partial y}\left(\mu\left(\frac{\partial v}{\partial z} + \frac{\partial w}{\partial y}\right)\right) + \rho f_z
$$

(3.11)

The terms on the left hand side describe the inertia effect of the fluid particle and the terms on the right hand side describe the body force, pressure, and viscous effects. The above equations expressing the balance of forces contain four unknowns: u, v, w, and p. In order to find these four unknowns a fourth equation is needed which is the balance of mass, also known as the continuity equation

$$
\frac{\partial \rho}{\partial t} + \mathrm{div}(\rho\underline{v}) = 0.
$$

(3.12)

The Navier-Stokes equations and the continuity equation are used to derive the Reynolds equation for lubricant flow.

The dominant terms in the Navier-Stokes equations for a thin film flow can be derived by exploiting the difference in length scales between the in-plane geometry and fluid film thickness for thin film applications. The position variables are made dimensionless by using

$$
\bar{x} = \frac{x}{x_*} \quad ; \quad \bar{y} = \frac{y}{y_*} \quad ; \quad \bar{z} = \frac{z}{z_*},
$$

(3.13)

where x_*, y_*, and z_* are the characteristics length scales. The dimensionless velocity components are

$$
\bar{u} = \frac{u}{u_*} \quad ; \quad \bar{v} = \frac{v}{v_*} \quad ; \quad \bar{w} = \frac{w}{w_*},
$$

(3.14)

where u_*, v_*, and w_* are the characteristics velocity scales. The quantities ρ, μ, p, and t are made dimensionless by:

$$
\bar{\rho} = \frac{\rho}{\rho_*} \quad ; \quad \bar{\mu} = \frac{\mu}{\mu_*} \quad ; \quad \bar{p} = \frac{p}{p_*} = \frac{z_*^2 p}{\mu_* u_* x_*} \quad ; \quad \bar{t} = \frac{t}{t_*} = \frac{u_*}{x_*}t,
$$

(3.15)

where ρ_* is the characteristic density and μ_* the characteristic shear viscosity. Substitution of the normalized parameters in (3.9) till (3.11) yields

$$
\rho_* \bar{\rho} \left(\frac{u_*^2}{x_*} \frac{\partial \bar{u}}{\partial \bar{t}} + \frac{u_*^2}{x_*} \bar{u} \frac{\partial \bar{u}}{\partial \bar{x}} + \frac{v_* u_*}{y_*} \bar{v} \frac{\partial \bar{u}}{\partial \bar{y}} + \frac{w_* u_*}{z_*} \bar{w} \frac{\partial \bar{u}}{\partial \bar{z}} \right) = - \frac{\mu_* u_* x_*}{z_*^2 x_*} \frac{\partial \bar{p}}{\partial \bar{x}}
$$
$$
- \frac{2}{3} \frac{\mu_* u_*}{x_*^2} \frac{\partial}{\partial \bar{x}} \left(\bar{\mu} \left(\frac{\partial \bar{u}}{\partial \bar{x}} + \frac{x_* v_*}{u_* y_*} \frac{\partial \bar{v}}{\partial \bar{y}} + \frac{x_* w_*}{u_* z_*} \frac{\partial \bar{w}}{\partial \bar{z}} \right) \right)
$$
$$
+ 2 \frac{\mu_* u_*}{x_*^2} \frac{\partial}{\partial \bar{x}} \left(\bar{\mu} \frac{\partial \bar{u}}{\partial \bar{x}} \right) + \frac{\mu_*}{y_*} \frac{\partial}{\partial \bar{y}} \left(\bar{\mu} \left(\frac{u_*}{y_*} \frac{\partial \bar{u}}{\partial \bar{y}} + \frac{v_*}{x_*} \frac{\partial \bar{v}}{\partial \bar{x}} \right) \right)
$$
$$
+ \frac{\mu_*}{z_*} \frac{\partial}{\partial \bar{z}} \left(\bar{\mu} \left(\frac{u_*}{z_*} \frac{\partial \bar{u}}{\partial \bar{z}} + \frac{w_*}{x_*} \frac{\partial \bar{w}}{\partial \bar{x}} \right) \right) + \rho_* \bar{\rho} f_x,
$$
$$(3.16)$$

$$
\rho_* \bar{\rho} \left(\frac{v_* u_*}{x_*} \frac{\partial \bar{v}}{\partial \bar{t}} + \frac{u_* v_*}{x_*} \bar{u} \frac{\partial \bar{v}}{\partial \bar{x}} + \frac{v_*^2}{y_*} \bar{v} \frac{\partial \bar{v}}{\partial \bar{y}} + \frac{w_* v_*}{z_*} \bar{w} \frac{\partial \bar{v}}{\partial \bar{z}} \right) = - \frac{\mu_* u_* x_*}{z_*^2 y_*} \frac{\partial \bar{p}}{\partial \bar{y}}
$$
$$
- \frac{2}{3} \frac{\mu_* v_*}{y_*^2} \frac{\partial}{\partial \bar{y}} \left(\bar{\mu} \left(\frac{y_* x_*}{v_* u_*} \frac{\partial \bar{u}}{\partial \bar{x}} + \frac{\partial \bar{v}}{\partial \bar{y}} + \frac{y_* w_*}{v_* z_*} \frac{\partial \bar{w}}{\partial \bar{z}} \right) \right)
$$
$$
+ 2 \frac{\mu_* v_*}{y_*^2} \frac{\partial}{\partial \bar{y}} \left(\bar{\mu} \left(\frac{\partial \bar{v}}{\partial \bar{y}} \right) \right) + \frac{\mu_*}{x_*} \frac{\partial}{\partial \bar{x}} \left(\bar{\mu} \left(\frac{u_*}{y_*} \frac{\partial \bar{u}}{\partial \bar{y}} + \frac{v_*}{x_*} \frac{\partial \bar{v}}{\partial \bar{x}} \right) \right)
$$
$$
+ \frac{\mu_*}{z_*} \frac{\partial}{\partial \bar{z}} \left(\bar{\mu} \left(\frac{v_*}{z_*} \frac{\partial \bar{v}}{\partial \bar{z}} + \frac{w_*}{y_*} \frac{\partial \bar{w}}{\partial \bar{y}} \right) \right) + \rho_* \bar{\rho} f_y,
$$
$$(3.17)$$

$$
\rho_* \bar{\rho} \left(\frac{w_* u_*}{x_*} \frac{\partial \bar{w}}{\partial \bar{t}} + \frac{u_* w_*}{x_*} \bar{u} \frac{\partial \bar{w}}{\partial \bar{x}} + \frac{v_* w_*}{y_*} \bar{v} \frac{\partial \bar{w}}{\partial \bar{y}} + \frac{w_*^2}{z_*} \bar{w} \frac{\partial \bar{w}}{\partial \bar{z}} \right) = - \frac{\mu_* u_* x_*}{z_*^3} \frac{\partial \bar{p}}{\partial \bar{z}}
$$
$$
- \frac{2}{3} \frac{\mu_*}{z_*} \frac{\partial}{\partial \bar{z}} \left(\bar{\mu} \left(\frac{u_*}{x_*} \frac{\partial \bar{u}}{\partial \bar{x}} + \frac{v_*}{y_*} \frac{\partial \bar{v}}{\partial \bar{y}} + \frac{w_*}{z_*} \frac{\partial \bar{w}}{\partial \bar{z}} \right) \right)
$$
$$
+ 2 \frac{\mu_* w_*}{z_*^2} \frac{\partial}{\partial \bar{z}} \left(\bar{\mu} \frac{\partial \bar{w}}{\partial \bar{z}} \right) + \frac{\mu_*}{x_*} \frac{\partial}{\partial \bar{x}} \left(\bar{\mu} \left(\frac{u_*}{z_*} \frac{\partial \bar{u}}{\partial \bar{z}} + \frac{w_*}{x_*} \frac{\partial \bar{w}}{\partial \bar{x}} \right) \right)
$$
$$
+ \frac{\mu_*}{y_*} \frac{\partial}{\partial \bar{y}} \left(\bar{\mu} \left(\frac{v_*}{z_*} \frac{\partial \bar{v}}{\partial \bar{z}} + \frac{w_*}{y_*} \frac{\partial \bar{w}}{\partial \bar{y}} \right) \right) + \rho_* \bar{\rho} f_z.
$$
$$(3.18)$$

Multiplying (3.16) by $\frac{z_*^2 x_*}{\mu_* u_* x_*}$ and dividing by $\bar{\rho}$ results in

$$
\frac{\rho_* z_*^2 u_*}{\mu_* x_*} \frac{\partial \bar{u}}{\partial \bar{t}} + \frac{\rho_* z_*^2 u_*}{\mu_* x_*} \bar{u} \frac{\partial \bar{u}}{\partial \bar{x}} + \frac{\rho_* z_*^2 v_*}{\mu_* y_*} \bar{v} \frac{\partial \bar{u}}{\partial \bar{y}} + \frac{\rho_* w_* z_*}{\mu_*} \bar{w} \frac{\partial \bar{u}}{\partial \bar{z}} = - \frac{1}{\bar{\rho}} \frac{\partial \bar{p}}{\partial \bar{x}} + \frac{\rho_* z_*^2}{\mu_* u_*} f_x
$$
$$
- \frac{2}{3} \left(\frac{z_*}{x_*} \right)^2 \frac{1}{\bar{\rho}} \frac{\partial}{\partial \bar{x}} \left(\bar{\mu} \left(\frac{\partial \bar{u}}{\partial \bar{x}} + \frac{x_* v_*}{u_* y_*} \frac{\partial \bar{v}}{\partial \bar{y}} + \frac{x_* w_*}{u_* z_*} \frac{\partial \bar{w}}{\partial \bar{z}} \right) \right)
$$
$$
+ 2 \left(\frac{z_*}{x_*} \right)^2 \frac{1}{\bar{\rho}} \frac{\partial}{\partial \bar{x}} \left(\bar{\mu} \frac{\partial \bar{u}}{\partial \bar{x}} \right)
$$
$$
+ \left(\frac{z_*}{y_*} \right)^2 \frac{1}{\bar{\rho}} \frac{\partial}{\partial \bar{y}} \left(\bar{\mu} \left(\frac{\partial \bar{u}}{\partial \bar{y}} + \frac{v_* y_*}{x_* u_*} \frac{\partial \bar{v}}{\partial \bar{x}} \right) \right)
$$
$$
+ \frac{1}{\bar{\rho}} \frac{\partial}{\partial \bar{z}} \left(\bar{\mu} \left(\frac{\partial \bar{u}}{\partial \bar{z}} + \frac{w_* z_*}{x_* u_*} \frac{\partial \bar{w}}{\partial \bar{x}} \right) \right).
$$
$$(3.19)$$

Multiplying (3.17) by $\frac{z_*^2 y_*}{\mu_* u_* x_*}$ and dividing by $\bar{\rho}$, assuming that $x_* \approx y_*$ and $u_* \approx v_*$ because of

almost equivalent length scales, results in

$$
\frac{\rho_* z_*^2 u_*}{\mu_* x_*} \frac{\partial \bar{v}}{\partial \bar{t}} + \frac{\rho_* z_*^2 u_*}{\mu_* x_*} \bar{u} \frac{\partial \bar{v}}{\partial \bar{x}} + \frac{\rho_* z_*^2 v_*}{\mu_* y_*} \bar{v} \frac{\partial \bar{v}}{\partial \bar{y}} + \frac{\rho_* w_* z_*}{\mu_*} \bar{w} \frac{\partial \bar{v}}{\partial \bar{z}} = -\frac{1}{\bar{\rho}} \frac{\partial \bar{p}}{\partial \bar{y}} + \frac{\rho_* z_*^2}{\mu_* u_*} f_y
$$

$$
- \frac{2}{3} \left(\frac{z_*}{y_*} \right)^2 \frac{1}{\bar{\rho}} \frac{\partial}{\partial y_*} \left(\bar{\mu} \left(\frac{y_* x_*}{v_* u_*} \frac{\partial \bar{u}}{\partial \bar{x}} + \frac{\partial \bar{v}}{\partial \bar{y}} + \frac{y_* w_*}{v_* z_*} \frac{\partial \bar{w}}{\partial \bar{z}} \right) \right)
$$

$$
+ 2 \left(\frac{z_*}{y_*} \right)^2 \frac{1}{\bar{\rho}} \frac{\partial}{\partial \bar{y}} \left(\bar{\mu} \left(\frac{\partial \bar{v}}{\partial \bar{y}} \right) \right)
$$

$$
+ \left(\frac{z_*}{x_*} \right)^2 \frac{1}{\bar{\rho}} \frac{\partial}{\partial \bar{x}} \left(\bar{\mu} \left(\frac{u_* x_*}{y_* v_*} \frac{\partial \bar{u}}{\partial \bar{y}} + \frac{\partial \bar{v}}{\partial \bar{x}} \right) \right)
$$

$$
+ \frac{1}{\bar{\rho}} \frac{\partial}{\partial \bar{z}} \left(\bar{\mu} \left(\frac{\partial \bar{v}}{\partial \bar{z}} + \frac{w_* z_*}{y_* v_*} \frac{\partial \bar{w}}{\partial \bar{y}} \right) \right).
$$

$$(3.20)$$

Multiplying (3.18) by $\frac{z_*^3}{\mu_* u_* x_*}$ and dividing by $\bar{\rho}$ yields

$$
\frac{\rho_* w_* z_*^3 u_*}{\mu_* u_* x_*^2} \frac{\partial \bar{w}}{\partial \bar{t}} + \frac{\rho_* w_* z_*}{\mu_*} \left(\frac{z_*}{x_*} \right)^2 \bar{u} \frac{\partial \bar{w}}{\partial \bar{x}} + \frac{\rho_* w_* z_*}{\mu_*} \left(\frac{z_*}{x_*} \right)^2 \bar{v} \frac{\partial \bar{w}}{\partial \bar{y}} + \frac{\rho_* w_*^2 z_*^2}{\mu_* u_* x_*} \bar{w} \frac{\partial \bar{w}}{\partial \bar{z}} = -\frac{1}{\bar{\rho}} \frac{\partial \bar{p}}{\partial \bar{z}} + \frac{\rho_* z_*^3}{\mu_* u_* x_*} f_z
$$

$$
- \frac{2}{3} \left(\frac{z_*}{x_*} \right)^2 \frac{1}{\bar{\rho}} \frac{\partial}{\partial \bar{z}} \left(\bar{\mu} \left(\frac{\partial \bar{u}}{\partial \bar{x}} + \frac{v_* x_*}{y_* u_*} \frac{\partial \bar{v}}{\partial \bar{y}} + \frac{w_* x_*}{z_* y_*} \frac{\partial \bar{w}}{\partial \bar{z}} \right) \right)
$$

$$
+ 2 \frac{w_* z_*}{u_* x_*} \frac{1}{\bar{\rho}} \frac{\partial}{\partial \bar{z}} \left(\bar{\mu} \frac{\partial \bar{w}}{\partial \bar{z}} \right) + \frac{z_*}{u_*} \left(\frac{z_*}{x_*} \right)^2 \frac{1}{\bar{\rho}} \frac{\partial}{\partial \bar{x}} \left(\bar{\mu} \left(\frac{u_*}{z_*} \frac{\partial \bar{u}}{\partial \bar{z}} + \frac{w_*}{x_*} \frac{\partial \bar{w}}{\partial \bar{x}} \right) \right)
$$

$$
+ \frac{z_*}{u_*} \left(\frac{z_*}{x_*} \right)^2 \frac{1}{\bar{\rho}} \frac{\partial}{\partial \bar{y}} \left(\bar{\mu} \left(\frac{v_*}{z_*} \frac{\partial \bar{v}}{\partial \bar{z}} + \frac{w_*}{y_*} \frac{\partial \bar{w}}{\partial \bar{y}} \right) \right).
$$

$$(3.21)$$

In bearing applications the ratio between the film thickness and in-plane geometry is in general of order

$$
\frac{z_*}{x_*} \approx \frac{z_*}{y_*} \approx \mathcal{O}(10^{-3}).
$$

$$(3.22)$$

In (3.19) - (3.21) the term

$$
\left(\frac{z_*}{x_*} \right)^2
$$

$$(3.23)$$

often occurs, which is of order $\mathcal{O}(10^{-6})$. Therefore it is reasonable to assume that the terms containing $\left(\frac{z_*}{x_*} \right)^2$ can be neglected. Note hereby that $\frac{w_*}{u_*}$ and $\frac{w_*}{v_*}$ are of the same order as $\frac{z_*}{x_*}$. Then the equations (3.19) - (3.21) become

$$
\frac{\rho_* z_*^2}{\mu_* t_*} \frac{\partial \bar{u}}{\partial \bar{t}} + \frac{\rho_* z_*^2 u_*}{\mu_* x_*} \bar{u} \frac{\partial \bar{u}}{\partial \bar{x}} + \frac{\rho_* z_*^2 v_*}{\mu_* y_*} \bar{v} \frac{\partial \bar{u}}{\partial \bar{y}} + \frac{\rho_* w_* z_*}{\mu_*} \bar{w} \frac{\partial \bar{u}}{\partial \bar{z}} = -\frac{1}{\bar{\rho}} \frac{\partial \bar{p}}{\partial \bar{x}} + \frac{\rho_* z_*^2}{\mu_* u_*} f_x
$$
$$
+ \frac{1}{\bar{\rho}} \frac{\partial}{\partial \bar{z}} \left(\bar{\mu} \frac{\partial \bar{u}}{\partial \bar{z}} \right),
$$

$$(3.24)$$

$$
\frac{\rho_* z_*^2}{\mu_* t_*} \frac{\partial \bar{v}}{\partial \bar{t}} + \frac{\rho_* z_*^2 u_*}{\mu_* x_*} \bar{u} \frac{\partial \bar{v}}{\partial \bar{x}} + \frac{\rho_* z_*^2 v_*}{\mu_* y_*} \bar{v} \frac{\partial \bar{v}}{\partial \bar{y}} + \frac{\rho_* w_* z_*}{\mu_*} \bar{w} \frac{\partial \bar{v}}{\partial \bar{z}} = -\frac{1}{\bar{\rho}} \frac{\partial \bar{p}}{\partial \bar{y}} + \frac{\rho_* z_*^2}{\mu_* u_*} f_y
$$
$$
+ \frac{1}{\bar{\rho}} \frac{\partial}{\partial \bar{z}} \left(\bar{\mu} \frac{\partial \bar{v}}{\partial \bar{z}} \right),
$$

$$(3.25)$$

$$
0 = -\frac{1}{\bar{\rho}} \frac{\partial \bar{p}}{\partial \bar{z}} + \frac{\rho_* z_*^3}{\mu_* u_* x_*} f_z.
$$

$$(3.26)$$

In subsection 3.1.1 it will be motivated that the left hand side of (3.24) - (3.26) can be neglected because they are of order $\frac{z_*}{x_*}$, resulting in

$$\frac{1}{\bar{\rho}}\frac{\partial\bar{p}}{\partial\bar{x}} = \frac{1}{\bar{\rho}}\frac{\partial}{\partial\bar{z}}\left(\bar{\mu}\frac{\partial\bar{u}}{\partial\bar{z}}\right) + \frac{\rho_* z_*^2}{\mu_* u_*}f_x, \tag{3.27}$$

$$\frac{1}{\bar{\rho}}\frac{\partial\bar{p}}{\partial\bar{y}} = \frac{1}{\bar{\rho}}\frac{\partial}{\partial\bar{z}}\left(\bar{\mu}\frac{\partial\bar{v}}{\partial\bar{z}}\right) + \frac{\rho_* z_*^2}{\mu_* u_*}f_y, \tag{3.28}$$

$$\frac{1}{\bar{\rho}}\frac{\partial\bar{p}}{\partial\bar{z}} = \frac{\rho_* z_*^3}{\mu_* u_* x_*}f_z. \tag{3.29}$$

By neglecting the body forces and and writing equations (3.27) till (3.29) in dimensional form the reduced version of the general Navier-Stokes equations is obtained as

$$\frac{\partial p}{\partial x} = \frac{\partial}{\partial z}\left(\mu\frac{\partial u}{\partial z}\right) \tag{3.30}$$

$$\frac{\partial p}{\partial y} = \frac{\partial}{\partial z}\left(\mu\frac{\partial v}{\partial z}\right) \tag{3.31}$$

$$\frac{\partial p}{\partial z} = 0 \tag{3.32}$$

3.1.1 Remarks

First of all note that (3.32) indicates that the pressure is constant across the film thickness. Further, [18] states that for air "the linear relationship is found surprisingly accurate for most applications" where the linear relationship between viscous stress and strain rate is meant. Therefore, in this report, it is assumed that air is a Newtonian fluid and that the Navier-Stokes equations (3.30) - (3.32) can be applied for air bearing applications.

The Reynolds number can be recognized in the inertia term on the left hand side of equations (3.24) - (3.26), see e.g. [13]. The Reynolds number represents the ratio between the inertia forces and the viscous forces and is defined as

$$R_e = \frac{\rho_* u_* x_*}{\mu_*} \tag{3.33}$$

As mentioned in [13], the modified Reynolds number is often used in fluid film lubrication problems which is defined in multiple directions as

$$R_x = \frac{\rho_* u_* z_*^2}{\mu_* x_*}, \tag{3.34}$$

$$R_y = \frac{\rho_* v_* z_*^2}{\mu_* y_*}, \tag{3.35}$$

and

$$R_z = \frac{\rho_* w_* z_*}{\mu_*}. \tag{3.36}$$

The squeeze number is defined as

$$\sigma_s = \frac{\rho_* z_*^2}{\mu_* t_*}. \tag{3.37}$$

These terms can all be seen in the inertia terms of equations (3.24) till (3.26) and are assumed to be of order $\frac{z_*}{x_*}$. This means that the fluid inertia terms may be neglected. For the squeeze number σ_s this can be seen by substituting $t_* = \frac{x_*}{u_*}$. The proof that R_z is of order $\frac{z_*}{x_*}$ follows from the equation of continuity. If the parameters in (3.12) are made dimensionless this results in

$$\frac{\rho_* u_*}{x_*}\frac{\partial\bar{\rho}}{\partial\bar{t}} + \frac{\rho_* u_*}{x_*}\frac{\partial\bar{\rho}\bar{u}}{\partial\bar{x}} + \frac{\rho_* v_*}{y_*}\frac{\partial\bar{\rho}\bar{v}}{\partial\bar{y}} + \frac{\rho_* w_*}{z_*}\frac{\partial\bar{\rho}\bar{w}}{\partial\bar{z}} = 0. \tag{3.38}$$

This can be rewritten as

$$\frac{\partial \bar{\rho}}{\partial \bar{t}} + \frac{\partial \bar{\rho}\bar{u}}{\partial \bar{x}} + \frac{\partial \bar{\rho}\bar{v}}{\partial \bar{y}} + \frac{x_* w_*}{u_* z_*}\frac{\partial \bar{\rho}\bar{w}}{\partial \bar{z}} = 0. \tag{3.39}$$

In order for this equation to hold

$$w_* = \frac{z_*}{x_*}u_*. \tag{3.40}$$

Substituting (3.40) in (3.36) shows that R_z is of order $\frac{z_*}{x_*}$.
In the case that a gas is used as lubricant, the ideal gas law has to be applied to normalize the density based on the pressure. The ideal gas law is defined as

$$p_* = \rho_* R_s T \tag{3.41}$$

where R_s is the specific gas constant and T the gas temperature. From (3.15) it follows that

$$p_* = \frac{\mu_* u_* x_*}{z_*^2} \tag{3.42}$$

and thus

$$\rho_* = \frac{\mu_* u_* x_*}{z_*^2 R_s T}. \tag{3.43}$$

If this density normalization factor is substituted in the equations (3.24) - (3.26), it is noticed that the terms indicating the order of $\frac{z_*}{x_*}$ disappear. However, the term $\frac{1}{R_s T}$ appears which is generally of order $\mathcal{O}(10^{-4})$ and thus smaller then $\frac{z_*}{x_*}$. Hence, it can be assumed that these terms are small enough to be neglected.

3.2 Reynolds equation

The reduced Navier-Stokes equations (3.30) and (3.31) can be integrated twice with respect to z, resulting in

$$u = \frac{1}{2\mu}\frac{\partial p}{\partial x}z^2 + \frac{1}{\mu}Az + B \tag{3.44}$$

$$v = \frac{1}{2\mu}\frac{\partial p}{\partial y}z^2 + \frac{1}{\mu}Cz + D \tag{3.45}$$

where and A, B, C, and D are integration constants. The following boundary conditions can be used to determine the integration constants:

$$\begin{aligned} u = U_0, \ v = V_0 \quad &\text{at} \quad z = 0, \\ u = U_h, \ v = V_h \quad &\text{at} \quad z = h. \end{aligned} \tag{3.46}$$

Substitution of the first set of boundary conditions in (3.44) and (3.45) gives

$$U_0 = B \tag{3.47}$$

and

$$V_0 = D. \tag{3.48}$$

Substitution of the second set of boundary conditions and (3.47) in (3.44) results in

$$U_h = \frac{1}{2\mu}\frac{\partial p}{\partial x}h^2 + \frac{1}{\mu}Ah + U_0 \rightarrow A = \frac{\mu}{h}\left(U_h - U_0\right) - \frac{1}{2}\frac{\partial p}{\partial x}h. \tag{3.49}$$

Substitution of the second set of boundary conditions and (3.48) in (3.45) yields

$$V_h = \frac{1}{2\mu}\frac{\partial p}{\partial y}h^2 + \frac{1}{\mu}Ch + V_0 \rightarrow C = \frac{\mu}{h}\left(V_h - V_0\right) - \frac{1}{2}\frac{\partial p}{\partial y}h. \tag{3.50}$$

Substitution of the integration constants (3.49) and (3.47) in (3.44) results in

$$
\begin{aligned}
u =& \frac{1}{2\mu}\frac{\partial p}{\partial x}z^2 + \frac{1}{\mu}\left(\frac{\mu}{h}\left(U_h - U_0\right) - \frac{1}{2}\frac{\partial p}{\partial x}h\right)z + U_0 \\
=& \frac{1}{2\mu}\frac{\partial p}{\partial x}(z^2 - hz) + \left(1 - \frac{z}{h}\right)U_0 + \frac{z}{h}U_h.
\end{aligned}
\tag{3.51}
$$

Analogously, substituting (3.50) and (3.48) in (3.45) yields

$$
\begin{aligned}
v =& \frac{1}{2\mu}\frac{\partial p}{\partial y}z^2 + \frac{1}{\mu}\left(\frac{\mu}{h}\left(V_h - V_0\right) - \frac{1}{2}\frac{\partial p}{\partial y}h\right)z + V_0 \\
=& \frac{1}{2\mu}\frac{\partial p}{\partial y}\left(z^2 - hz\right) + \left(1 - \frac{z}{h}\right)V_0 + \frac{z}{h}V_h.
\end{aligned}
\tag{3.52}
$$

The continuity equation (3.12) written in Cartesian coordinates is

$$
\frac{\partial \rho}{\partial t} + \frac{\partial \rho u}{\partial x} + \frac{\partial \rho v}{\partial y} + \frac{\partial \rho w}{\partial z} = 0.
\tag{3.53}
$$

Equation (3.53) is integrated across the height z

$$
\rho w|_0^h = \rho\left(W_h - W_0\right) = -\int_0^h \left(\frac{\partial \rho u}{\partial x}\right)dz - \int_0^h \left(\frac{\partial \rho v}{\partial y}\right)dz - \int_0^h \left(\frac{\partial \rho}{\partial t}\right)dz.
\tag{3.54}
$$

where W_0 is the velocity in the z direction at $z = 0$ and W_h is the velocity in the z direction at $z = h$. It is assumed that these velocities are known. Substitution of (3.51) and (3.52) in (3.54) yields

$$
\begin{aligned}
\rho w|_0^h =& -\int_0^h \left(\frac{\partial}{\partial x}\left[\rho\left(\frac{1}{2\mu}\frac{\partial p}{\partial x}(z^2 - hz) + \left(1 - \frac{z}{h}\right)U_0 + \frac{z}{h}U_h\right)\right]\right)dz \\
&-\int_0^h \left(\frac{\partial}{\partial y}\left[\rho\left(\frac{1}{2\mu}\frac{\partial p}{\partial y}(z^2 - hz) + \left(1 - \frac{z}{h}\right)V_0 + \frac{z}{h}V_h\right)\right]\right)dz - \int_0^h \left(\frac{\partial \rho}{\partial t}\right)dz.
\end{aligned}
\tag{3.55}
$$

By applying Leibnitz's rule for differentiation under the integral sign

$$
\frac{d}{dx}\int_A^B f(x,t)dt = \int_A^B \frac{\partial f(x,t)}{\partial x}dt + f(x,B)\frac{dB}{dx} - f(x,A)\frac{dA}{dx},
\tag{3.56}
$$

(3.55) can be rewritten as

$$
\begin{aligned}
\rho w|_0^h =& -\frac{\partial}{\partial x}\left(\int_0^h \left[\rho\left(\frac{1}{2\mu}\frac{\partial p}{\partial x}(z^2 - hz) + \left(1 - \frac{z}{h}\right)U_0 + \frac{z}{h}U_h\right)\right]dz\right) + \rho U_h \frac{\partial h}{\partial x} \\
&-\frac{\partial}{\partial y}\left(\int_0^h \left[\rho\left(\frac{1}{2\mu}\frac{\partial p}{\partial y}(z^2 - hz) + \left(1 - \frac{z}{h}\right)V_0 + \frac{z}{h}V_h\right)\right]dz\right) + \rho V_h \frac{\partial h}{\partial y} \\
&-\int_0^h \left(\frac{\partial \rho}{\partial t}\right)dz.
\end{aligned}
\tag{3.57}
$$

Performing the integration on the right hand side yields

$$
\begin{aligned}
\rho w|_0^h =& -\frac{\partial}{\partial x}\left(-\frac{\rho h^3}{12\mu}\frac{\partial p}{\partial x}\right) - \frac{\partial}{\partial x}\left(\frac{\rho h}{2}U_0\right) - \frac{\partial}{\partial x}\left(\frac{\rho h}{2}U_h\right) + \rho U_h \frac{\partial h}{\partial x} \\
&-\frac{\partial}{\partial y}\left(-\frac{\rho h^3}{12\mu}\frac{\partial p}{\partial y}\right) - \frac{\partial}{\partial y}\left(\frac{\rho h}{2}V_0\right) - \frac{\partial}{\partial y}\left(\frac{\rho h}{2}V_h\right) + \rho V_h \frac{\partial h}{\partial y} \\
&-h\frac{\partial \rho}{\partial t}.
\end{aligned}
\tag{3.58}
$$

Note that

$$\rho w|_0^h = \rho \frac{dh}{dt}. \tag{3.59}$$

Then, (3.58) can be rewritten into the general Reynolds equation for lubrication:

$$\frac{\partial}{\partial x}\left(-\frac{\rho h^3}{12\mu}\frac{\partial p}{\partial x}\right) + \frac{\partial}{\partial y}\left(-\frac{\rho h^3}{12\mu}\frac{\partial p}{\partial y}\right) = -\frac{\partial}{\partial x}\left(\frac{\rho h\left(U_0 + U_h\right)}{2}\right) - \frac{\partial}{\partial y}\left(\frac{\rho h\left(V_0 + V_h\right)}{2}\right)$$
$$+ \rho U_h\frac{\partial h}{\partial x} + \rho V_h\frac{\partial h}{\partial y} - h\frac{\partial \rho}{\partial t} - \rho\frac{dh}{dt}. \tag{3.60}$$

This can be further simplified by using the definition of the material derivative (3.2) and applying it to the $\frac{dh}{dt}$ term, resulting in

$$\frac{dh}{dt} = \frac{\partial h}{\partial t} + u\frac{\partial h}{\partial x} + v\frac{\partial h}{\partial y} + w\frac{\partial h}{\partial z}. \tag{3.61}$$

Note that h is a function of x, y and t meaning that the last term in (3.61) can be omitted. Further, for u and v at $z = h$ it holds that $u = U_h$ and $v = V_h$ from which it follows that

$$\frac{dh}{dt} = \frac{\partial h}{\partial t} + U_h\frac{\partial h}{\partial x} + V_h\frac{\partial h}{\partial y}. \tag{3.62}$$

Substitution of (3.62) in (3.60) and using

$$\frac{\partial \rho h}{\partial t} = \rho\frac{\partial h}{\partial t} + h\frac{\partial \rho}{\partial t} \tag{3.63}$$

reduces (3.60) to

$$\frac{\partial}{\partial x}\left(\frac{\rho h^3}{12\mu}\frac{\partial p}{\partial x}\right) + \frac{\partial}{\partial y}\left(\frac{\rho h^3}{12\mu}\frac{\partial p}{\partial y}\right) = \frac{\partial}{\partial x}\left(\frac{\rho h\left(U_0 + U_h\right)}{2}\right) + \frac{\partial}{\partial y}\left(\frac{\rho h\left(V_0 + V_h\right)}{2}\right) + \frac{\partial \rho h}{\partial t}. \tag{3.64}$$

The above equation is known as the Reynolds equation for lubrication in Cartesion coordinates. The Reynolds equation for lubrication in coordinate-free from is

$$\nabla \cdot \frac{\rho h^3}{12\mu}\nabla p = \nabla \cdot \frac{\rho h}{2}\underline{V} + \frac{\partial \rho h}{\partial t}. \tag{3.65}$$

3.3 Simplifications of the Reynolds equation

The Reynolds equation for lubrication (3.65) holds if the assumptions of a Newtonian fluid, the difference in length scales between the fluid thickness and in-plane geometry, negligible inertia and negligible body forces hold. If the two opposite fluid surfaces do not translate in the x and y direction, meaning that $\underline{V} = 0$, then the Reynolds equation reduces to

$$\nabla \cdot \frac{\rho h^3}{12\mu}\nabla p = \frac{\partial \rho h}{\partial t}. \tag{3.66}$$

Further, if it is assumed that the fluid thickness and viscosity is uniform, meaning that h and μ do not depend on the coordinates, the Reynolds equation is written as

$$\nabla \cdot \rho\nabla p = \frac{12\mu}{h^3}\frac{\partial \rho h}{\partial t}. \tag{3.67}$$

For incompressible fluids the density ρ drops from the equation resulting in

$$\nabla \cdot \nabla p = \frac{12\mu}{h^3}\frac{\partial h}{\partial t}. \tag{3.68}$$

If a static situation is considered the right hand side in (3.68) is equal to zero, hence

$$\nabla \cdot \nabla p = 0. \tag{3.69}$$

3.4 Reynolds equation for axial symmetric air bearings

For axially symmetric bearings the Reynolds equation has to be written in cylindrical coordinates. Appendix B gives a procedure to transform the Reynolds equation for Cartesian coordinates into cylindrical coordinates. The Reynolds equation in coordinate-free form can be written into cylindrical coordinate form by applying the gradient and divergence for cylindrical coordinates defined as

$$\nabla(\cdot) = \begin{bmatrix} \frac{\partial(\cdot)}{\partial r} \\ \frac{1}{r}\frac{\partial(\cdot)}{\partial \theta} \\ \frac{\partial(\cdot)}{\partial z} \end{bmatrix} \tag{3.70}$$

and

$$\nabla \cdot (\cdot) = \frac{1}{r}\frac{\partial r(\cdot)_r}{\partial r} + \frac{1}{r}\frac{\partial(\cdot)_\theta}{\partial \theta} + \frac{\partial(\cdot)_z}{\partial z} \tag{3.71}$$

respectively [2]. Application ito (3.66) yields

$$\frac{1}{r}\frac{\partial}{\partial r}\left(r\frac{\rho h^3}{12\mu}\frac{\partial p}{\partial r}\right) + \frac{1}{r}\frac{\partial}{\partial \theta}\left(\frac{\rho h^3}{12\mu r}\frac{\partial p}{\partial \theta}\right) + \frac{\partial}{\partial z}\left(\frac{\rho h^3}{12\mu}\frac{\partial p}{\partial z}\right) = \frac{\partial \rho h}{\partial t} \tag{3.72}$$

Using (3.32) and the property that the air bearing is axially symmetric (3.72) is written as

$$\frac{1}{r}\frac{\partial}{\partial r}\left(r\frac{\rho h^3}{12\mu}\frac{\partial p}{\partial r}\right) = \frac{\partial \rho h}{\partial t}. \tag{3.73}$$

In the remainder of this report the simplified Reynolds equation (3.73) will be used to model the air bearing fluid film.

3.5 Summary

The Reynolds equation is derived from the Navier-Stokes equation for a Newtonian fluid and the equation of continuity by exploiting the difference in length-scales between the in-plane geometry and fluid film thickness. Furthermore, it is assumed that the fluid inertia and body forces are negligible. The general Reynolds equation in Cartesian coordinates reads

$$\frac{\partial}{\partial x}\left(\frac{\rho h^3}{12\mu}\frac{\partial p}{\partial x}\right) + \frac{\partial}{\partial y}\left(\frac{\rho h^3}{12\mu}\frac{\partial p}{\partial y}\right) = \frac{\partial}{\partial x}\left(\frac{\rho h\left(U_0 + U_h\right)}{2}\right) + \frac{\partial}{\partial y}\left(\frac{\rho h\left(V_0 + V_h\right)}{2}\right) + \frac{\partial \rho h}{\partial t}. \tag{3.64}$$

If it is assumed that the bearing does not translate in the x or y direction and that the bearing is axially symmetric (3.64) reduces to

$$\frac{1}{r}\frac{\partial}{\partial r}\left(r\frac{\rho h^3}{12\mu}\frac{\partial p}{\partial r}\right) = \frac{\partial \rho h}{\partial t}. \tag{3.74}$$

where cylindrical coordinates are used. It is assumed that the circular orifice bearing under consideration has a uniform film thickness and viscosity. This means that (3.74) can be written as

$$\frac{\partial}{\partial r}\left(r\rho\frac{\partial p}{\partial r}\right) = \frac{12\mu r}{h^3}\frac{\partial \rho h}{\partial t}. \tag{3.75}$$

If the fluid is incompressible the density ρ drops from the equation giving

$$\frac{\partial}{\partial r}\left(r\frac{\partial p}{\partial r}\right) = \frac{12\mu r}{h^3}\frac{\partial h}{\partial t}. \tag{3.76}$$

If furthermore a static situation is considered then the right hand side in (3.76) vanishes resulting in

$$\frac{\partial}{\partial r}\left(r\frac{\partial p}{\partial r}\right) = 0. \tag{3.77}$$

Table 3.1 gives all simplified versions of the Reynolds equations used in this report and the conditions and assumptions under which these are valid.

In the next chapter, the derived Reynolds equation will be used to develop a thrust air bearing model.

Table 3.1: Simplified versions of the Reynolds equation and the application conditions.

Equation	Assumptions
$\frac{\partial}{\partial r}\left(r\rho\frac{\partial p}{\partial r}\right) = \frac{12\mu r}{h^3}\frac{\partial \rho h}{\partial t}$	- Newtonian fluid - Negligible fluid inertia - Negligible body forces - $x_* >> z_*,\ y_* >> z_*$ - $U_0 = U_h = V_0 = V_h = 0$ - $\mu = \text{constant}$ - $h = \text{uniform}$
$\frac{\partial}{\partial r}\left(r\frac{\partial p}{\partial r}\right) = \frac{12\mu r}{h^3}\frac{\partial h}{\partial t}$	- Newtonian fluid - Negligible fluid inertia - Negligible body forces - $x_* >> z_*,\ y_* >> z_*$ - $U_0 = U_h = V_0 = V_h = 0$ - $\mu = \text{constant}$ - $h = \text{uniform}$ - $\rho = \text{constant(incompressibility)}$
$\frac{\partial}{\partial r}\left(r\frac{\partial p}{\partial r}\right) = 0$	- Newtonian fluid - Negligible fluid inertia - Negligible body forces - $x_* >> z_*,\ y_* >> z_*$ - $U_0 = U_h = V_0 = V_h = 0$ - $\mu = \text{constant}$ - $h = \text{uniform}$ - $\rho = \text{constant(incompressibility)}$ - $\frac{\partial h}{\partial t} = 0$

Chapter 4

Thrust air bearing model

As already mentioned in section 2.4, in this study a flat single hole orifice thrust air bearing is considered. The model of a thrust air bearing contains basically three parts, the lubrication or fluid film model, the orifice model, and the dynamic model of the supported solid. First the lubrication model is investigated which is represented by the Reynolds equation for lubrication that was derived in the previous chapter. In order to simplify the lubrication model, first the Reynolds equation for incompressible fluids is investigated before the compressible case is considered. After investigation of these two cases the orifice restriction model is examined and added to the lubrication model. Finally, the incompressible lubrication model and the restriction model are combined with the dynamic model of the supported solid to model the dynamics of the flat axial symmetric thrust air bearing. Table 4.1 shows the parameter values used for mathematical analyses presented in this chapter (if not stated otherwise). Some of these parameters are indicated in Figure 4.1. Further, it is assumed that the initial velocity is zero.

Parameter symbol	Value	Unit	Quantity
R_1	$2 \cdot 10^{-4}$	m	Orifice radius
R_2	$4 \cdot 10^{-2}$	m	Air bearing radius
p_s	$2 \cdot 10^5$	N/m^2	Supply pressure
p_{in}	$2 \cdot 10^5$	N/m^2	Air gap inlet pressure
p_a	$1 \cdot 10^5$	N/m^2	Ambient pressure
T	293	K	Temperature
μ	$1.8205 \cdot 10^{-5}$	kg/(ms)	Viscosity
R_s	287	J/(kgK)	Specific gas constant
κ	1.405	–	Adiabatic expansion coefficient
M	5	kg	Air bearing mass
g	9.81	m/s^2	Gravitational constant

Table 4.1: Model parameter values used in simulations.
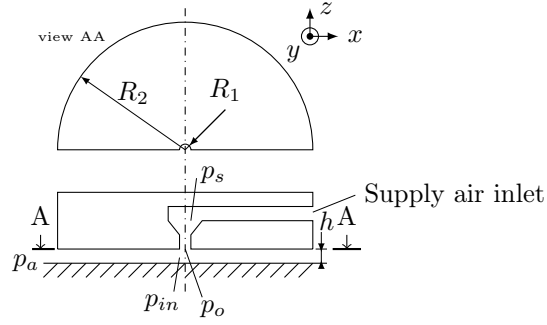
Figure 4.1: Schematic drawing of a flat single hole orifice thrust bearing.

4.1 Incompressible fluids

The incompressible lubrication model for axial symmetric thrust bearings is described by the Reynolds equation for incompressible fluids

$$\frac{\partial}{\partial r}\left(r\frac{\partial p}{\partial r}\right) = \frac{12\mu r}{h^3}\frac{\partial h}{\partial t} \tag{4.1}$$

as was derived in chapter 3 (see (3.76)). First an analytic solution of this equation is sought. Second, the finite difference method is discussed and used to obtain a numerical solution. Finally, the analytical and numerical solutions are compared.

4.1.1 Analytical solution

The analytical solution of (4.1) is

$$p = p_{part} + p_{hom} \tag{4.2}$$

where p_{hom} is the homogeneous solution and p_{part} the particular solution. The homogeneous solution is the solution of the homogeneous incompressible Reynolds equation

$$\frac{\partial}{\partial r}\left(r\frac{\partial p}{\partial r}\right) = 0. \tag{4.3}$$

In order to solve (4.3) two boundary conditions are needed because the differential equation is of order 2. It is assumed that the pressure at the bearing gap inlet is equal to the orifice outlet ($p_{in} = p_o$) and that the ambient pressure is p_a. This results in the following boundary conditions

$$\begin{aligned} p &= p_{in} \quad \text{at} \quad r = R_1, \\ p &= p_a \quad \text{at} \quad r = R_2. \end{aligned} \tag{4.4}$$

Integration of (4.3) yields

$$r\frac{dp}{dr} = A \rightarrow \frac{dp}{dr} = \frac{1}{r}A \tag{4.5}$$

where A is an integration constant. The pressure is solved from (4.5) and reads

$$p = \ln(r)A + B \tag{4.6}$$

where B is a second integration constant. Substitution of the first and second boundary condition in (4.6) results in

$$p_{in} = \ln(R_1)A + B, \tag{4.7}$$

$$p_a = \ln(R_2)A + B. \tag{4.8}$$

Solving (4.7) and (4.8) for A and B gives

$$A = \frac{p_{in} - p_a}{\ln(R_1/R_2)}, \quad B = p_{in} - \ln(R_1) A. \tag{4.9}$$

Substituting (4.9) in (4.6) gives the solution of (4.3), hence the pressure is

$$p = (p_{in} - p_a) \frac{\ln(r/R_2)}{\ln(R_1/R_2)} + p_a. \tag{4.10}$$

This equation can be made dimensionless and normalized by assuming

$$p = p_{in}\bar{p}, \quad r = R_2\bar{r}, \quad p_a = 0. \tag{4.11}$$

The solution can then be written as

$$\bar{p} = \frac{\ln(\bar{r})}{\ln(R_1/R_2)} \tag{4.12}$$

which is equal to the result in [37], see equation (3.6).
With the pressure distribution known it is possible to calculate the load capacity W of the air bearing. The load capacity consists of a load carrying part directly under the inlet hole

$$W_{ih} = \pi R_1^2 p_{in} \tag{4.13}$$

and a part under the bearing surface which can be expressed as

$$W_{abs} = \int_0^{2\pi} \int_{R_1}^{R_2} (rp)\, dr d\phi = 2\pi \int_{R_1}^{R_2} (rp)\, dr. \tag{4.14}$$

The ambient pressure acts on the top of the air bearing and provides a negative force on the bearing

$$W_a = -\pi R_2^2 p_a. \tag{4.15}$$

This gives for the full load capacity

$$W = \pi R_1^2 p_{in} - \pi R_2^2 p_a + 2\pi \int_{R_1}^{R_2} (rp)\, dr. \tag{4.16}$$

Substituting (4.10) into (4.16) and solving the integral results in the homogeneous load capacity

$$W_{hom} = \pi (p_{in} - p_a) \frac{R_2^2 - R_1^2}{2\ln(R_2/R_1)}. \tag{4.17}$$

Equation (4.17) is used to describe the static load capacity of an air bearing with an incompressible lubricant film. After all, in the static case it holds that $\frac{\partial h}{\partial t} = 0$.
A solution for p in the non-homogeneous equation (4.1) can be computed in a similar way. Again the following boundary conditions are used.

$$\begin{aligned} p = p_{in} \quad &at \quad r = R_1, \\ p = p_a \quad &at \quad r = R_2. \end{aligned} \tag{4.18}$$

Integrating (4.1) once with respect to r gives

$$r\frac{\partial p}{\partial r} = \frac{6\mu r^2}{h^3}\frac{\partial h}{\partial t} + A \rightarrow \frac{\partial p}{\partial r} = \frac{6\mu r}{h^3}\frac{\partial h}{\partial t} + \frac{1}{r}A. \tag{4.19}$$

Integrating twice yields

$$p = \frac{3\mu r^2}{h^3}\frac{\partial h}{\partial t} + \ln(r)A + B. \tag{4.20}$$

Substitution of the first and second boundary condition in (4.20) results in

$$p_{in} = \frac{3\mu R_1^2}{h^3}\frac{\partial h}{\partial t} + \ln(R_1)A + B, \tag{4.21}$$

$$p_a = \frac{3\mu R_2^2}{h^3}\frac{\partial h}{\partial t} + \ln(R_2)A + B. \tag{4.22}$$

Solving (4.21) and (4.22) for A and B results in

$$A = \frac{p_{in} - p_a}{\ln(R_1/R_2)} + \frac{(R_2^2 - R_1^2)}{\ln(R_1/R_2)}\frac{3\mu}{h^3}\frac{\partial h}{\partial t}, \tag{4.23}$$

$$B = \frac{-(p_{in} - p_a)\ln(R_2)h^3 + 3\mu R_1^2 \ln(R_2)\frac{\partial h}{\partial t} - 3\mu R_2^2 \ln(R_1)\frac{\partial h}{\partial t}}{h^3 \ln(R_1/R_2)} + p_a. \tag{4.24}$$

The pressure p follows from (4.20), after substituting (4.23) and (4.24) and reads

$$\begin{aligned} p =& \frac{3\mu r^2}{h^3}\frac{\partial h}{\partial t} + \ln(r)\left(\frac{p_{in} - p_a}{\ln(R_1/R_2)} + \frac{(R_2^2 - R_1^2)}{\ln(R_1/R_2)}\frac{3\mu}{h^3}\frac{\partial h}{\partial t}\right) \\ &+ \frac{-(p_{in} - p_a)\ln(R_2)h^3 + 3\mu R_1^2 \ln(R_2)\frac{\partial h}{\partial t} - 3\mu R_2^2 \ln(R_1)\frac{\partial h}{\partial t}}{h^3 \ln(R_1/R_2)} + p_a. \end{aligned} \tag{4.25}$$

This can be rewritten as

$$p = \frac{3\mu}{h^3}\frac{\partial h}{\partial t}\left(r^2 + \ln(r)\frac{(R_2^2 - R_1^2)}{\ln(R_1/R_2)} + \frac{R_1^2 \ln(R_2) - R_2^2 \ln(R_1)}{\ln(R_1/R_2)}\right) + (p_{in} - p_a)\frac{\ln(r/R_2)}{\ln(R_1/R_2)} + p_a, \tag{4.26}$$

which is the fluid film pressure distribution for incompressible fluids. The last two terms in (4.26) are equal to the homogeneous solution (4.10). Hence,

$$p = p_{part}(r, h, \frac{\partial h}{\partial t}) + p_{hom}(r) \tag{4.27}$$

where

$$p_{part} = \frac{3\mu}{h^3}\frac{\partial h}{\partial t}\left(r^2 + \ln(r)\frac{(R_2^2 - R_1^2)}{\ln(R_1/R_2)} + \frac{R_1^2 \ln(R_2) - R_2^2 \ln(R_1)}{\ln(R_1/R_2)}\right) \tag{4.28}$$

and

$$p_{hom} = (p_{in} - p_a)\frac{\ln(r/R_2)}{\ln(R_1/R_2)} + p_a. \tag{4.29}$$

Substituting (4.26) in (4.16) and solving the integral results in the dynamic load capacity of an air bearing with an incompressible lubricant film

$$W = C_1 \frac{1}{h^3}\frac{\partial h}{\partial t} + C_2 \tag{4.30}$$

where

$$C_1 = -\frac{1}{2}3\mu\pi\left((R_2^4 - R_1^4) + \frac{(R_2^2 - R_1^2)^2}{\ln(R_1/R_2)}\right) \tag{4.31}$$

and

$$C_2 = W_{hom} = \pi(p_{in} - p_a)\frac{R_2^2 - R_1^2}{2\ln(R_2/R_1)}. \tag{4.32}$$

Note that C_2 is equal to the (homogeneous) static load capacity (4.17).
The height $h(t)$ as a function of time for an air bearing subjected to a constant external force $W = F_{ex}$ starting from initial height $h(0) = h_0$ is derived as follows. Rewriting (4.30) gives

$$(F_{ex} - C_2)\,dt = C_1 \frac{1}{h^3}dh. \tag{4.33}$$

Integrating both sides with taking the initial conditions into account yields

$$\int_0^t (F_{ex} - C_2)\, dt = \int_{h_0}^{h(t)} C_1 \frac{1}{h^3}\, dh \tag{4.34}$$

$$(F_{ex} - C_2)\, t = -C_1 \frac{1}{2} \left(\frac{1}{h(t)^2} - \frac{1}{h_0^2} \right). \tag{4.35}$$

Solving (4.35) for h results in

$$h(t) = \pm \sqrt{\frac{1}{\frac{1}{h_0^2} - \frac{2}{C_1}(W - C_2)t}}. \tag{4.36}$$

Assuming that the height cannot be negative gives

$$h(t) = \sqrt{\frac{h_0^2}{1 - h_0^2 \frac{2}{C_1}(W - C_2)t}}. \tag{4.37}$$

The analytic solutions described in (4.10), (4.17), (4.20), (4.30), and (4.37) are used to assess the numerical solution that is derived in the next section.

4.1.2 Numerical solution

A numerical solution of (4.1) can be found by using e.g. the finite difference method. In order to find a solution the problem is split up. First, a numerical solution for the homogeneous problem (4.3) with boundary conditions

$$\begin{aligned} p &= p_{in} \quad \text{at} \quad r = R_1, \\ p &= p_a \quad \text{at} \quad r = R_2 \end{aligned} \tag{4.38}$$

is computed. Second, the particular solution is computed by finding a numerical solution for (4.1) with boundary conditions

$$\begin{aligned} p &= 0 \quad \text{at} \quad r = R_1, \\ p &= 0 \quad \text{at} \quad r = R_2. \end{aligned} \tag{4.39}$$

Finite Difference Method

The following short introduction on the finite difference method is based on [6]. The derivative $\frac{du}{dx}$ of a function $u = u(x)$ is defined as :

$$\frac{du}{dx}(x) = \lim_{\delta \to 0} \frac{u(x + \delta) - u(x)}{\delta} = \lim_{\delta \to 0} \frac{u(x) - u(x - \delta)}{\delta} = \lim_{\delta \to 0} \frac{u(x + \frac{1}{2}\delta) - u(x - \frac{1}{2}\delta)}{\delta}. \tag{4.40}$$

The discretization follows from a Taylor expansion, which for $u(x + \delta)$ at x is

$$u(x + \delta) = u(x) + \delta \frac{du}{dx}(x) + \frac{\delta^2}{2!} \frac{d^2 u}{dx^2}(x) + \frac{\delta^3}{3!} \frac{d^3 u}{dx^3}(x) + \dots. \tag{4.41}$$

This can be rewritten to

$$\frac{du}{dx}(x) = \frac{u(x + \delta) - u(x)}{\delta} + \mathcal{O}(\delta) \tag{4.42}$$

where $\mathcal{O}(\delta^n)$ denotes the local truncation error that contains terms of order n in δ. This is called the "forward finite difference". For $u(x - \delta)$ the Taylor expansion becomes

$$u(x - \delta) = u(x) - \delta \frac{du}{dx}(x) + \frac{\delta^2}{2!} \frac{d^2 u}{dx^2}(x) - \frac{\delta^3}{3!} \frac{d^3 u}{dx^3}(x) + \dots \tag{4.43}$$

which can be rewritten to

$$\frac{du}{dx}(x) = \frac{u(x) - u(x - \delta)}{\delta} + \mathcal{O}(\delta) \tag{4.44}$$

and is called the "backward finite difference". The "central finite difference" is computed as follows. Take the Talyor expansions of $u(x + \frac{1}{2}\delta)$ and $u(x - \frac{1}{2}\delta)$ resulting in

$$u(x + \frac{1}{2}\delta) = u(x) + \frac{1}{2}\delta\frac{du}{dx}(x) + \frac{(\frac{1}{2}\delta)^2}{2!}\frac{d^2u}{dx^2}(x) + \frac{(\frac{1}{2}\delta)^3}{3!}\frac{d^3u}{dx^3}(x) + \dots \tag{4.45}$$

$$u(x - \frac{1}{2}\delta) = u(x) - \frac{1}{2}\delta\frac{du}{dx}(x) + \frac{(\frac{1}{2}\delta)^2}{2!}\frac{d^2u}{dx^2}(x) - \frac{(\frac{1}{2}\delta)^3}{3!}\frac{d^3u}{dx^3}(x) + \dots \tag{4.46}$$

Rewrite (4.45) and (4.46) gives

$$\frac{1}{2}\frac{du}{dx}(x) = \frac{u(x + \frac{1}{2}\delta) - u(x)}{\delta} - \frac{\frac{1}{4}\delta}{2!}\frac{d^2u}{dx^2}(x) - \frac{\frac{1}{8}\delta^2}{3!}\frac{d^3u}{dx^3}(x) + \dots \tag{4.47}$$

$$\frac{1}{2}\frac{du}{dx}(x) = \frac{u(x) - u(x - \frac{1}{2}\delta)}{\delta} + \frac{\frac{1}{4}\delta}{2!}\frac{d^2u}{dx^2}(x) - \frac{\frac{1}{8}\delta^2}{3!}\frac{d^3u}{dx^3}(x) + \dots \tag{4.48}$$

Summing (4.47) and (4.48) yields

$$\frac{du}{dx}(x) = \frac{u(x + \frac{1}{2}\delta) - u(x - \frac{1}{2}\delta)}{\delta} + \mathcal{O}(\delta^2) \tag{4.49}$$

Note that the truncation error $\mathcal{O}(\delta^2)$ of the central finite difference is one order higher than that of the forward finite difference and the backward finite difference. An approximation of the second derivative can be found by applying the central finite difference on the intermediate points resulting in

$$\frac{d^2u}{dx^2} = \frac{\frac{du}{dx}(x + \frac{1}{2}\delta) - \frac{du}{dx}(x - \frac{1}{2}\delta)}{\delta} = \frac{\frac{u(x+\delta)-u(x)}{\delta} - \frac{u(x)-u(x-\delta)}{\delta}}{\delta} =$$
$$= \frac{u(x - \delta) - 2u(x) + u(x + \delta)}{\delta^2} + \mathcal{O}(\delta^2). \tag{4.50}$$
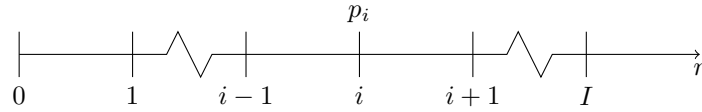
Figure 4.2: Spatial discrete grid of the radius r.

Homogeneous solution

A numerical solution for (4.3) is found by dividing the radius in a grid with I intermediate non-equidistant intervals as shown in Figure 4.2. Herein $p_i = p(r_i)$ is the pressure at grid point i with radius r_i. Equation (4.3) at grid point i can be written in finite difference form by applying the central finite difference to the first derivative of (4.3) resulting in

$$\frac{1}{\frac{1}{2}(\Delta r_{i-1} + \Delta r_i)}\left[r\frac{\partial p}{\partial r}\bigg|_{i+\frac{1}{2}} - r\frac{\partial p}{\partial r}\bigg|_{i-\frac{1}{2}}\right] = 0 \tag{4.51}$$

where

$$\Delta r_{i-1} = r_i - r_{i-1} \quad \Delta r_i = r_{i+1} - r_i. \tag{4.52}$$

Application of the central finite difference to the remaining derivatives yields

$$r \frac{\partial p}{\partial r}\bigg|_{i+\frac{1}{2}} = \frac{1}{2} \left(r_{i+1} + r_i\right) \frac{p_{i+1} - p_i}{\Delta r_i} \tag{4.53}$$

and

$$r \frac{\partial p}{\partial r}\bigg|_{i-\frac{1}{2}} = \frac{1}{2} \left(r_i + r_{i-1}\right) \frac{p_i - p_{i-1}}{\Delta r_{i-1}}. \tag{4.54}$$

Substitution of (4.53) and (4.54) in (4.51) results in

$$\frac{1}{\frac{1}{2}\left(\Delta r_{i-1} + \Delta r_i\right)} \left[\frac{1}{2}\left(r_{i+1} + r_i\right)\frac{p_{i+1} - p_i}{\Delta r_i} - \frac{1}{2}\left(r_i + r_{i-1}\right)\frac{p_i - p_{i-1}}{\Delta r_{i-1}}\right] = 0 \tag{4.55}$$

which can be rewritten as

$$\frac{\left(r_{i+1} + r_i\right)}{\left(\Delta r_{i-1} + \Delta r_i\right)\Delta r_i}p_{i+1} + \left(-\frac{\left(r_{i+1} + r_i\right)}{\left(\Delta r_{i-1} + \Delta r_i\right)\Delta r_i} - \frac{\left(r_i + r_{i-1}\right)}{\left(\Delta r_{i-1} + \Delta r_i\right)\Delta r_{i-1}}\right)p_i + \frac{\left(r_i + r_{i-1}\right)}{\left(\Delta r_{i-1} + \Delta r_i\right)\Delta r_{i-1}}p_{i-1} = 0. \tag{4.56}$$

Or in short notation

$$c_{h1,i}p_{i-1} + c_{h2,i}p_i + c_{h3,i}p_{i+1} = 0. \tag{4.57}$$

Taking the boundary conditions into account this can be written as the grid function

$$R_{hom} = \begin{cases} c_{h1,i}p_{i+1} + c_{h2,i}p_i + c_{h3,i}p_{i-1} = 0 & \forall\, i\, :\, R_1 < r_i < R_2 \\ p_i - p_{in} = 0 & \forall\, i\, :\, r_i = R_1 \\ p_i - p_a = 0 & \forall\, i\, :\, r_i = R_2 \end{cases}. \tag{4.58}$$

This can be written into the following matrix notation

$$\mathbf{R}_{hom}\,\underline{p}_{hom} = \underline{c}_{hom}. \tag{4.59}$$

where

$$\mathbf{R}_{hom} = \begin{bmatrix} 1 & & & & & & \\ c_{h1,1} & c_{h2,1} & c_{h3,1} & & & & \\ & \ddots & \ddots & \ddots & & & \\ & & c_{h1,i} & c_{h2,i} & c_{h3,i} & & \\ & & & \ddots & \ddots & \ddots & \\ & & & & c_{h1,I-1} & c_{h2,I-1} & c_{h3,I-1} \\ & & & & & & 1 \end{bmatrix}, \underline{p}_{hom} = \begin{bmatrix} p_0 \\ p_1 \\ \vdots \\ p_i \\ \vdots \\ p_{I-1} \\ p_I \end{bmatrix}, \underline{c}_{hom} = \begin{bmatrix} p_{in} \\ 0 \\ \vdots \\ 0 \\ \vdots \\ 0 \\ p_a \end{bmatrix}. \tag{4.60}$$

This set of linear equations can be solved with for example a Gaussian elimination method. The static load capacity is computed by substituting the computed pressure distribution $\underline{p}_{hom}$ into (4.16). The integral in this equation is numerically calculated with the trapezoidal integration method resulting in

$$\begin{aligned} W_{num} &= \pi R_1^2 p_{in} - \pi R_2^2 p_a + 2\pi \int_{R_1}^{R_2} (rp)\, dr \\ &\approx \pi R_1^2 p_{in} - \pi R_2^2 p_a + 2\pi \frac{1}{2} \sum_{i=0}^{I-1} \left[(r_{i+1} - r_i)\left(r_{i+1}p_{hom,i+1} + r_i p_{hom,i}\right)\right]. \end{aligned} \tag{4.61}$$

Figure 4.3: Discrete grid of the air bearing radius r and time t.

Particular solution

Equation (4.1) contains besides the spatial derivative also a time derivative. Therefore the space and time grid as shown in Figure 4.3 is considered. Herein $p_{i,j} = p(r_i, t_j)$ is the pressure at grid point (i, j) with radius r_i and on time t_j. I and J denote the number of intermediate non-equidistant intervals in the space and time direction, respectively. Further, $\Delta r_{i-1} = r_i - r_{i-1}$ and $\Delta r_i = r_{i+1} - r_i$.

For the derivation of the finite difference form of (4.1), the following form of the incompressible Reynolds equation is used

$$\frac{1}{r}\frac{\partial}{\partial r}\left(rh^3\frac{\partial p}{\partial r}\right) = 12\mu\frac{\partial h}{\partial t}. \tag{4.62}$$

which is found by eliminating ρ from (3.74) and bringing μ to the right hand side with the assumption of a uniform viscosity. Note that (4.62) can be rewritten as (4.1) with the assumption of a uniform film thickness. By applying the spatial central finite difference at r_i using the intermediate points $i \pm \frac{1}{2}$, (4.62) is approximated by

$$\frac{1}{r_i}\left[\frac{1}{\frac{1}{2}(\Delta r_{i-1} + \Delta r_i)}\left(rh^3\frac{\partial p}{\partial r}\bigg|_{i+\frac{1}{2}} - rh^3\frac{\partial p}{\partial r}\bigg|_{i-\frac{1}{2}}\right)\right] = 12\mu\frac{\partial h}{\partial t}. \tag{4.63}$$

Note that the time index j is omitted here for simplicity. Application of the central finite difference on the intermediate points yields

$$rh^3\frac{\partial p}{\partial r}\bigg|_{i+\frac{1}{2}} = \frac{1}{2}\left(r_ih_i^3 + r_{i+1}h_{i+1}^3\right)\frac{p_{i+1} - p_i}{\Delta r_i} \ \vee \ \left(\frac{1}{2}(r_{i+1} + r_i)\right)\left(\frac{1}{2}(h_{i+1} + h_i)\right)^3\frac{p_{i+1} - p_i}{\Delta r_i} \tag{4.64}$$

and

$$rh^3\frac{\partial p}{\partial r}\bigg|_{i-\frac{1}{2}} = \frac{1}{2}\left(r_{i-1}h_{i-1}^3 + r_i + h_i^3\right)\frac{p_i - p_{i-1}}{\Delta r_{i-1}} \ \vee \ \left(\frac{1}{2}(r_i + r_{i-1})\right)\left(\frac{1}{2}(h_i + h_{i-1})\right)^3\frac{p_i - p_{i-1}}{\Delta r_{i-1}}. \tag{4.65}$$

As can be seen above, two methods can be used to evaluate the central finite difference on the intermediate points. The two methods will be investigated later. Substituting (4.64) and (4.65) in (4.63) results in

$$C_3 \left(C_1 \frac{p_{i+1} - p_i}{\Delta r_i} - C_2 \frac{p_i - p_{i-1}}{\Delta r_{i-1}} \right) = 12\mu \frac{\partial h}{\partial t} \tag{4.66}$$

where

$$C_1 = \frac{1}{2} \left(r_i h_i^3 + r_{i+1} h_{i+1}^3 \right) \; \vee \; \left(\frac{1}{2}(r_{i+1} + r_i) \right) \left(\frac{1}{2}(h_{i+1} + h_i) \right)^3, \tag{4.67}$$

$$C_2 = \frac{1}{2} \left(r_{i-1} h_{i-1}^3 + r_i + h_i^3 \right) \; \vee \; \left(\frac{1}{2}(r_i + r_{i-1}) \right) \left(\frac{1}{2}(h_i + h_{i-1}) \right)^3 \tag{4.68}$$

and

$$C_3 = \frac{1}{\frac{1}{2} r_i (\Delta r_{i-1} + \Delta r_i)} \tag{4.69}$$

Rewriting (4.66) results in

$$\frac{C_3 C_2}{\Delta r_{i-1}} p_{i-1} - C_3 \left(\frac{C_2}{\Delta r_{i-1}} + \frac{C_1}{\Delta r_i} \right) p_i + \frac{C_3 C_1}{\Delta r_i} p_{i+1} = 12\mu \frac{\partial h}{\partial t} \tag{4.70}$$

The following grid function can now be defined

$$R_{inc} = \begin{cases} c_{1,i} p_{i-1} + c_{2,i} p_i + c_{3,i} p_{i+1} = 12\mu \frac{\partial h}{\partial t} & \forall i \; : \; R_1 < r_i < R_2 \\ p_i = 0 & \forall i \; : r_i = R_1 \\ p_i = 0 & \forall i \; : r_i = R_2 \end{cases} \tag{4.71}$$

where

$$c_{1,i} = \frac{C_3 C_2}{\Delta r_{i-1}}, \quad c_{2,i} = -C_3 \left(\frac{C_2}{\Delta r_{i-1}} + \frac{C_1}{\Delta r_i} \right), \quad c_{3,i} = \frac{C_3 C_1}{\Delta r_i}. \tag{4.72}$$

In matrix notation this gives

$$\mathbf{R}_{part,j} \underline{p}_{part,j} = 12\mu \frac{\partial h}{\partial t}_j \underline{c}_{part} \tag{4.73}$$

where

$$\mathbf{R}_{part,j} \begin{bmatrix} 1 & & & & & \\ c_{1,2} & c_{2,2} & c_{3,2} & & & \\ & \ddots & \ddots & \ddots & & \\ & & c_{1,i} & c_{2,i} & c_{3,i} & \\ & & & \ddots & \ddots & \ddots \\ & & & & c_{1,I-1} & c_{2,I-1} & c_{3,I-1} \\ & & & & & 1 \end{bmatrix}, \underline{p}_{part,j} = \begin{bmatrix} p_1 \\ p_2 \\ \vdots \\ p_i \\ \vdots \\ p_{I-1} \\ p_I \end{bmatrix}, \underline{c}_{part} = \begin{bmatrix} 0 \\ 1 \\ \vdots \\ 1 \\ \vdots \\ 1 \\ 0 \end{bmatrix} \tag{4.74}$$

and the time indices j are written again.

Numerical integration scheme

Figure 4.4 shows schematically the numerical procedure that is applied to find the numerical solution of (4.1) for an air bearing subjected to a known transient external force F_{ex}. Further, it is assumed that the height $h(t_0) = h_0$ is known. The balance of forces acting on the bearing is described by

$$F_{ex,j} = W_{hom} + F_{part,j} \tag{4.75}$$

where $F_{ex,j}$ is the externally applied load on time t_j, W_{hom} is the numerical static load capacity in (4.61) and $F_{part,j}$ is the air bearing force contribution of the particular pressure distribution.

The homogeneous load capacity W_{hom} is computed using (4.61) where $\underline{p}_{hom}$ is found by solving (4.59). $F_{part,j}$ follows from the trapezoidal integration of $\underline{p}_{part,j}$

$$F_{part,j} = \int_0^{2\pi} \int_{R_1}^{R_2} rp \, dr d\phi \approx 2\pi \frac{1}{2} \sum_{i=0}^{I-1} \left[(r_{i+1} - r_i) \left(r_{i+1} p_{part,i+1,j} + r_i p_{part,i,j} \right) \right]. \tag{4.76}$$

$\underline{p}_{part,j}$ follows from solving

$$\mathbf{R}_{part,j} \, \underline{p}'_{part,j} = 12\mu \underline{c}_{part} \tag{4.77}$$

where

$$\underline{p}_{part,j} = \underline{p}'_{part,j} \frac{\partial h}{\partial t_j}. \tag{4.78}$$

Note that (4.77) follows from substituting (4.78) in (4.73). Substitution of (4.78) in (4.76) yields

$$\begin{aligned} F_{part,j} =& 2\pi \frac{1}{2} \sum_{i=0}^{I-1} \left[(r_{i+1} - r_i) \left(r_{i1} p'_{part,i+1,j} + r_{i1} p'_{part,i,j} \right) \right] \frac{\partial h}{\partial t_j} \\ =& F'_{part,j} \frac{\partial h}{\partial t_j} \end{aligned} \tag{4.79}$$

Substituting (4.79) in (4.75) results in the following expression for $\frac{\partial h}{\partial t_j}$

$$\frac{\partial h}{\partial t}_j = \frac{F_{ex,j} - W}{F'_{part,j}} \tag{4.80}$$

Knowing $\frac{\partial h}{\partial t_j}$, the height h_{j+1} can be determined for sufficiently small $\Delta t = t_{j+1} - t_j$ by

$$h_{j+1} = h_j + \int_{t_j}^{t_{j+1}} \frac{\partial h}{\partial t} dt \approx h_j + \frac{\partial h}{\partial t} \bigg|_j \Delta t_j. \tag{4.81}$$

This integration method is called the first order forward Euler integration method [4]. h_{j+1} is then the input for a new iteration at the next time step.

The pressure distribution at t_j is computed by

$$\underline{p}_j = \underline{p}_{hom} + \underline{p}_{part,j} = \underline{p}_{hom} + \underline{p}'_{part,j} \frac{\partial h}{\partial t_j}. \tag{4.82}$$

4.1.3 Analytical versus numerical solution

In this section the results for a general solution of the gap height $h(t)$, for two different discretization methods, and for a convergence analysis will be presented. For all the results an initial height $h_0 = 50 \cdot 10^{-6}$ m, $p_{in} = p_s = 2 \cdot 10^5$ N/m^2, $M = 7$ kg, and a constant external force of $F_{ex} = Mg = 68.67$ N is used. Further, the number of elements in the spatial and time direction is $I = 1000$ and $J = 1000$, respectively. The remaining used parameter values are shown in Table 4.1.

Figure 4.5 shows a typical solution of $h(t)$ by applying the numerical procedure as described in the previous section for a linear and logarithmic time discretization and a logarithmic spatial discretization. As can be seen, the height initially decreases fast and approaches 0 asymptotically. Equation (4.30) shows that if W is larger than the static load capacity, then the lubrication film force is proportional to the velocity. Because of the negative sign of C_1 in (4.31) the bearing force acts in the opposite direction of the velocity. It can be concluded that the fluid film acts as a damper. Further, it can be seen that the numerical solution coincides well with the analytic solution.

IC: $j = 0$, h_0, F_{ex}

Compute W_{hom}

Solve $\mathbf{R}_{part,j} \; \underline{p}'_{part,j} = 12\mu\underline{c}_{part}$ for $\underline{p}'_{part,j}$, equation (4.77)

Compute $F'_{part,j}$, equation (4.79)

$j = j + 1$

Compute $\frac{\partial h}{\partial t_j} = \frac{F_{ex,j} - W_{hom}}{F'_{part,j}}$, equation (4.80)

Compute $h_{j+1} = h_j + \frac{\partial h}{\partial t_j}\Delta t_j$, equation (4.81)

$j = J?$

no

yes

Stop
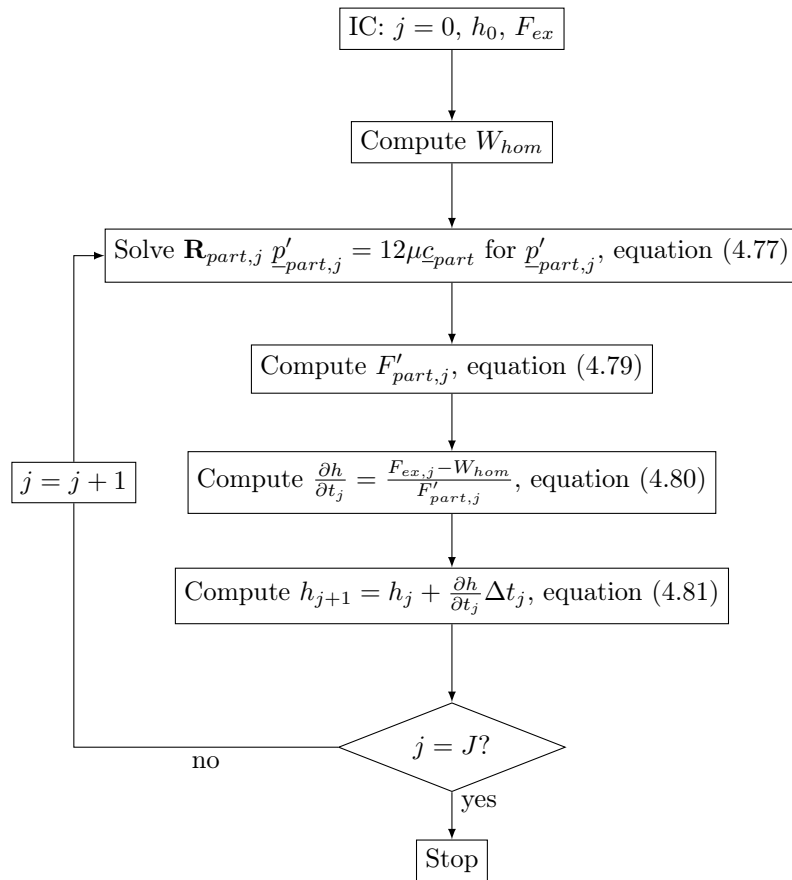
Figure 4.4: Solution scheme for solving $h(t)$ numerically for the incompressible Reynolds equation.

Figure 4.6 shows the error between the numerical and analytic solutions. It is seen that the error in the logarithmic grid is smaller than for the linear grid. The maximum error in the logarithmic and linear grid compared with the analytic solution is respectively $5.7 \cdot 10^{-8}$ m (0.3 %) and $2.5 \cdot 10^{-6}$ m (5 %). From the solution of the height in Figure 4.5 it is seen that the height decreases fast initially. In order to sufficiently approximate this decrease in the numerical solution, it is desired to apply a fine time grid. Because the logarithmic grid has a more dense grid initially, the height is approximated better by the logarithmic grid than by the linear grid. The logarithmic grid becomes less dense when time increases and this means that the linear grid approximates the height better at larger times as can be seen in Figure 4.6. Hence, the application of a logarithmic grid or linear grid depends on the solution of the height. It is also possible to construct for example a hybrid grid between logarithmic or linear grids, or a grid with varying densities.
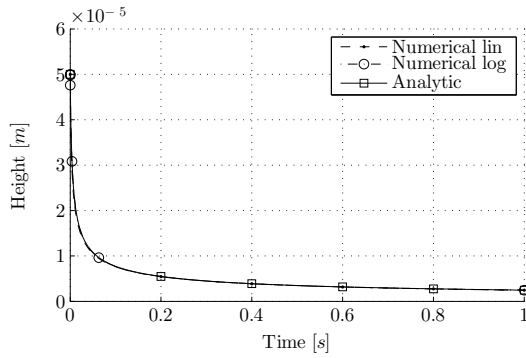
Figure 4.5: Numerical solution of $h(t)$ for $h_0 = 50 \cdot 10^{-6}$ m, $F_{ex} = 68.67$ N, $I = 1000$, $J = 1000$.
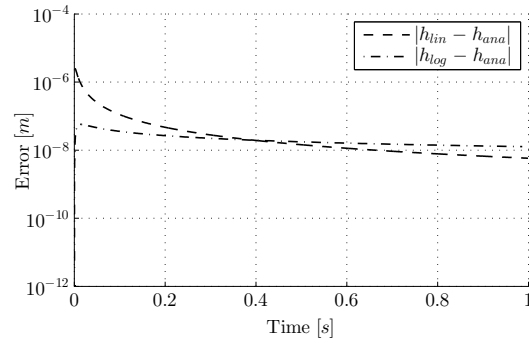
Figure 4.6: Error between analytic and numeric height for $h_0 = 50 \cdot 10^{-6}$ m, $F_{ex} = 68.67$ N, $I = 1000$, $J = 1000$.

In the derivation of the finite difference discretization of the Reynolds equation two options emerged for the coefficients C_1 and C_2 in (4.64) and (4.65), respectively. In order to investigate the difference between option one (FD1) and option two (FD2) for C_1 and C_2, a dynamic simulation can be conducted for each option with the parameter values mentioned in the beginning of this section. Further, a logarithmic spatial discretization and a linear time discretization are used. Figure 4.7 shows the pressure distribution of the numerical solutions and the analytic solution. As can be seen, the differences between FD1, FD2, and the analytic solution are not visible in this figure. Therefore, Figure 4.8 shows the error between the numeric pressure distribution for option one and two and the analytic solution in an attempt to identify a difference. Also in this figure no clear differences are seen but it can be seen that the maximum error in the pressure is approximately 0.1 N/m^2. To identify a difference between FD1 and FD2, Figure 4.9 shows the difference between the errors in Figure 4.8. From this figure it can be seen that there is no clear advantage between FD1 or FD2. For small and large radii option two has a smaller error than option one but in the middle sector option one is smaller. For simplicity option one is used in the remainder of this study.

In order to assess the numerical procedure a convergence analysis is performed to study if the numerical procedure behaves as expected. The pressure distribution is discretized with the central finite difference method resulting in a truncation error of $\mathcal{O}(\delta^2)$ (see (4.49)). If the number of intermediate sections I doubles to $2I$ for a linear discretization, the distance between these points halves resulting in $\mathcal{O}((\frac{1}{2}\delta)^2) = \frac{1}{4}\mathcal{O}(\delta^2)$. Hence, the truncation error for $2I$ is four times smaller compared with the truncation error for I.

Figure 4.10 shows the maximum relative error between the numeric and analytic solution as function of the number of intermediate spatial intervals I for a linear spatial discretization and a
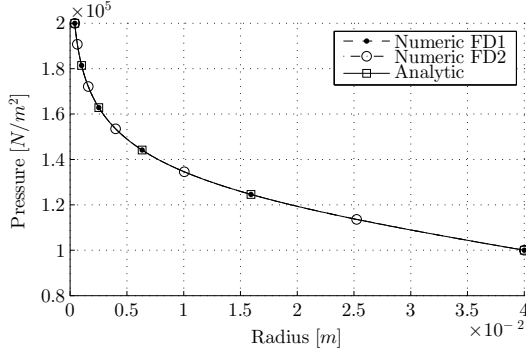
Figure 4.7: Pressure distribution for $F_{ex} = 68.67$ N, $I = 1000$, $J = 1000$.
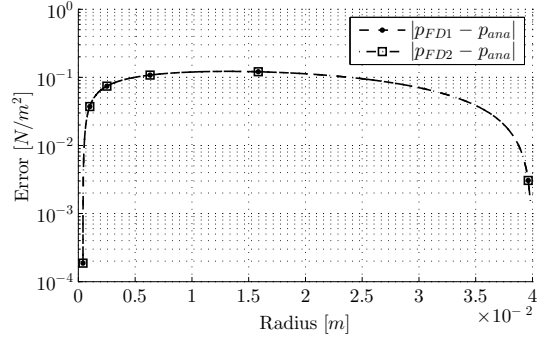
Figure 4.8: Error between analytic and numeric pressure for $F_{ex} = 68.67$ N, $I = 1000$, $J = 1000$.
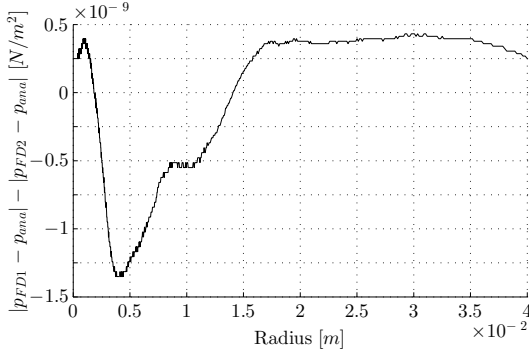
Figure 4.9: Difference between error FD1 and FD2 (FD1 - FD2) for $F_{ex} = 68.67$ N, $I = 1000$, $J = 1000$.
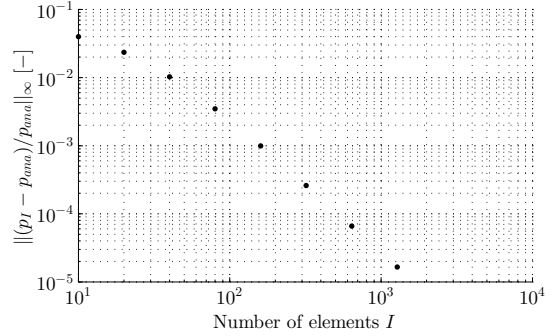
Figure 4.10: Relative error in pressure as function of I for $h_0 = 50 \cdot 10^{-6}$ m, $F_{ex} = 68.67$ N, $J = 1000$.

constant linear time discretization. Herein, the relative error is defined as

$$e_I = \frac{p_I - p_{ana}}{p_{ana}} \tag{4.83}$$

where p_I is the numerical pressure distribution with I intermediate spatial intervals and p_{ana} is the analytic solution at the same spatial grid points as in p_I. It is seen that the error decreases with an increasing number of intermediate intervals I. This indicates that the numerical solution is converging towards the analytic solution if the number of elements I is increased. Figure 4.11 shows the ratio between the subsequent relative maximum errors shown in Figure 4.10. As can be seen, the error ratio converges to 4 if I is large enough, as expected. Figure 4.12 plots the radius of the maximum error as function of I. From this figure it is clear that the location does not change for large values of I.

The same assessment is performed for the Euler discretization in (4.81) and a constant linear spatial discretization with $I = 1000$. According to Atkinson [4] the maximum error should at least halve when the number of intermediate intervals doubles. Thus, if we define the relative error of the numerical solution with J intermediate intervals at time instant t as

$$e_J(t) = \frac{h_J(t) - h_{ana}(t)}{h_{ana}(t)}, \tag{4.84}$$
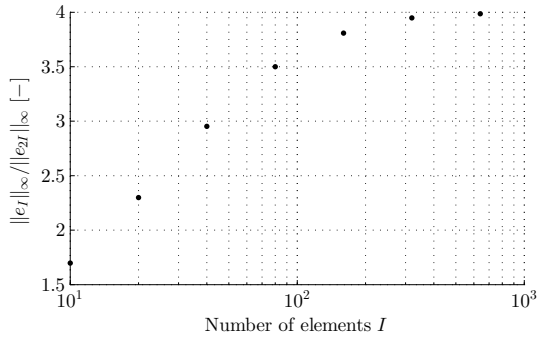
Figure 4.11: Error ratio in pressure as function of I for $h_0 = 50 \cdot 10^{-60}$ m, $F_{ex} = 68.67$ N, $J = 1000$.
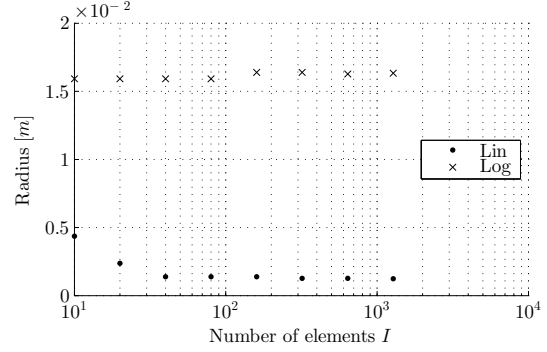
Figure 4.12: Maximum error location as function of I for $h_0 = 50 \cdot 10^{-6}$ m, $F_{ex} = 68.67$ N, $J = 1000$.
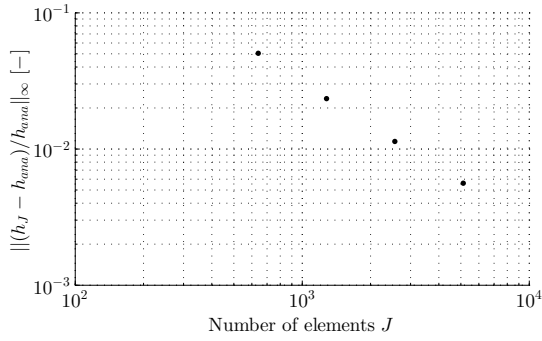
Figure 4.13: Relative error in height as function of J for $h_0 = 50 \cdot 10^{-6}$ m, $F_{ex} = 68.67$ N, $I = 1000$.
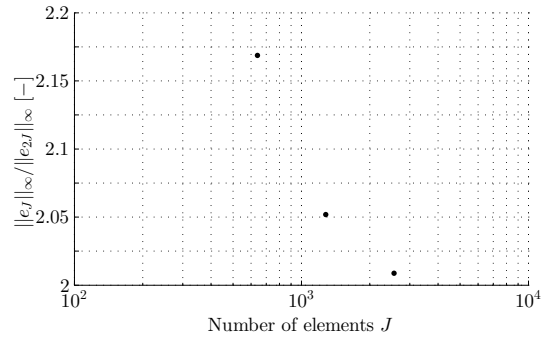
Figure 4.14: Height error ratio as function of J for $h_0 = 50 \cdot 10^{-6}$ m, $F_{ex} = 68.67$ N, $I = 1000$.

then

$$\frac{||e_J(t)||_\infty}{||e_{2J}(t)||_\infty} \geq 2. \tag{4.85}$$

Herein, $h_J(t)$ denotes the numerical solution for J intermediate intervals at time t, h_{ana} is the analytic solution at time t, and the vector e_{2J} contains only the mutual spatial points of e_J. Figure 4.13 shows the relative maximum errors between the numeric and analytic solution in the height as function of J. It is clearly seen that the relative error is decreasing if J increases. Figure 4.14 shows the ratio of the maximum errors. As can be seen, the ratio of the maximum errors converges to 2 if J increases, as expected.

4.2   Compressible fluids

In the previous section, the incompressible Reynolds equation was considered. In the following, a numerical solution method for the compressible Reynolds equation

$$\frac{1}{r}\frac{\partial}{\partial r}\left(r\frac{\rho h^3}{12\mu}\frac{\partial p}{\partial r}\right) = \frac{\partial \rho h}{\partial t}, \tag{4.86}$$

Dynamic behavior of thrust air bearings

is derived. If it is assumed that the viscosity is uniform and the fluid temperature is uniform and constant in time, equation (4.86) can be rewritten as

$$\frac{1}{r}\frac{\partial}{\partial r}\left(rh^3\frac{\partial p^2}{\partial r}\right) = 24\mu\frac{\partial ph}{\partial t}. \tag{4.87}$$

Here, use is made of the ideal gas law

$$p = \rho R_s T \tag{4.88}$$

and

$$\frac{\partial p^2}{\partial r} = 2p\frac{\partial p}{\partial r}. \tag{4.89}$$

First a numerical solution method is derived. Then the difference between the compressible and incompressible fluid film model is investigated. Furthermore, the convergence behavior of the numerical method is assessed.

4.2.1 Numerical solution method

The finite difference method and first order backward Euler integration method are used again to approximate the spatial derivative and time derivative, respectively. An elaboration on the application of these methods for solving the compressible Reynolds equation as a function of time is given below.

Application of the central finite difference on the spatial derivative at r_i results in

$$\frac{1}{r_i}\left[\frac{1}{\frac{1}{2}(\Delta r_{i-1} + \Delta r_i)}\left(rh^3\frac{\partial p^2}{\partial r}\bigg|_{i+\frac{1}{2}} - rh^3\frac{\partial p^2}{\partial r}\bigg|_{i-\frac{1}{2}}\right)\right] = 24\mu\frac{\partial ph}{\partial t} \tag{4.90}$$

where $\Delta r_i = r_{i+1} - r_i$ and $\Delta r_{i-1} = r_i - r_{i-1}$. Note that the discrete grid as shown in Figure 4.3 is used again and that the time indexes j are omitted for simplicity. The two remaining spatial derivatives can be approximated by applying the central finite difference again, giving

$$rh^3\frac{\partial p^2}{\partial r}\bigg|_{i+\frac{1}{2}} = \frac{1}{2}\left(r_i h_i^3 + r_{i+1}h_{i+1}^3\right)\frac{p_{i+1}^2 - p_i^2}{\Delta r_i} \ \vee \ \left(\frac{1}{2}(r_{i+1} + r_i)\right)\left(\frac{1}{2}(h_{i+1} + h_i)\right)^3\frac{p_{i+1}^2 - p_i^2}{\Delta r_i} \tag{4.91}$$

and

$$rh^3\frac{\partial p^2}{\partial r}\bigg|_{i-\frac{1}{2}} = \frac{1}{2}\left(r_{i-1}h_{i-1}^3 + r_i + h_i^3\right)\frac{p_i^2 - p_{i-1}^2}{\Delta r_{i-1}} \ \vee \ \left(\frac{1}{2}(r_i + r_{i-1})\right)\left(\frac{1}{2}(h_i + h_{i-1})\right)^3\frac{p_i^2 - p_{i-1}^2}{\Delta r_{i-1}}. \tag{4.92}$$

Note that for the bearing in Figure 4.1 it will hold that $h_i = h \ \forall \ i$ (uniform height). For simplicity only the first approximation in (4.91) and (4.92) is used. Substituting (4.91) and (4.92) in (4.90) yields

$$C_3\left(C_1\frac{p_{i+1}^2 - p_i^2}{\Delta r_i} - C_2\frac{p_i^2 - p_{i-1}^2}{\Delta r_{i-1}}\right) = 24\mu\frac{\partial ph}{\partial t} \tag{4.93}$$

Here

$$C_1 = \frac{1}{2}\left(r_i h_i^3 + r_{i+1}h_{i+1}^3\right), \tag{4.94}$$

$$C_2 = \frac{1}{2}\left(r_{i-1}h_{i-1}^3 + r_i h_i^3\right), \tag{4.95}$$

and

$$C_3 = \frac{1}{\frac{1}{2}r_i\left(\Delta r_{i-1} + \Delta r_i\right)}. \tag{4.96}$$

Equation (4.93) can be rewritten as

$$\frac{C_3 C_2}{\Delta r_{i-1}}p_{i-1}^2 - C_3\left(\frac{C_2}{\Delta r_{i-1}} + \frac{C_1}{\Delta r_i}\right)p_i^2 + \frac{C_3 C_1}{\Delta r_i}p_{i+1}^2 = 24\mu\frac{\partial ph}{\partial t} \tag{4.97}$$

For simplicity this is written as

$$c_{1,i}p_{i-1}^2 + c_{2,i}p_i^2 + c_{3,i}p_{i+1}^2 = 24\mu\frac{\partial ph}{\partial t} \tag{4.98}$$

where

$$c_{1,i} = \frac{C_3 C_2}{\Delta r_{i-1}}, \quad c_{2,i} = -C_3\left(\frac{C_2}{\Delta r_{i-1}} + \frac{C_1}{\Delta r_i}\right), \quad c_{3,i} = \frac{C_3 C_1}{\Delta r_i}. \tag{4.99}$$

Application of the first order backward Euler integration method on the time derivative is used to obtain an implicit notation of (4.98) with respect to time

$$c_{1,i,j+1}p_{i-1,j+1}^2 + c_{2,i,j+1}p_{i,j+1}^2 + c_{3,i,j+1}p_{i+1,j+1}^2 = 24\mu\frac{p_{i,j+1}h_{i,j+1} - p_{i,j}h_{i,j}}{t_{j+1} - t_j}. \tag{4.100}$$

Combining (4.100) and the boundary conditions

$$\begin{aligned} p &= p_{in} \quad \text{at} \quad r = R_1, \\ p &= p_a \quad \text{at} \quad r = R_2 \end{aligned} \tag{4.101}$$

results in the following grid function in zero form

$$\begin{cases} p_{i,j+1} - p_{in} = 0 & \forall i : r_i = R_1 \\ c_{1,i,j+1}p_{i-1,j+1}^2 + c_{2,i,j+1}p_{i,j+1}^2 + c_{3,i,j+1}p_{i+1,j+1}^2 - 24\mu\frac{p_{i,j+1}h_{i,j+1}-p_{i,j}h_{i,j}}{t_{j+1}-t_j} = 0 & \forall i : R_1 < r_i < R_2 \\ p_{i,j+1} - p_a = 0 & \forall i : r_i = R_2 \end{cases} \tag{4.102}$$

This can be written as a non-linear system of equations

$$\underline{f}_{comp}(\underline{p}_{j+1}) = \begin{bmatrix} p_{0,j+1} - p_{in} \\ c_{1,1,j+1}p_{0,j+1}^2 + c_{2,1,j+1}p_{1,j+1}^2 + c_{3,1,j+1}p_{2,j+1}^2 - 24\mu\frac{p_{1,j+1}h_{1,j+1}-p_{1,j}h_{1,j}}{t_{j+1}-t_j} \\ \vdots \\ c_{1,I-1,j+1}p_{I-2,j+1}^2 + c_{2,I-1,j+1}p_{I-1,j+1}^2 + c_{3,I-1,j+1}p_{I,j+1}^2 - 24\mu\frac{p_{I-1,j+1}h_{I-1,j+1}-p_{I-1,j}h_{I-1,j}}{t_{j+1}-t_j} \\ p_{I,j+1} - p_a \end{bmatrix} = \underline{0}. \tag{4.103}$$

Newton's method can be used to find the root of (4.103) if $\underline{h}_j$ and $\underline{h}_{j+1}$ are known. Hence, the Jacobian of $\underline{f}_{comp}$ is needed which is

$$\mathbf{J}_{comp} = \begin{bmatrix} 1 \\ 2c_{1,1}p_0 & 2c_{2,1}p_1 - 24\eta\frac{h_i}{t_{j+1}-t_j} & 2c_{3,1}p_2 \\ & \ddots & \ddots & \ddots \\ & & 2c_{1,I-1}p_{I-2} & 2c_{2,I-1}p_{I-1} - 24\eta\frac{h_i}{t_{j+1}-t_j} & 2c_{3,I-1}p_I \\ & & & & 1 \end{bmatrix}. \tag{4.104}$$

Note that in (4.104) the index $j + 1$ is omitted. The first order backward Euler equation (4.103) is solved with a regula falsi method.

The regula falsi method is implemented in the following solution procedure to compute the numerical solution $h(t)$ for a time dependent external force $F_{ex}(t)$ starting from an initial height $h(t_0) = h_0$ with $\frac{\partial ph}{\partial t} = 0$. Figure 4.15 gives a scheme for this procedure. Then, Newton's method is used to find a static pressure distribution $\underline{p}_0$ from (4.103). Subsequently, the static load capacity is computed using

$$F_{ab}(\underline{p}) = \pi R_1^2 p_{in} - \pi R_2^2 p_a + 2\pi\frac{1}{2}\sum_{i=0}^{I-1}\left[(r_{i+1} - r_i)(r_{i+1}p_{i+1} + r_i p_i)\right] \tag{4.105}$$

Set IC: $t_0 = 0$, $\underline{h}_0 = \underline{h}(t_0)$, $\frac{\partial ph}{\partial t} = 0$, $j = 0$

Determine $\underline{p}_0$ with Newton's method (4.103) and compute $F_{ab,0}$ (4.105)

$m = 1$, $\underline{h}_{j+1}^0 = \underline{h}_j$, $\underline{h}_{j+1}^1 = 0.9\underline{h}_j$

Solve $\underline{f}_{comp}(\underline{h}_{j+1}^m, \underline{h}_j, \underline{p}_j, \underline{p}_{j+1}^m) = \underline{0}$ for $\underline{p}_{j+1}^m$ (4.103), fig (4.16)

$j = j+1$

Compute $F_{ab,j+1}^m(\underline{p}_{j+1}^m)$ (4.105)

$m = m+1$ Solve $F_{ex,j+1} = a^m\underline{h}_{j+1}^{m+1} + b^m$ for $\underline{h}_{j+1}^{m+1}$ (4.108)

$\|\underline{h}_{j+1}^{m+1} - \underline{h}_{j+1}^m\| < \varepsilon$ no

$\underline{h}_{j+1} = \underline{h}_{j+1}^{m+1}$ yes

$t_{j+1} = t_J$ no   yes

Stop

Variables

t : Time
$\underline{h}_j^m$: Gap height vector
$F_{ex,j}$: External force at t_j
$\underline{p}_j$: Pressure distribution in r at t_j
F_{ab} : Air bearing force
a^m : $= (F_{ab,j+1}^m - F_{ab,j+1}^{m-1})/(\underline{h}_{j+1}^m - \underline{h}_{j+1}^{m-1})$
b^m : $= F_{ab,j+1}^m - a^m\underline{h}_{j+1}^m$
ε : Stop criterion for m iteration

Sub/Superscripts

j : Nodal value in time
m: Iteration number

Remarks

$F_{ab,j+1}^0$: Static load capacity
J : Last time node

Figure 4.15: Solution scheme for solving the height as function of time.

where $\underline{p} = \underline{p}_0$. Then a height $\underline{h}_{j+1}^m$ at the next time instant is guessed where m denotes the mth guessed value for the time instant $j+1$. For this guess a value of 0.9 times the height at the previous time instant is used because it is expected that the height will monotonically decrease.

$$\underline{h}_{j+1}^1 = 0.9\underline{h}_j. \tag{4.106}$$

In the first time step, $\underline{h}_0$, $\underline{h}_1^1 = 0.9\underline{h}_0$ and $\underline{p}_0$ are substituted in (4.103) and (4.104) and Newton's method is used to find the root $\underline{p}_1^1$. Figure 4.16 gives the solution scheme for Newton's method. The force caused by $\underline{p}_1^1$ on the air bearing is computed with (4.105). The balance of forces states that this force must be equal to the external applied force

$$F_{ex,j+1} = F_{ab,j+1}(\underline{p}_{j+1}(\underline{h}_{j+1})). \tag{4.107}$$
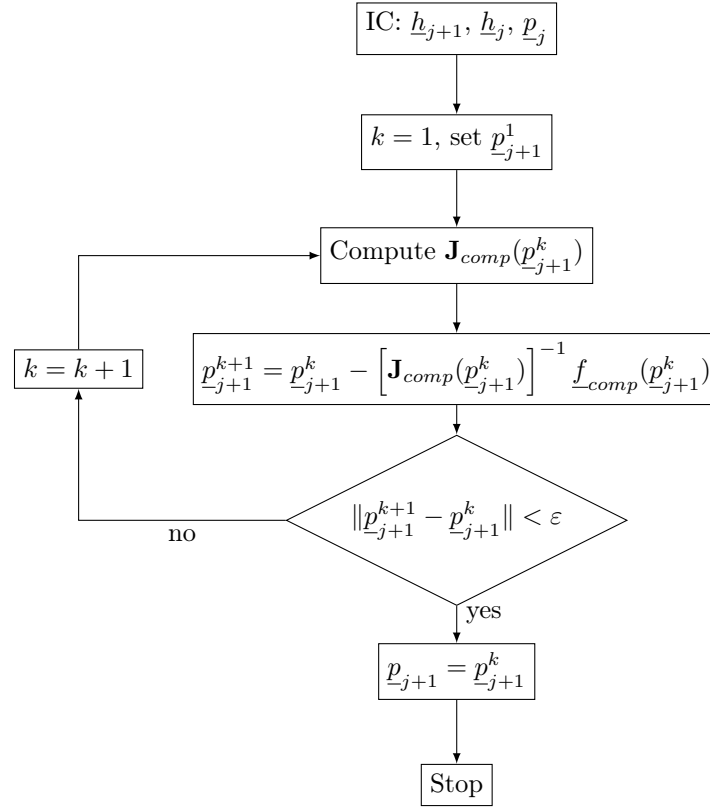
Figure 4.16: Solution scheme for Newton's method.

Using the regula falsi method (4.107) is rewritten into

$$F_{ex,j+1} = \frac{F_{ab,j+1}^m - F_{ab,j+1}^{m-1}}{\underline{h}_{j+1}^m - \underline{h}_{j+1}^{m-1}} h_{j+1}^{m+1} + F_{ab,j+1}^m - \frac{F_{ab,j+1}^m - F_{ab,j+1}^{m-1}}{\underline{h}_{j+1}^m - \underline{h}_{j+1}^{m-1}} \underline{h}_{j+1}^m. \tag{4.108}$$

Equation (4.108) is then used to compute a new guess for $\underline{h}_1$ namely $\underline{h}_1^2$. Herein, the previous guess $\underline{h}_1^0 = \underline{h}_0$ and the current guess $\underline{h}_1^1 = 0.9\underline{h}_0$ are used as the boundaries in the regula falsi method. The new guess is compared with the current guess. If the difference is too large a new pressure distribution and air bearing force is computed with the new guess. This is iterated until the difference between the new guess and current guess is small enough. If the difference is small enough the last guess is accepted as the solution of $\underline{h}_1$. Then the above described process is repeated for the next time instant where the first guess for the height is 0.9 times smaller than the height at the previous time instant.

4.2.2 Results

Figure 4.17 gives the static pressure distribution of the bearing under consideration for the compressible and incompressible case for the parameter values in Table 4.1. It is clearly seen that the static pressure distribution is higher for compressible fluids than for incompressible fluids. Due to the compressibility, the mass density is not uniform in the radial direction and this effect cannot be neglected. The mass density influence the pressure according to the ideal gas law (4.88). In the compressible case the mass density is uniform and does not influence the pressure distribution. The influence of the mass density results in an overall higher pressure for the compressible fluid film. This difference is also seen in the static load capacity where the compressible load capacity is approximately 72 N and the incompressible load capacity 55 N.

Table 4.2: Maximum differences between iteratively computed relative pressure distributions in Newton's method.

m	$||p^k - p^{k-1}||_\infty / p_a$ [−]
1	$8.579 \cdot 10^{-2}$
2	$2.487 \cdot 10^{-3}$
3	$2.14 \cdot 10^{-6}$
4	$1.124 \cdot 10^{-12}$

Figure 4.18 plots the uniform height response for the compressible and incompressible case. In this simulation the air bearing is subjected to a constant force of $F_{ex} = 200$ N with an initial height of $h_0 = 50$ μm. As can be seen, the height for the compressible case decreases somewhat faster than for the incompressible case.

Figure 4.19 shows the compressible pressure distribution just after the application of an external force of $F_{ex} = 200$ N at $t = 1.3209 \cdot 10^{-8}$ s and after 0.5 seconds. The pressure distribution at $t = 1.3209 \cdot 10^{-8}$ s is increased by approximately $0.22 \cdot 10^5$ N/m^2 compared with the compressible static pressure distribution shown in Figure 4.17. The shape is similar except at the boundaries where the boundary conditions have to be satisfied. This increase in pressure is probably caused by the compressibility of the fluid. Because the gap height decreases very fast initially, this results in a lower volume underneath the bearing. The decrease in volume results in an increase in the density and by the ideal gas law in an increase in pressure. Due to the increased pressure, the air underneath the bearing will start to flow out of the bearing clearance and the density of the fluid underneath the bearing will drop again. Eventually, a steady state pressure distribution is formed that is shown in Figure 4.19 at $t = 0.5$ seconds. For a more elaborate discussion on the initial response of the air bearing see appendix C.2.

Figure 4.20 shows the convergence rate of Newton's method for the computation of the static pressure distribution with $h_0 = 50$ μm. Herein, the relative differences for subsequent computed pressure distributions is used. The numerical values are shown in Table 4.2. It is clearly seen that the maximum difference between the iteratively computed relative pressure distributions decreases quadratic, as expected [4].

Figure 4.21 plots the maximum difference between the dynamic height solutions $\underline{h}$ for the compressible case using $2J$ and J time discretization points for different values of J (evaluating the differences only on the J grid). The results are obtained using a logarithmic spatial grid with $I = 1000$ and a linear time grid between the time points $t = 0$ s and $t = 0.5$ s. As can be seen, the difference between the height solutions becomes smaller if the number of intermediate time intervals J increases. Figure 4.22 depicts the ratios between the maximum difference of a height solution with $2J$ and J where $e_J = ||\underline{h}_{2J} - \underline{h}_J||_\infty$. It can be seen that the ratio is equal to approximately 2, as expected due to the first order backward Euler implementation.

Figure 4.23 shows the maximum difference between the numerical static compressible pressure solutions for $2I$ and I for different values of I. The parameter values in Table 4.1 are again used with a spatial linear grid. It can be seen that the errors between the pressure distributions decrease if the number of intermediate intervals I increases. The rate at which the pressure distributions converge is approximately 4 (quadratic convergence) if I is large enough. This is also seen in Figure 4.22 where $e_J = ||\underline{p}_{2J} - \underline{p}_J||_\infty$. This is as expected because of the central finite difference approximation of the spatial derivatives.

Based on the observations that the errors between the computed solutions decrease if the number of elements in the spatial and time directions increases it can be concluded that the numerical solution converges.
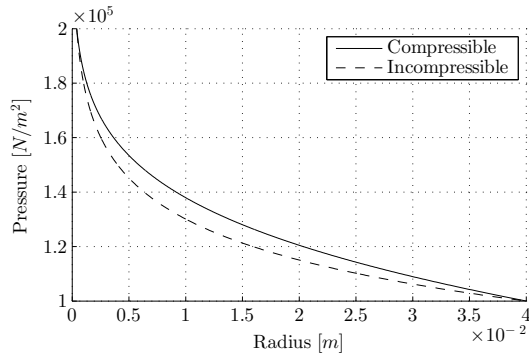
Figure 4.17: Numerically computed static pressure for compressible and incompressible fluids $I = 1000$.
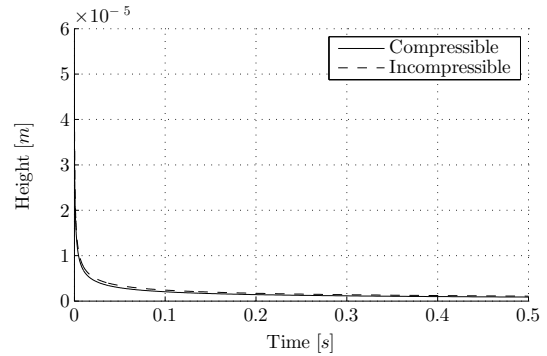
Figure 4.18: Numerically computed solution of $h(t)$ for compressible and incompressible fluids for $F_{ex} = 200$ N $I = J = 1000$.
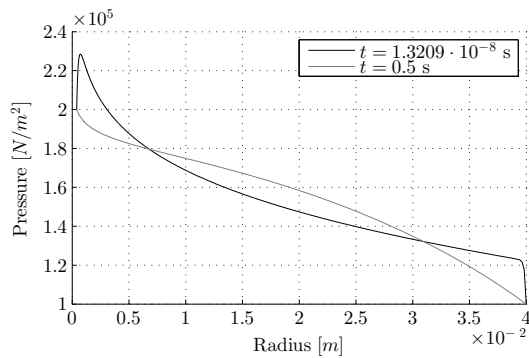
Figure 4.19: Numerically computed pressures for incompressible fluids with $F_{ex} = 200$ N, $I = J = 1000$.
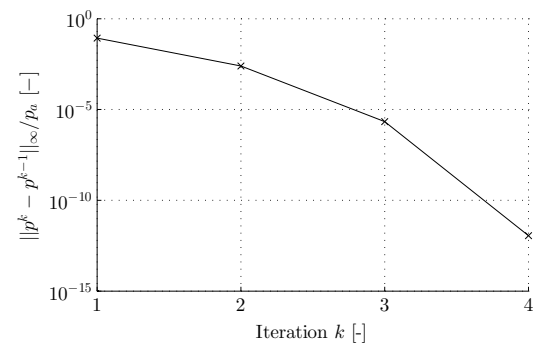
Figure 4.20: Convergence of Newton's method.
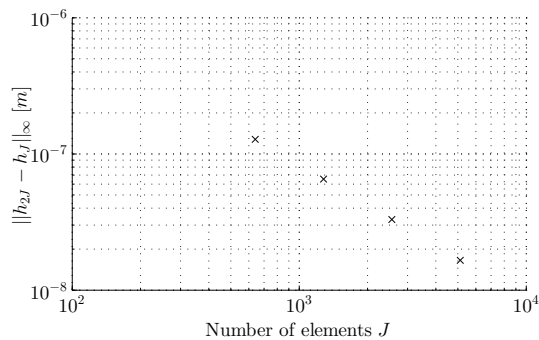
Figure 4.21: Numerical computed errors in height as function of J.
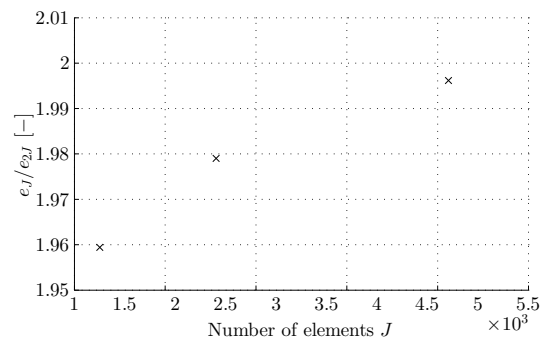
Figure 4.22: Height error ratios as function of J.
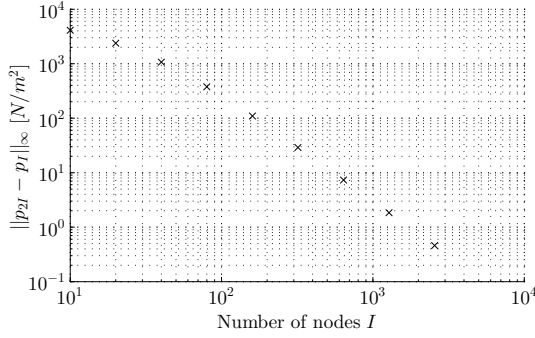
Figure 4.23: Numerical computed errors in pressure as function of I.
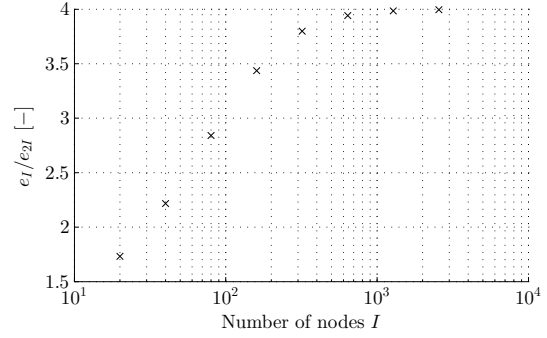
Figure 4.24: Height error ratios as function of I.

4.3 Compressible fluids with orifice restrictor

The function of the orifice in the air bearing is to supply air and generate stiffness. Due to the orifice the pressure underneath the orifice p_o changes as function of the air bearing gap height, while the supply pressure remains constant. The orifice model and the air bearing fluid film model are coupled by the mass flow through the air bearing. It is assumed that the mass flow through the orifice is equal to the mass flow through the air bearing clearance. Two models for the orifice mass flow are considered. First the mass flow through a hole based on Bernoulli's law is considered in subsection 4.3.1. Subsequently, an improved orifice mass flow model by Holster [14] is discussed in subsection 4.3.2.

4.3.1 Orifice model by Bernoulli's law

The mass flow in kg/s of a fluid through a hole based on the compressible Bernoulli equation [14] can be described by

$$\dot{m} = C_d \frac{A_{eff}}{\sqrt{R_s T}} \phi(p_b, p_e) \tag{4.109}$$

where

$$\phi(p_b, p_e) = \begin{cases} p_b \sqrt{\frac{2\kappa}{\kappa-1} \left(\left(\frac{p_e}{p_b}\right)^{\frac{2}{\kappa}} - \left(\frac{p_e}{p_b}\right)^{\frac{\kappa+1}{\kappa}} \right)} & \text{if } \frac{p_e}{p_b} \geq \left(\frac{2}{\kappa+1}\right)^{\frac{\kappa}{\kappa-1}} \\ p_b \left(\frac{2\kappa}{\kappa+1}\right)^{\frac{1}{2}} \left(\frac{2}{\kappa+1}\right)^{\frac{1}{\kappa-1}} & \text{if } \frac{p_e}{p_b} < \left(\frac{2}{\kappa+1}\right)^{\frac{\kappa}{\kappa-1}} \end{cases}. \tag{4.110}$$

Herein, C_d is the dimensionless coefficient of discharge and A_{eff} is the cross sectional area of the hole. Further, R_s is the specific gas constant, T is the fluid temperature, p_b is the pressure at the beginning of the hole, p_e is the pressure at the end of the hole, and κ is the adiabatic expansion coefficient (see also Figure 4.25). The piecewise boundary for $\kappa = 1.405$ is $p_e/p_b = 0.53$.

Equation (4.109) only holds for $p_e \leq p_b$ and positive mass flows $\dot{m} > 0$. The hole mass flow has to be defined piecewise to also take negative mass flows into account for which holds $p_e \geq p_b$. This
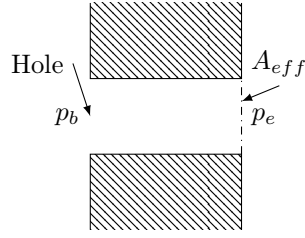
Figure 4.25: Schematical drawing of hole with two different pressures at beginning and end.

results in the following definition for ϕ

$$\phi(p_b, p_e) = \begin{cases} p_b \left(\frac{2\kappa}{\kappa+1}\right)^{\frac{1}{2}} \left(\frac{2}{\kappa+1}\right)^{\frac{1}{\kappa-1}} & \text{if } \frac{p_e}{p_b} < \left(\frac{2}{\kappa+1}\right)^{\frac{\kappa}{\kappa-1}} \\ p_b \sqrt{\frac{2\kappa}{\kappa-1}\left(\left(\frac{p_e}{p_b}\right)^{\frac{2}{\kappa}} - \left(\frac{p_e}{p_b}\right)^{\frac{\kappa+1}{\kappa}}\right)} & \text{if } \left(\frac{2}{\kappa+1}\right)^{\frac{\kappa}{\kappa-1}} \leq \frac{p_e}{p_b} \leq 1 \\ -p_e \sqrt{\frac{2\kappa}{\kappa-1}\left(\left(\frac{p_b}{p_e}\right)^{\frac{2}{\kappa}} - \left(\frac{p_b}{p_e}\right)^{\frac{\kappa+1}{\kappa}}\right)} & \text{if } 1 < \frac{p_e}{p_b} \leq \left(\frac{2}{\kappa+1}\right)^{-\frac{\kappa}{\kappa-1}} \\ -p_e \left(\frac{2\kappa}{\kappa+1}\right)^{\frac{1}{2}} \left(\frac{2}{\kappa+1}\right)^{\frac{1}{\kappa-1}} & \text{if } \frac{p_e}{p_b} > \left(\frac{2}{\kappa+1}\right)^{-\frac{\kappa}{\kappa-1}} \end{cases}. \tag{4.111}$$

This equation is graphically shown in Figure 4.26. Herein, the dotted lines indicate the piecewise boundaries between the four regimes. Equation (4.109) with (4.111) are used to model the mass flow through the air bearing orifice.
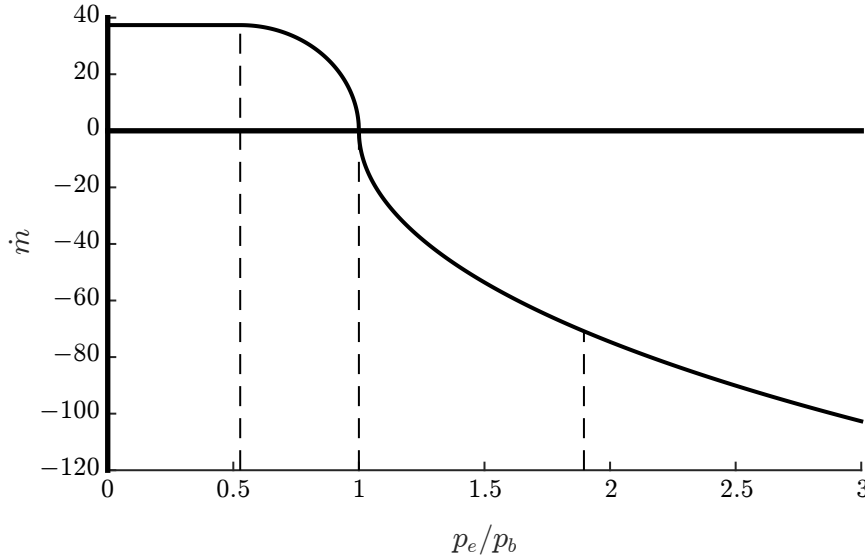
Figure 4.26: Graphical representation of the hole mass flow equation for $R_s = 287$ J/(kgK), $T = 293$ K and $\kappa = 1.405$.

The mass flow at the air bearing gap edge on the orifice side can be computed with the use of the continuity equation. The continuity equation is used in the derivation of the Reynolds equation and follows from the law of conservation of mass stated here as [18]

$$\int_V \frac{\partial \rho}{\partial t} dV = -\int_A \rho \underline{u} \cdot d\underline{A}. \tag{4.112}$$

where $\underline{u}$ is the velocity vector and vector $d\underline{A}$ is defined as $d\underline{A} = \underline{n}dA$ with $\underline{n}$ the unit outward normal to the surface. This equation states that the rate at which the mass changes in a system is equal to the rate at which mass enters the system through the boundaries. In the case of the air bearing under consideration (see Figure 4.1) this can be restated as

$$\int_V \frac{\partial \rho(r,t)}{\partial t} dV = -\int_0^{2\pi} \int_0^{h(t)} \rho(r,t) r u_r|_{R_1} \, dz d\theta + \int_0^{2\pi} \int_0^{h(t)} \rho(r,t) r u_r|_{R_2} \, dz d\theta, \qquad (4.113)$$

where u_r is the fluid velocity in the radial direction. From the Navier-Stokes equation an expression can be found for u_r which was derived in (3.51) and is restated here as

$$u_r = \frac{1}{2\mu} \frac{\partial p(r,t)}{\partial r} (z^2 - hz), \qquad (4.114)$$

where it is assumed that the bearing does not move in the planar directions. Substitution of (4.114) in (4.113) results in

$$\int_V \frac{\partial \rho(r,t)}{\partial t} dV = -\frac{\pi h^3 r \rho(r,t)}{6\mu} \frac{\partial p(r,t)}{\partial r}\bigg|_{R_1} + \frac{\pi h^3 r \rho(r,t)}{6\mu} \frac{\partial p(r,t)}{\partial r}\bigg|_{R_2}. \qquad (4.115)$$

In order to compute the mass flows in the air bearing with the numerical method presented in subsection 4.2.1, (4.115) has to be rewritten to the finite difference form resulting in

$$\int_V \frac{\partial \rho(r,t)}{\partial t} dV = -\frac{\pi h^3 R_1 (p_{0,j} + p_{1,j})}{12\mu R_s T} \frac{p_{1,j} - p_{0,j}}{r_1 - r_0} + \frac{\pi h^3 R_2 (p_{I,j} + p_{I-1,j})}{12\mu R_s T} \frac{p_{I,j} - p_{I-1,j}}{r_I - r_{I-1}}. \qquad (4.116)$$

Here, use is made of the ideal gas law and $p_{i,j}$ and r_i with $i = 0, 1, \ldots, I$ and $j = 0, 1, \ldots, J$ are the pressures and radii underneath the air bearing with the grid defined in Figure 4.3. Note that $r_0 = R_1$ and $r_I = R_2$. The orifice equation (4.109) can be coupled with the air bearing by setting the mass flow of the orifice equal to the first term on the right hand side of (4.116), which is the mass flow at the air bearing gap orifice boundary (at $r = R_1$). Hence,

$$\dot{m}_{gap} = -\frac{\pi h^3 R_1 (p_{0,j} + p_{1,j})}{12\mu R_s T} \frac{p_{1,j} - p_{0,j}}{r_1 - r_0}. \qquad (4.117)$$

This can be simplified to

$$\dot{m}_{gap} = -\frac{\pi h^3 R_1}{12\mu R_s T (r_1 - r_0)} \left(p_{1,j}^2 - p_{0,j}^2 \right). \qquad (4.118)$$

In the previous sections 4.1 and 4.2, the inlet pressure of the air bearing gap p_{in} was prescribed as a boundary condition and the first entry of the pressure solution vector was $p_0 = p_{in}$. In the following, $p_0 = p_{in}$ is set equal to the pressure directly underneath the orifice p_o and the supply pressure p_s is prescribed, see also Figure 4.27. In order to couple the orifice to the air bearing (4.109) as to be equal to (4.118). This can be written in zero notation as

$$\dot{m}_{gap} - \dot{m}_o = 0. \qquad (4.119)$$

Herein $\dot{m}_o$ is described by (4.109) where $p_b = p_s$ and $p_e = p_o$. Further, the dimensionless discharge coefficient C_d is set equal to the dimensionless discharge coefficient of the orifice $C_{d,o}$ and it is assumed that $C_{d,o} = 0.8$ as was done by Holster and Jacobs [14]. Surface $A_{eff} = A_{gap} = 2\pi R_1 h$ if $A_{gap} < A_o$ or $A_{eff} = A_o = \pi R_1^2$ if $A_{gap} > A_o$, see Figure 4.27. The system of equations consisting of (4.119) and (4.102) can be solved with Newton's method. In that case $p_o = p_{in} = p_0$ is an unknown and p_s is prescribed. The same solution scheme as described in section 4.2 can be used
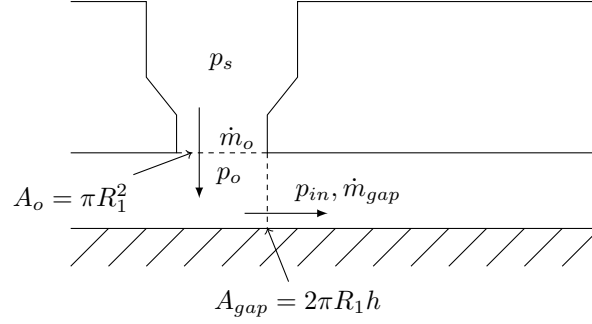
Figure 4.27: Schematical drawing of air bearing with parameters assumed for the orifice model by Bernoulli.

apart form the fact that the system of equations $\underline{f}_{comp}$ and the Jacobian $\mathbf{J}_{comp}$ have changed to

$$\underline{f}_{comp}(\underline{p}_{j+1}) = \begin{bmatrix} \dot{m}_{gap}(p_{0,j+1}, p_1) - \dot{m}_{or}(p_s, p_{0,j+1}) \\ c_{1,1,j+1}p_{0,j+1}^2 + c_{2,1,j+1}p_{1,j+1}^2 + c_{3,1,j+1}p_{2,j+1}^2 - 24\mu\frac{p_{1,j+1}h_{1,j+1}-p_{1,j}h_{1,j}}{t_{j+1}-t_j} \\ \vdots \\ c_{1,I-1,j+1}p_{I-2,j+1}^2 + c_{2,I-1,j+1}p_{I-1,j+1}^2 + c_{3,I-1,j+1}p_{I,j+1}^2 - 24\mu\frac{p_{I-1,j+1}h_{I-1,j+1}-p_{I-1,j}h_{I-1,j}}{t_{j+1}-t_j} \\ p_{I,j+1} - p_a \end{bmatrix} \tag{4.120}$$

and

$$\mathbf{J}_{comp}(\underline{p}_{j+1}) = \begin{bmatrix} \frac{\partial \dot{m}_{gap}}{\partial p_0} - \frac{\partial \dot{m}_o}{\partial p_0} & \frac{\partial \dot{m}_{gap}}{\partial p_1} & & & \\ 2c_{1,2}p_1 & 2c_{2,2}p_2 - 24\eta\frac{h_{j+1}}{t_{j+1}-t_j} & 2c_{3,2}p_3 & & \\ & \ddots & \ddots & \ddots & \\ & & 2c_{1,I-1}p_{I-2} & 2c_{2,I-1}p_{I-1} - 24\eta\frac{h_{j+1}}{t_{j+1}-t_j} & 2c_{3,I-1}p_I \\ & & & & 1 \end{bmatrix}_{j+1} . \tag{4.121}$$

Expressions for $\frac{\partial \dot{m}_{gap}}{\partial p_0}$, $\frac{\partial \dot{m}_o}{\partial p_0}$, and $\frac{\partial \dot{m}_{gap}}{\partial p_1}$ are given in appendix C.3.

4.3.2 Improved orifice model

Holster and Jacobs [14] describe an improved orifice model based on experimental observations of [27]. Figure 4.28 shows this description graphically. First the supply pressure drops from p_s to p_o because the air has to cross the orifice hole with area $A_o = \pi R_1^2$ and discharge coefficient $C_{d,o} = 0.8$. Then the pressure drops again from p_o to p_{th} because the air crosses the air bearing inlet gap with area $A_{in} = 2\pi R_1 h$ and $C_{d,in} = 0.9$. According to [14] a pressure recovery takes place just after the inlet of the air bearing gap described by the K factor

$$K = \frac{p_o - p_{in}}{p_o - p_{th}}. \tag{4.122}$$

The factor K is empirically determined in [27] and can be computed using

$$K = 0.2 + 0.5\left(1 - e^{-\frac{\text{Re}}{1200}}\right)^2. \tag{4.123}$$

where Re is the Reynolds number described by

$$\text{Re} = \frac{\dot{m}_{in}}{\pi R_1 \eta}. \tag{4.124}$$
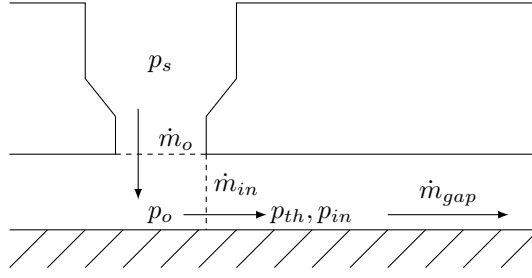
Figure 4.28: Graphical representation of orifice restrictor according to Holster.

.

Figure 4.29 sketches this pressure change across the radius.

The pressure drops across the orifice and inlet gap are described by (4.109), where

$$\dot{m}_o = C_{d,o} \frac{A_o}{\sqrt{R_s T}} \phi(p_s, p_o), \tag{4.125}$$

$$\dot{m}_{in} = C_{d,in} \frac{A_{in}}{\sqrt{R_s T}} \phi(p_o, p_{th}). \tag{4.126}$$

The mass flows through the orifice and inlet gap have to be equal to the mass flow according to the Reynolds equation at the orifice edge as defined in (4.118) which is restated here

$$\dot{m}_{gap} = -\frac{\pi h^3 R_1 (p_0 + p_1)}{12 \eta R_s T} \frac{p_1 - p_0}{r_1 - r_0}. \tag{4.127}$$

Using (4.122), (4.123), (4.124), (4.125), (4.126), and (4.127) the unknown parameters p_o, p_{th}, p_{in}, and $\dot{m}$ can be determined. Because the unknown parameters are described implicitly in the equations above, two functions are introduced

$$f_1(p_{o,j+1}, p_{in,j+1}) = \dot{m}_{gap}(p_{in}) - \dot{m}_{in}(p_o, p_{th}(p_o, p_{in})) = 0, \tag{4.128}$$

$$f_2(p_{o,j+1}, p_{in,j+1}) = \dot{m}_{gap}(p_{in}) - \dot{m}_o(p_o) = 0, \tag{4.129}$$

as done in [14]. This can be written as a set of equations

$$\underline{f}_o = \begin{bmatrix} f_1(p_o, p_{in}) \\ f_2(p_o, p_{in}) \end{bmatrix} = \underline{0}. \tag{4.130}$$

This set of equations (4.130) can be solved together with (4.102). Again, the same solution scheme as described in section 4.2 can be used. Herein, the system of equations $\underline{f}_{comp}$ and the Jacobian $\mathbf{J}_{comp}$ have changed to

$$\underline{f}_{comp}(\underline{p}_{j+1}) = \begin{bmatrix} f_1(p_o, p_{in}) \\ f_2(p_o, p_{in}) \\ c_{1,1,j+1}p_{0,j+1}^2 + c_{2,1,j+1}p_{1,j+1}^2 + c_{3,1,j+1}p_{2,j+1}^2 - 24\mu \frac{p_{1,j+1}h_{1,j+1} - p_{1,j}h_{1,j}}{t_{j+1} - t_j} \\ \vdots \\ c_{1,I-1,j+1}p_{I-2,j+1}^2 + c_{2,I-1,j+1}p_{I-1,j+1}^2 + c_{3,I-1,j+1}p_{I,j+1}^2 - 24\mu \frac{p_{I-1,j+1}h_{I-1,j+1} - p_{I-1,j}h_{I-1,j}}{t_{j+1} - t_j} \\ p_{I,j+1} - p_a \end{bmatrix}$$

$$\tag{4.131}$$

and

$$\mathbf{J}_{comp}(\underline{p}_{j+1}) = \begin{bmatrix} \frac{\partial f_1}{\partial p_o} & \frac{\partial f_1}{\partial p_0} & \frac{\partial f_1}{\partial p_1} & & & \\ \frac{\partial f_2}{\partial p_o} & \frac{\partial f_2}{\partial p_0} & \frac{\partial f_2}{\partial p_1} & & & \\ & 2c_{1,1}p_0 & 2c_{2,1}p_1 - 24\eta\frac{h_{j+1}}{t_{j+1}-t_j} & 2c_{3,1}p_2 & & \\ & & \ddots & \ddots & \ddots & \\ & & & 2c_{1,I-1}p_{I-2} & 2c_{2,I-1}p_{I-1} - 24\eta\frac{h_{j+1}}{t_{j+1}-t_j} & 2c_{3,I-1}p_I \\ & & & & & 1 \end{bmatrix}_{j+1}.$$

(4.132)

The derivatives in $\underline{f}_o$ are given in appendix C.3. Note that the pressure vector $\underline{p}$ has the following form

$$\underline{p} = \begin{bmatrix} p_o \\ p_0 = p_{in} \\ p_1 \\ \vdots \\ p_I \end{bmatrix}.$$

(4.133)

Figure 4.29: Pressure levels underneath the air bearing according to the orifice model of Holster and Jacobs [14].

4.3.3 Numerical validation

Figure 4.30 shows the static load carrying capacity as function of the air bearing gap height for the orifice model based on the Bernoulli equation and the model suggested by Holster and Jacobs [14]. As can be seen, the load carrying capacity is higher for the orifice model by Holster for low gap heights. For gap heights above approximately $45 \cdot 10^{-6}$ m the Bernoulli orifice model shows larger load carrying capacities.

Figure 4.31 plots the static mass flows of the air bearing. These are computed using (4.118). The mass flow in the Holster orifice model is larger for gap heights below approximately $45 \cdot 10^{-6}$ m. For larger gap heights the Bernoulli orifice model has the largest mass flow. Both orifice models will be experimentally validated in the next chapter. Because it is expected that the orifice model by Holster will coincide better with the experimental results this orifice model is used in remainder of this chapter.

Figure 4.32 depicts the height response of a bearing that is initially in a static position with an external force of $F_{ex} = 49.05$ N, and is then suddenly subjected to an external force of $F_{ex} = 70$ N. To obtain this result a logarithmic spatial and linear time grid is used with $I = J = 1000$. The initial height is equal to $h_0 = 3.7 \cdot 10^{-5}$ m. This corresponds to the height in Figure 4.30 at approximately 49.05 N due to gravity. The height initially decreases fast and the velocity decreases

Figure 4.30: Load capacity as function of gap height.

Figure 4.31: Mass flow as function of gap height.

Figure 4.32: Height response with $h_0 = 3.7 \cdot 10^{-5}$ m and $F_{ex} = 70$ N.

until a static height is reached of $2.1 \cdot 10^{-5}$ m. Again, this corresponds with the results shown in Figure 4.30.

4.4 Complete air bearing model

In the previous sections, a solution method to solve the compressible Reynolds equation was proposed in order to model the air bearing lubrication film. In this section, the lubrication film model is combined with a dynamic model of the air bearing. First the dynamic model is described, then a solution method is elaborated to solve the height as function of time for the dynamic model coupled with the lubrication model. Finally, some numerical results are presented.

4.4.1 Dynamic air bearing model
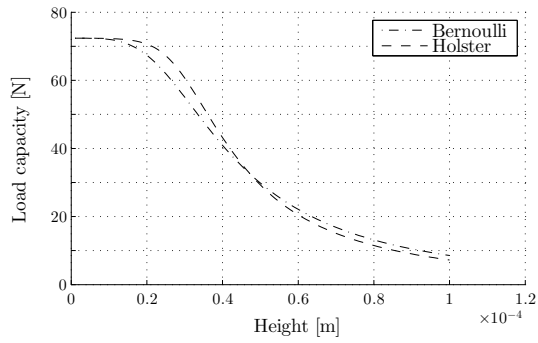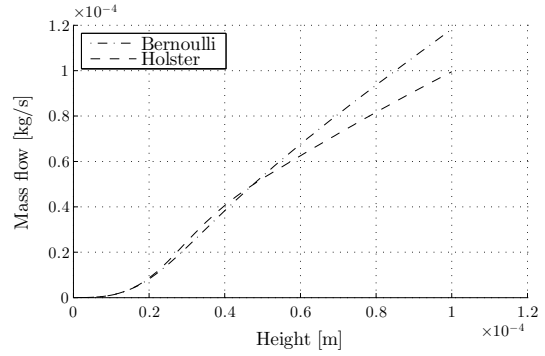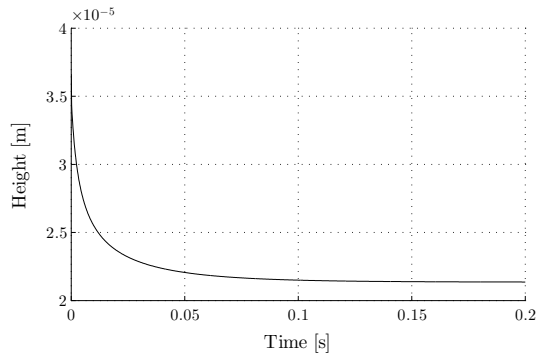
Figure 4.33 schematically shows the dynamic model where the height coordinate is represented by x. In this model, it is assumed that the air bearing can only translate perpendicular to the bearing surface resulting in a one-dimensional model. The air bearing can be modeled as a rigid mass that is subjected to the forces $F_{ab}(x, \dot{x})$ and $F_s(t)$. The force $F_{ab}(x, \dot{x})$ is the force acting on the air bearing due to the air lubrication and can be seen as a non-linear spring-damper. This force is equal to the relative pressure distribution underneath the air bearing integrated over the bearing surface area,

$$F_{ab}(x, \dot{x}) = 2\pi \int_{R1}^{R2} \left[r \left(p(r, x, \dot{x}) - p_a \right) \right] dr + \pi R_1^2 (p_{in} - p_a) \tag{4.134}$$

where $p(r, x, \dot{x})$ follows from the Reynolds equation and p_a is the ambient pressure. The force $F_s(t)$ contains the gravitational force $F_g = Mg$ and the externally applied forces $F_{ex}(t)$

$$F_s(t) = Mg + F_{ex}(t) \tag{4.135}$$

with M the mass of the air bearing and g the gravitational constant. This results in the following equation of motion

$$M\ddot{x} = F_{ab}(x, \dot{x}) - F_s(t). \tag{4.136}$$

This second order ordinary differential equation may be rewritten to a first order vector ordinary differential equation

$$\frac{d\underline{x}}{dt} = \dot{\underline{x}} = \begin{bmatrix} x_2 \\ \frac{F_{ab}(x_1, x_2) - F_s}{M} \end{bmatrix} = \begin{bmatrix} v \\ \frac{F_{ab}(x, v) - F_s}{M} \end{bmatrix} \tag{4.137}$$

where the state $\underline{x}$ is defines as

$$\underline{x} = \begin{bmatrix} x_1 \\ x_2 \end{bmatrix} = \begin{bmatrix} x \\ \dot{x} \end{bmatrix} = \begin{bmatrix} x \\ v \end{bmatrix}. \tag{4.138}$$

4.4.2 Dynamic and lubrication model solution

To obtain a complete dynamic model (4.137) and the fluid film model by (4.98), (4.130), and the outer condition

$$p_I - p_a = 0, \tag{4.139}$$

are coupled by the air bearing force (4.134). The time derivatives in these equations are solved with the Crank-Nicolson method. This ensures second-order accuracy and unconditional stability for the time integration process [4].
Applying the Crank-Nicolson integration scheme ($\Theta = 0.5$) on (4.98) gives

$$p_{i,j+1}x_{i,j+1} - p_{i,j}x_{i,j} - \frac{\Delta t}{24\eta}\Theta \left(c_{1,i,j+1}p_{i-1,j+1}^2 - c_{2,i,j+1}p_{i,j+1}^2 + c_{3,i,j+1}p_{i+1,j+1}^2 \right) -$$
$$\frac{\Delta t}{24\eta} \left(1 - \Theta \right) \left(c_{1,i,j}p_{i-1,j}^2 - c_{2,i,j}p_{i,j}^2 + c_{3,i,j}p_{i+1,j}^2 \right) = 0 \quad \forall i = 1, \dots, I-1. \tag{4.140}$$
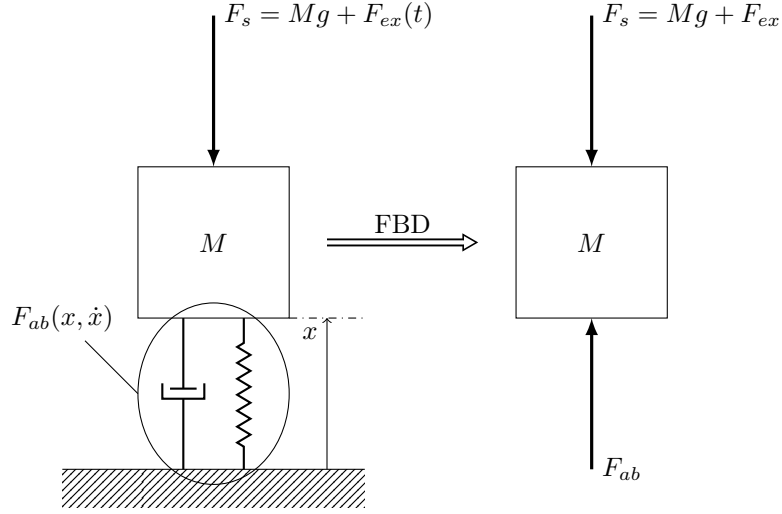
Figure 4.33: Sketch of the assumed dynamic model and free body diagram (FBD).

Applying this scheme to (4.137) yields

$$\underline{F}_1 = \begin{bmatrix} v \\ x \end{bmatrix}_{j+1} - \begin{bmatrix} v \\ x \end{bmatrix}_j - \Delta t \begin{bmatrix} \Theta \left(\frac{F_{ab}((p))_{j+1} - F_{s,j+1}}{M} \right) + (1-\Theta) \left(\frac{F_{ab}((p))_j - F_{s,j}}{M} \right) \\ \Theta v_{j+1} + (1-\Theta) v_j \end{bmatrix} = \underline{0}. \quad (4.141)$$

The air bearing force in (4.141) is computed numerically by

$$F_{ab} = 2\pi \frac{1}{2} \sum_{i=0}^{I-1} \left[(r_{i+1} - r_i) \left(r_{i+1}(p_{i+1} - p_a) + r_i(p_i - p_a) \right) \right] + \pi R_1^2 (p_0 - p_a). \quad (4.142)$$

Combining (4.141), (4.142), (4.130), (4.140), and (4.139) results in a system of non-linear algebraic equations

$$\underline{F}(\underline{y}_{j+1}, \underline{y}_j) = \begin{bmatrix} \underline{F}_1 \\ \underline{F}_2 \\ \underline{F}_3 \\ \underline{F}_4 \end{bmatrix} = \underline{0} \quad (4.143)$$

with

$$\underline{y}_j = \begin{bmatrix} v_j \\ x_j \\ p_{o,j} \\ p_{0,j} \\ p_{1,j} \\ \vdots \\ p_{I,j} \end{bmatrix}. \quad (4.144)$$

Herein $\underline{F}_1$ is defined in (4.141) and

$$\underline{F}_2 = \begin{bmatrix} \dot{m}_{gap}(p_0) - \dot{m}_{in}(p_o, p_0) \\ \dot{m}_{gap}(p_0) - \dot{m}_o(p_o) \end{bmatrix} = \begin{bmatrix} f_{o1} \\ f_{o2} \end{bmatrix}, \quad (4.145)$$

$$\underline{F}_3 = \begin{bmatrix} F_{3,1} \\ \vdots \\ F_{3,I-1} \end{bmatrix} = p_{i,j+1} x_{i,j+1} - p_{i,j} x_{i,j} - \frac{\Delta t}{24\eta} \Theta \left(c_{1,i,j+1} p_{i-1,j+1}^2 - c_{2,i,j+1} p_{i,j+1}^2 + c_{3,i,j+1} p_{i+1,j+1}^2 \right) -$$

$$\frac{\Delta t}{24\eta} (1-\Theta) \left(c_{1,i,j} p_{i-1,j}^2 - c_{2,i,j} p_{i,j}^2 + c_{3,i,j} p_{i+1,j}^2 \right) \quad \forall i = 1, 2, \ldots, I-1,$$
$$(4.146)$$

and

$$\underline{F}_4 = p_{I,j+1} - p_a. \tag{4.147}$$

Here, the Holster orifice model is used but the complete model based on the Bernoulli orifice model is derived analogously.

The above set of equations can again be solved using Newton's method in an iterative way. Therefore, the Jacobian of (4.143) with respect to $\underline{y}_{j+1}$ is needed which is defined here as

$$\mathbf{J} = \frac{\partial \underline{F}}{\partial \underline{y}_{j+1}} = \begin{bmatrix} \mathbf{J}_1 \\ \mathbf{J}_2 \\ \mathbf{J}_3 \\ \mathbf{J}_4 \end{bmatrix}. \tag{4.148}$$

The Jacobian with respect to $\underline{y}_{j+1}$ for $\underline{F}_1$ is

$$\mathbf{J}_1^T = \begin{bmatrix} 1 & -\Delta t\Theta \\ 0 & 1 \\ 0 & 0 \\ -\frac{\Delta t\Theta\pi}{M}\left((r_1-r_0)r_0 + R_1^2\right) & 0 \\ -\frac{\Delta t\Theta}{M}\frac{\partial F_{ab}}{\partial p_1} & 0 \\ \vdots & \vdots \\ -\frac{\Delta t\Theta}{M}\frac{\partial F_{ab}}{\partial p_{I-1}} & 0 \\ -\frac{\Delta t\Theta\pi}{M}\left(\sum_{i=0}^{I-2}\left[-(r_{i+1}-r_i)(r_{i+1}+r_i)\right] - (r_I-r_{I-1})r_{I-1} - R_1^2\right) & 0 \end{bmatrix} \tag{4.149}$$

with

$$\frac{\partial F_{ab}}{\partial p_i} = \pi(r_{i+1}-r_i)r_i + (r_i-r_{i-1})r_i = \pi(r_{i+1}-r_{i-1})r_i \quad \forall \quad i = 1, 2, \ldots, I-1. \tag{4.150}$$

For $\underline{F}_2$ the Jacobian with respect to $\underline{y}_{j+1}$ is

$$\mathbf{J}_2 = \begin{bmatrix} 0 & \frac{\partial f_{o1}}{\partial x_{j+1}} & \frac{\partial f_{o1}}{\partial p_o} & \frac{\partial f_{o1}}{\partial p_0} & \frac{\partial f_{o1}}{\partial p_1} & \underline{0} \\ 0 & \frac{\partial f_{o2}}{\partial x_{j+1}} & \frac{\partial f_{o2}}{\partial p_o} & \frac{\partial f_{o2}}{\partial p_0} & \frac{\partial f_{o2}}{\partial p_1} & \underline{0} \end{bmatrix}. \tag{4.151}$$

Where

$$\frac{\partial f_{o1}}{\partial x_{j+1}} = \frac{\partial \dot{m}_{gap}}{\partial x_{j+1}} - \frac{\partial \dot{m}_{in}}{\partial x_{j+1}} = \frac{\partial \dot{m}_{gap}}{\partial x_{j+1}} - \frac{\partial \dot{m}_{in}}{\partial h} - \frac{\partial \dot{m}_{in}}{\partial p_{th}}\frac{\partial p_{th}}{\partial K}\frac{\partial K}{\partial \dot{m}_{gap}}\frac{\partial \dot{m}_{gap}}{\partial x_{j+1}} \tag{4.152}$$

and

$$\frac{\partial f_{o2}}{\partial x_{j+1}} = \frac{\partial \dot{m}_{gap}}{\partial x_{j+1}}. \tag{4.153}$$

The other derivatives in (4.151) can be found in section 4.3. For $\underline{F}_3$ the Jacobian is

$$\mathbf{J}_3 = \begin{bmatrix} \underline{0}_{[(I-1)\times 1]} & \frac{\partial \underline{F}_3}{\partial x_{j+1}} & \underline{0}_{[(I-1)\times 1]} & \frac{\partial \underline{F}_3}{\partial \underline{p}_{j+1}} \end{bmatrix} \tag{4.154}$$

With

$$\frac{\partial F_{3,i}}{\partial x_{j+1}} = p_{i,j+1} - \frac{\Delta t\Theta}{24\eta}\left(\frac{\partial c_{1,i,j+1}}{\partial x_{j+1}}p_{i-1,j+1}^2 - \frac{\partial c_{2,i,j+1}}{\partial x_{j+1}}p_{i,j+1}^2 + \frac{\partial c_{3,i,j+1}}{\partial x_{j+1}}p_{i+1,j+1}^2\right) \quad \forall i = 1, \ldots, I-1 \tag{4.155}$$

Herein,

$$\frac{\partial c_{1,i,j+1}}{\partial x_{j+1}} = 3x_{j+1}^2\frac{r_i + r_{i+1}}{r_i\left(r_{i+1}-r_{i-1}\right)\left(r_{i+1}-r_i\right)}, \tag{4.156}$$

Table 4.3: Maximum error between iteratively computed solutions in Newton's method.

m	$\|\|\underline{y}^k - \underline{y}^{k-1}\|\|_\infty / p_a \ [-]$
1	$1.983 \cdot 10^0$
2	$1.452 \cdot 10^{-3}$
3	$1.464 \cdot 10^{-6}$
4	$1.919 \cdot 10^{-12}$

$$\frac{\partial c_{3,i,j+1}}{\partial x_{j+1}} = 3x_{j+1}^2 \frac{r_{i-1} + r_i}{r_i \left(r_{i+1} - r_{i-1} \right) \left(r_i - r_{i-1} \right)}, \tag{4.157}$$

and

$$\frac{\partial c_{2,i,j+1}}{\partial x_{j+1}} = \frac{\partial c_{1,i,j+1}}{\partial x_{j+1}} + \frac{\partial c_{3,i,j+1}}{\partial x_{j+1}}, \tag{4.158}$$

if it is assumed that the bearing is flat ($x_i = x_{i+1} \ \forall i$). Further,

$$\frac{\partial F_{3,i}}{\partial \underline{p}_{j+1}} =$$

$$\left[\underline{0}_{[1\times(i-1)]} \quad 2\frac{\Delta t \Theta}{24\eta} c_{1,i,j} p_{i-1,j+1} \quad x_{i,j+1} - 2\frac{\Delta t \Theta}{24\eta} c_{2,i,j} p_{i,j+1} \quad 2\frac{\Delta t \Theta}{24\eta} c_{3,i,j} p_{i+1,j+1} \quad \underline{0}_{[1\times(I-1-i)]} \right] \forall i = 1, \ldots, I-1. \tag{4.159}$$

For $\underline{F}_4$ the Jacobian is

$$\mathbf{J}_4 = \begin{bmatrix} \underline{0}_{[1\times(I+3)]} & 1 \end{bmatrix}. \tag{4.160}$$

Applying Newton's method to find a root of (4.143) results in the following iteration scheme

$$\underline{y}_{j+1}^{k+1} = \underline{y}_{j+1}^k - \mathbf{J}(\underline{y}_{j+1}^k)^{-1} F(\underline{y}_{j+1}^k) \tag{4.161}$$

Where k denotes the kth iteration. The starting point of the time simulation is $\underline{y}_0$ with $v_0 = 0$, x_0 a known height, and $p_{o,0}$ and $\underline{p}_0$ the static pressure distribution determined as explained in section 4.3. After convergence of the iteration scheme (4.161), $\underline{y}_{j+1}^{k+1}$ is set equal to $\underline{y}_j$ and the iteration scheme is started again from $k = 1$ where $\underline{y}_{j+1}^1 = \underline{y}_j$. This is repeated until $j + 1 = J$.

4.4.3   Simulation results

Figure 4.34 shows the gap height response from the static height ($F_{ex} = F_g = Mg$) if the air bearing is suddenly subjected to an external force of $F_{ex} = 70$ N. Both the full model result (the complete air bearing model with inertia) and the lubricant film model (without inertia as derived in chapter 4.3) are plotted. As can be seen, the full model height is initially decreasing less fast than the fluid film model. This is due to the mass of the air bearing that first has to come in motion. Eventually both models converge to the same static height.

Figure 4.35 plots the maximum error between Newton iteration solutions during the first time step of the simulation result shown in Figure 4.34. The values of these errors are given in Table 4.3. The convergence rate is initially linear but becomes quadratic in the last iteration step, as expected.

Figure 4.36 shows the maximum error between height solutions computed with J time elements and $2J$ elements as function of J. For this error analysis a sinusoidal force is used with a frequency of 5 Hz and amplitude of 5 N. As can be seen, the maximum error decreases if the number of elements increases. Because of the Crank-Nicolson implementation for the time derivative it is expected that if the number of elements is doubled the error decreases with a factor 4. Figure 4.37 plots the ratio between the error $e_J = \|\|h_J - h_{2J}\|\|_\infty$ and $e_{2J} = \|\|h_{2J} - h_{4J}\|\|_\infty$. Herein, this behavior is clearly seen.

More simulation results such as the response to an impulse force and a sine-sweep are shown in appendix C.4.
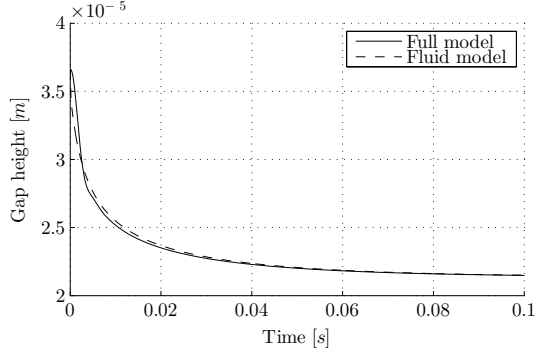
Figure 4.34: Solution of height for $F_{ex} = 70$ N
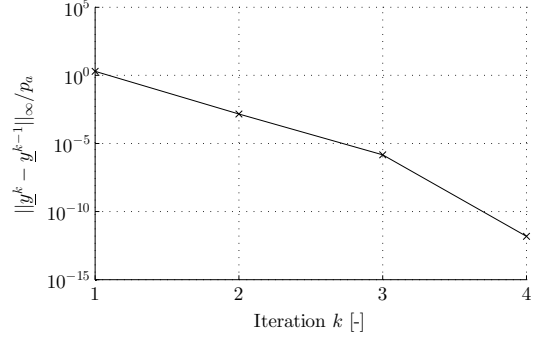
Figure 4.35: Newton convergence in first time step of full model.
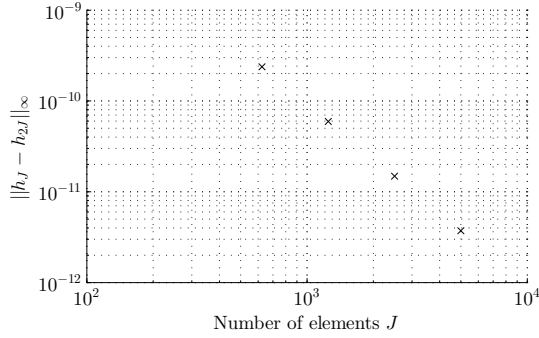
Figure 4.36: Maximum errors in height as function of J.
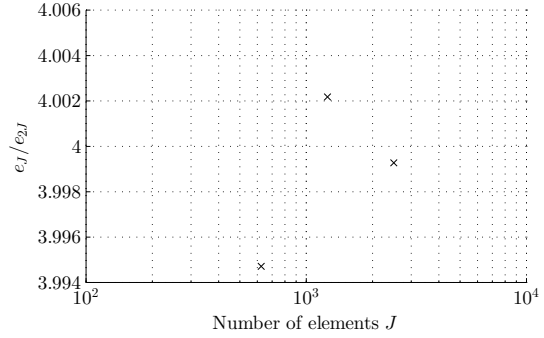
Figure 4.37: Ratio between errors as function of J where $e_J = ||h_J - h_{2J}||_\infty$.

4.5 Summary

First the lubricant film model for incompressible fluids was derived. For this, use was made of the finite difference method for the spatial derivatives. In static situations, the emerging equations were solved with the Gaussian elimination method. In dynamic situations, the time derivative was approximated with the first order forward Euler method. It was observed that the lubricate film acted as a damper. Second, a model for the incompressible lubricate film model was derived. Herein, the time derivatives were approximated by a first order backward Euler method, because of the unconditional stability, and solved with Newton's method. Then, the lubricant film model was extended with an orifice restrictor model to also include stiffness effects into the lubricate film model. Finally, the lubricant film model and a solid dynamics model were combined to obtain a complete dynamic model for the thrust air bearing. Here, the Crank-Nicolson method was used to approximate the time derivative because of the unconditional stability and second order accuracy. Further, all equations were simultaneously solved with Newton's method. For every developed model it was checked if the numerical methods implemented behaved as expected. In the next chapter the developed complete dynamic air bearing model will be compared with experimental data for different load cases and the results will be analyzed.

Chapter 5

Experimental validation of air bearing model

In the previous chapter and specifically section 4.4, a complete air bearing model was developed that combines the Reynolds equation for lubrication with the dynamics of the air bearing model. In this chapter, the results of this air bearing model are compared with experimental data. In this way, the accuracy of the developed model can be assessed. First, the experimental setup is presented in section 5.1. In section 5.2, the static load capacity and mass flow are validated. The frequency response is investigated by comparing sine-sweep results of the model with frequency response measurements in section 5.3. Impulsive force responses are compared in section 5.4 and finally the responses of step forces are investigated in section 5.5.

Figure 5.1: Image of the experimental setup.

5.1 Experimental setup

Figure 5.1 shows an image of the used experimental setup. This setup is schematically shown in Figure 5.2. The setup consists of a T-slot base table on which a large steel block is mounted. On the steel block a Kistler 9061A force transducer is placed with on top of the force transducer the bearing mount plate. On the mount plate the air bearing pad to be investigate is fixed with four bolts. On the bearing pad a bearing counter surface is placed. One side of the counter surface block is flat to make the creation of an air lubrication film possible between the counter surface

Table 5.1: Assumed model parameters used in air bearing analysis.

Parameter symbol	Value	Unit	Quantity
R_1	$2.5 \cdot 10^{-4}$	m	Orifice radius
R_2	$3 \cdot 10^{-2}$	m	Air bearing radius
p_s	T.B.D.	N/m^2	Supply pressure
p_a	10^5	N/m^2	Ambient pressure
T	293	K	Temperature
μ	$1.8205 \cdot 10^{-5}$	kg/(ms)	Viscosity
R_s	287	J/(kgK)	Specific gas constant
κ	1.405	$-$	Adiabatic expansion coefficient
M	1.1	kg	Air bearing nominal mass
g	9.81	m/s^2	Gravitational constant

and the bearing pad. The other side of the counter surface block is spherical with a large radius. On top of this radius a concave bearing pad is placed which is rigidly fixed to a linear guide. The concave bearing pad acts like an air lubricated pivot. This pivot corrects for tilt errors and ensures a parallel gap between the air bearing pad and the flat counter surface. The linear guide where the pivot is attached to, is air lubricated and contains a piston pressure chamber. The pressure in this chamber can be increased to apply an extra load via the piston on the air bearing pad. Note that the setup can be compared with the upside down version of the situation sketched in Figure 4.1. Hence, the air is supplied from underneath and the air bearing is statically mounted and the counter surface is levitated.

Two Lion C7-C capacitive displacement sensors are placed with fixtures above the bearing counter surface as shown in Figure 5.2 to measure the air bearing gap height. The fixtures are mounted with magnets on the large steel block. Further, a Alicat Scientific M-10SLPM-D mass flow meter and a Fluke 700PD7 pressure module are used to measure the fluid mass flow and pressure just before the air bearing pad air outlet. For modal hammer experiments an Endevco model 2302-100 modal hammer is used.

Figure 5.3 shows a one-dimensional dynamical model of the experimental setup. In this model it is assumed that the steel block can be seen as the rigid world. The load cell has a stiffness which is used to measure the force between the rigid world and the bearing mount plate. However, this stiffness is $1.4 \cdot 10^{10}$ N/m and therefore the load cell link is seen as a rigid connection. M_{cs} represents the counter surface mass and is equal to 0.55 kg. This mass is linked via the air bearing lubrication layer to the rigid world. M_g is the mass of the linear guide and is linked by the pivot lubrication layer to the counter surface. The mass of the linear guide M_g is equal to 0.55 kg. The mass of the counter surface M_{cs} and of the guide M_g are used to preload the bearing and give the bearing a nominal gap height for a certain supply pressure. The mass of the guide can be increased, or the piston pressure chamber can be pressurized to adjust the nominal gap height. For the dynamic experiments the pivot air bearing is deactivated just before the experiment. In this way, the counter surface is able to correct for major tilt errors but the pivot lubrication film is not participating in the dynamic measurements.

A flat thrust bearing pad is used with radius $R_2 = 30$ mm and and orifice radius of $R_1 = 0.25$ mm. The experiments are conducted a conditioned room that ensures an almost constant temperature and therefore it is assumed that the temperature remains constant at 293 K. Table 5.1 gives the above described parameters and other assumed parameters used during the simulation of the air bearing model.
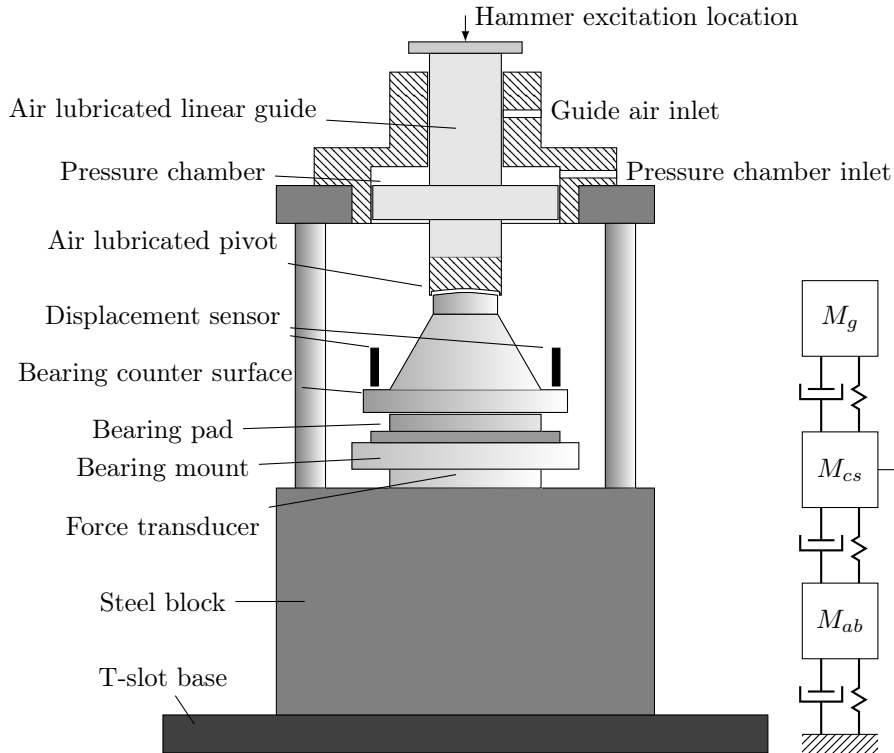
Figure 5.2: Schematic drawing of test setup.
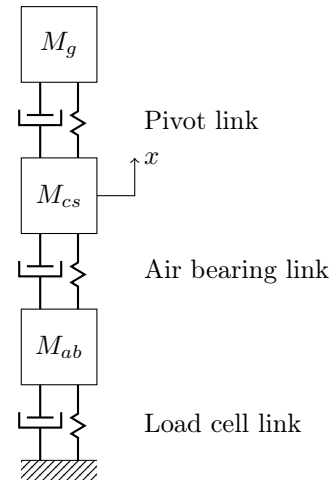
Figure 5.3: Dynamical model sketch of experimental setup.

5.2 Static experiments

An important aspect in air bearing design is the static load carrying capacity of the bearing. Therefore, the simulated static load carrying capacity, with the model described in section 4.3, is validated in this experiment. The mass of the air bearing is increased to $M = M_{cs} + M_g + M_a = 2$ kg to preload the bearing such that the measured gap heights are in range of the displacement sensors. Herein, M_a is an additional mass of 0.9 kg placed on top of the guide. Because in this study only one bearing pad is available and to validate the model for multiple situations, the static load curve is measured for three different supply pressure cases, namely, $p_s = 4$ bar, $p_s = 5$ bar, and $p_s = 6$ bar.

Because the capacitive displacement sensors can only measure a relative position, a zero reference position has to be determined. The zero position of the moving mass is determined by applying a relatively high force of approximately 270 N with the piston integrated in the linear guide. Then the capacitive displacement sensors are set to zero displacement for this height. This is done without pressurizing the air bearing. In this way, it is tried to minimize offset between the two displacement sensors due to tilt of the counter surface. After determining the zero reference position the air bearing is pressurized.

Each measurement series is started by beginning at a force (load carrying capacity) of approximately 20 N due to the weight of the moving part M. The resulting nominal air bearing gap height is seen as the maximum gap height for this measurement series. Then the force is increased with a small step by increasing the pressure in the piston pressure chamber. The moving mass is held on the corresponding height long enough for dynamic effects to damp out before this height is registered. This is repeated with sufficiently small force steps until the two bearing surfaces touched each other. Then the force is decreased again with small steps until the maximum gap

height is reached to make hysteresis effects visible. This sequence of measurements is performed two times per supply pressure to assess the repeatability.

Figure 5.4: Load capacity measurement results for an absolute supply pressure of 4 bar.

Figure 5.5: Mass flow measurement results for an absolute supply pressure of 4 bar.

Figure 5.6: Load capacity measurement results for an absolute supply pressure of 5 bar.

Figure 5.7: Mass flow measurement results for an absolute supply pressure of 5 bar.

Figures 5.4, 5.6, and 5.8 show the measured and simulated load carrying capacity against the nominal gap height for the three supply pressure cases. As can be seen, the measurement results are 3-5 μm shifted to the left compared with the simulated data. This shift is also seen in Figures 5.5, 5.7, and 5.9 where the mass flow against the nominal gap height is shown. Here, the shift is approximately 5-8 μm. Besides the shift, it is also noticed that the measured load carrying capacity for small gap heights is lower than the load capacity predicted by the models. Further, the maximum measured gap height is higher for 5 bar than for 4 bar, as expected. However, for 6 bar the maximum gap height seems equal to that of 5 bar. For these two measurements the counter surface was out of range of the capacitive sensors and therefore the maximum measurable displacement of the sensors was measured. This has no effect on the lower air bearing gap measurement results that are in range of the sensors.

Because the measurement data have a large offset in the displacement compared with the model results, the roughness of the bearing pad surface is investigated. Figure 5.10 shows the roughness measurements in different directions of the air bearing that are plotted over each other. The air bearing profile is measured in 8 directions with a Bruker Dektak stylus profiler. Every measurement
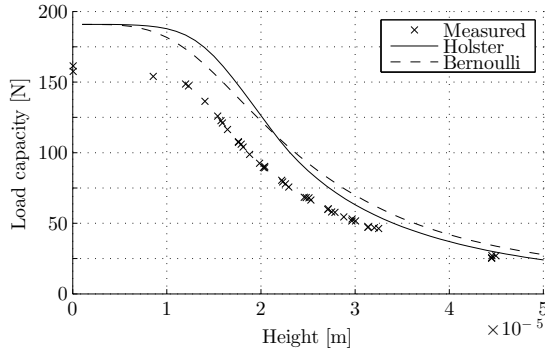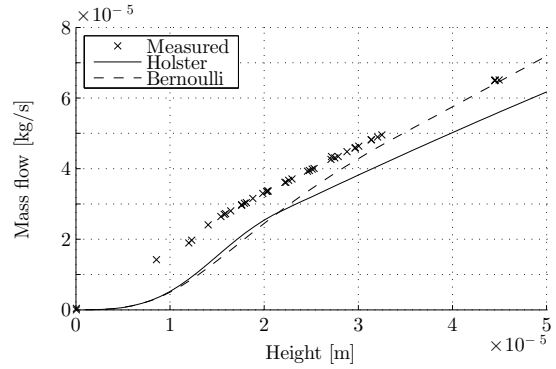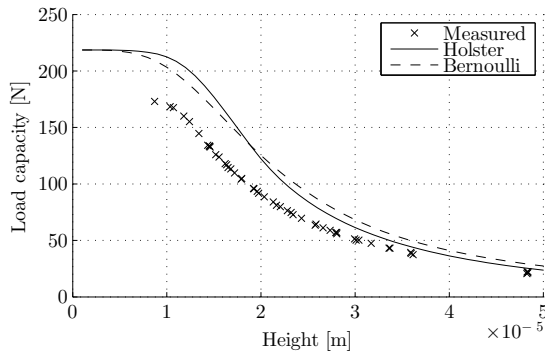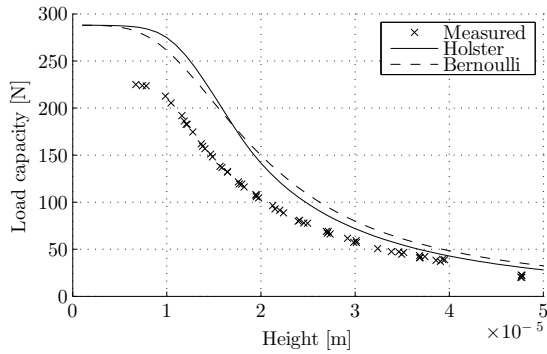
Figure 5.8: Load capacity measurement results for an absolute supply pressure of 6 bar.

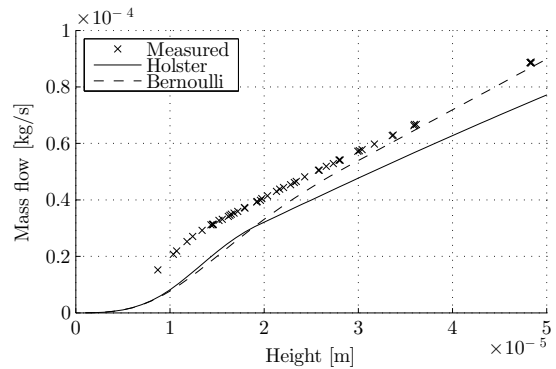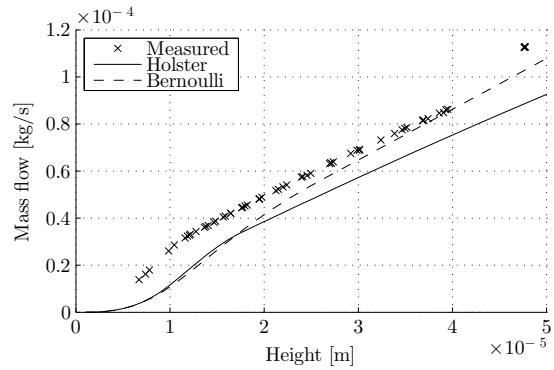Figure 5.9: Mass flow measurement results for an absolute supply pressure of 6 bar.
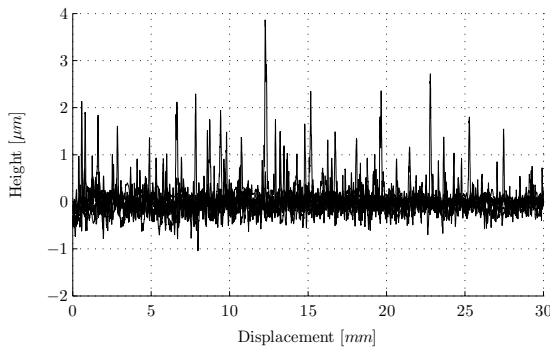
Figure 5.10: Roughness measurement of air bearing.
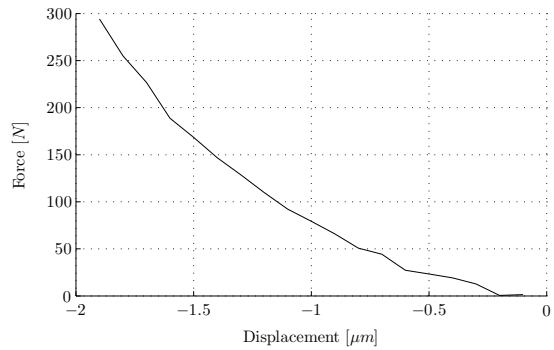
Figure 5.11: Stiffness measurement of air bearing pad (averaged over the two displacement sensors).

is performed from the edge of the air bearing toward the center with intervals of 45°. From these measurements it can be seen that the slope of the air bearing surface is constant. However, peaks with a height of approximately 2 μm can be detected. Inspection of the bearing pad surfaces shows that the surfaces is grinded in only one direction. The peaks in the roughness measurement originate from the measurements orthogonal to the grinding direction and are measured after the execution of the measurements. This means the peaks are not flattened due to the contact between the bearing pad and counter surface. Furthermore, the counter surface has a roughness and profile error smaller than 0.1 μm and thus can be, relative to the bearing pad, considered flat. This indicates that the air bearing has channels with a depth of approximately 2 μm that also contribute in generating a lubrication film. Appendix D.2 gives more details on the measured profiles.

An indication of tilt between the bearing surfaces is seen during the determination of the zero reference position of the two displacement sensors. If the force on the air bearing pad is increased from 20 N (due to the weight of the levitating mass) to 270 N, without pressurizing the air bearing, there is a difference in the displacement between the two displacement sensors of approximately 3 μm. This difference between the two displacement sensors indicates a tilt between the two bearing surfaces. The source of this tilt is unknown and needs further investigation. It could be caused by errors in the assumed flat profile of the bearing pad or a not perpendicular application
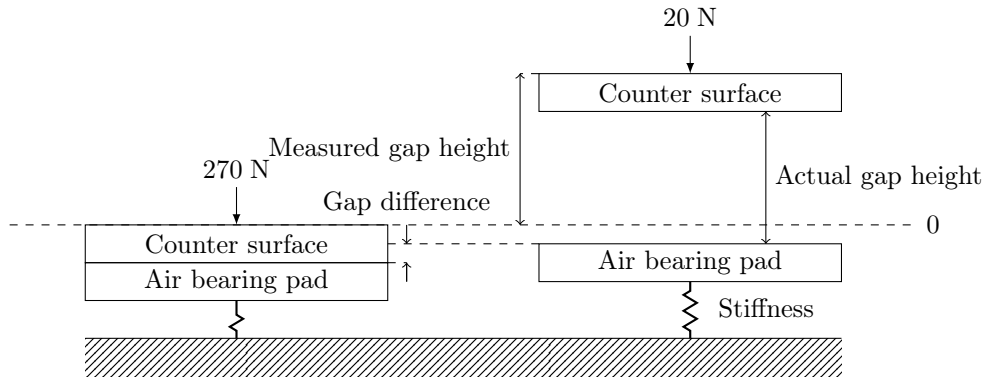
Figure 5.12: Schematic drawing of the effect of stiffness on the experimental setup.

of the piston force on the counter surface.

Furthermore, tilt between the bearing surfaces is seen if the bearing is pressurized. Besides the above mentioned causes the bearing could also tilt due to a misalignment between the orifice hole and the center of the counter surface. The displacement measured by the two sensors is averaged to determine the displacement in the middle of the bearing. Due to the observed tilt, an error of several micrometers is made with respect to the real zero height of the bearing.

Besides the tilt, the negative displacement observed if a force is applied on the not pressurized bearing indicates that there is some mechanical stiffness in the setup. The used force of 270 N is also used in experiments which makes this stiffness significant. Therefore, the stiffness was measured to correct the measurement data for this stiffness. This makes it possible to compare the trend seen in the measurement data with the model.

The stiffness is measured by not pressurizing the air bearing pad and letting the counter surface rest on the bearing pad surface. By increasing the pressure in the piston pressure chamber, the applied load on the bearing pad is increased and the displacement is measured with the displacement sensors. This is done multiple times for and increasing and decreasing force. Figure 5.11 shows the averaged measured air bearing pad stiffness. Note that the force applied in this figure is only caused by the piston in the setup and the bearing is preloaded with $1.1 \cdot 9.81$ N. As can be seen, the height decreases for an increase in the force. If the gap height is measured for a force of 270 N where the displacement sensors are set to zero, then the actual gap height is measured. For lower forces the air bearing pad surface will translate upwards due to the stiffness and the actual gap height is then smaller than measured. This is schematically shown in Figure 5.12.

From the above observations it is concluded that it is difficult to determine the real zero position of the air bearing gap. The observed offset between the measured data and the model results in figures 5.4 - 5.9 relates to this problem. Appendix E contains a sensitivity study to investigate if a deviation in one of the input parameters of the model could cause such a difference. From this analysis it follows that the maximum sensitivity error is in the order of 0.4 μm and the 5 μm shift observed cannot be explained by this. Therefore, more research is needed to develop a reliable method to measure the bearing gap height and zero position.

Further, it is noticed that the measured load capacity is significantly smaller for small gap heights compared to the model. The cause of this is also unknown and needs more research. It might be an effect due to tilt of the two bearing surfaces that becomes significant for small gap heights. This tilt could cause that the supplied air travels via the way of the least resistance, which is in this case the part of the air bearing surface where the distance between the two bearing surfaces is the largest. For larger gap heights the load carrying capacity is smaller and this may cause that on average the load capacity is smaller than expected for tilted air bearings. This tilt could be caused by irregularities in the roughness and profile of the bearing pad. Also, the tilt could be caused by an unknown misalignment of the orifice hole with respect to the bearing counter surface

or a not perpendicular application of the piston force trough the pivot on the counter surface. The developed one-dimensional model is not able to investigate tilt influences. Therefore, a two-dimensional model of the air bearing pad could be developed that makes it possible to investigate tilt and the influence of tilt on the load carrying capacity and stiffness.

From a practical point of view it is difficult to investigate the load capacity for small gap heights because the stiffness of the air bearing decreases rapidly towards zero. If a small error in the applied force is made, this will result in a relative large error in the measured displacement. Besides, disturbances in the externally applied force can push the bearing gap height into a low gap height region. Herein, there is insufficient stiffness to support the bearing and its load, resulting in invalid measurements.

Figure 5.13: Adjusted and shifted load capacity measurement results for an absolute supply pressure of 4 bar

Figure 5.14: Adjusted and shifted mass flow measurement results for an absolute supply pressure of 4 bar
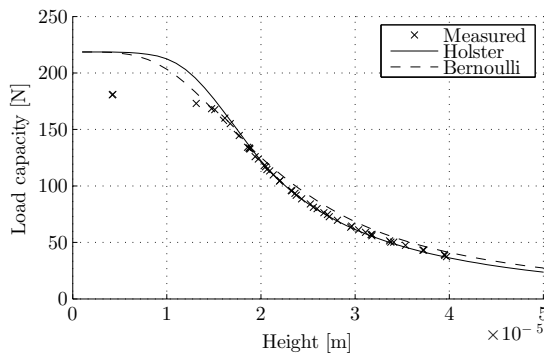
Figure 5.15: Adjusted and shifted load capacity measurement results for an absolute supply pressure of 5 bar
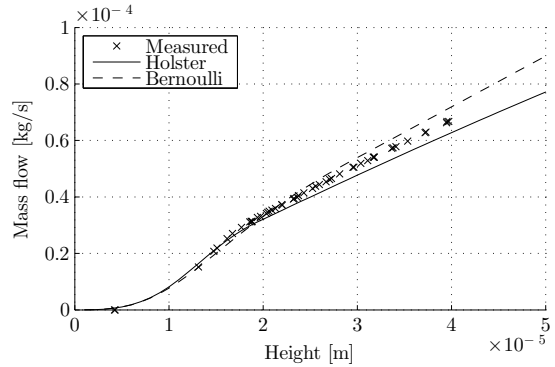
Figure 5.16: Adjusted and shifted mass flow measurement results for an absolute supply pressure of 5 bar

In order to compare the measurement data trend with the results of the two orifice models, the measured data is compensated for the measured bearing pad stiffness. The bearing pad stiffness error is adjusted by interpolating the displacement for the according force and adding it to the measurement result. After that an approximate shift of 5 μm is seen between the experimental and simulated data. In order to compare the trend in the data the experimental data is shifted 5 μm to the right. Figure 5.19 shows the relation between the adjusted and measured gap height for the absolute supply pressure of 4 bar case. For other supply pressure cases the curve is similar.
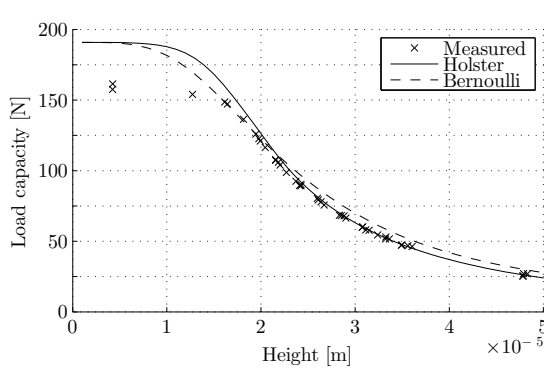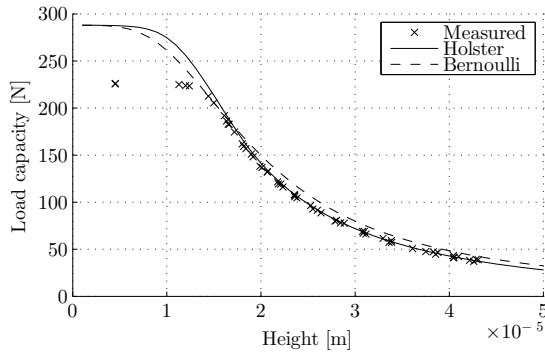
Figure 5.17: Adjusted and shifted load capacity measurement results for an absolute supply pressure of 6 bar

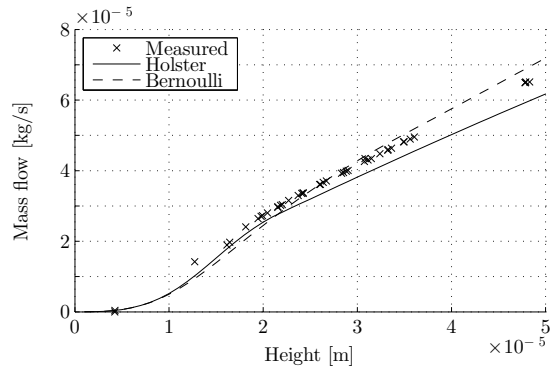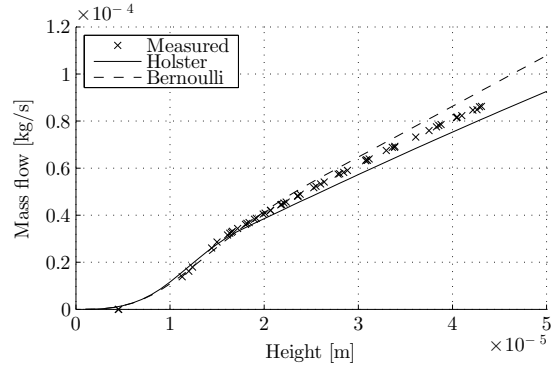
Figure 5.18: Adjusted and shifted mass flow measurement results for an absolute supply pressure of 6 bar
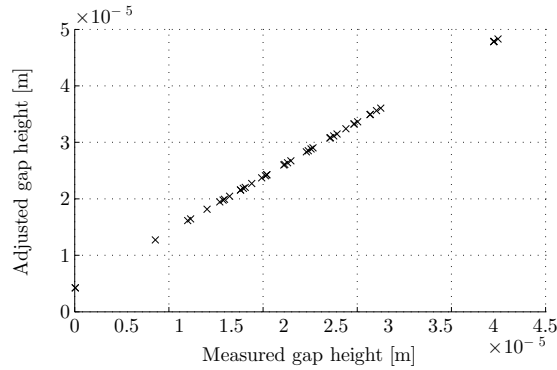
Figure 5.19: Measured gap height versus adjusted gap height for an absolute supply pressure of 4 bar.

Figures 5.13-5.18 shows the stiffness corrected and shifted measurement data.

Figure 5.13 shows the adjusted measured and modeled load capacity for a supply pressure of 4 bar. As can be seen, the slope coincides better with the model of Holster than with the Bernoulli orifice model for large gap heights. If the height decreases the measurement trend starts to deviate and does not correspond with both orifice models. Based on the trend seen in the measurements it may be concluded that the orifice model of Holster coincides best with the measurements.

Figure 5.14 shows the adjusted measured mass flow and the corresponding model data for 4 bar. The measured trend shows a similarity with both orifice models. The difference between the two orifice models is especially good noticeable for large gap heights. The slope of the measurement data is in between the shapes predicted by both orifice models in this region and this makes it difficult to make a statement on which model corresponds best. Furthermore, the discharged coefficients in the orifice model is based on [14]. It might be that if a better approximation of the discharge coefficient can be made, that one of the orifice models corresponds better to the measurement data. This will also influence the error seen in the modeled stiffness of the load carrying capacity plots.

Figures 5.15 and 5.17 show the adjusted measured load capacity and the simulated load capacities for 5 bar and 6 bar, respectively. Figures 5.16 and 5.18 shows the same but now for the mass flow. From these figures the same conclusion can be drawn as was done for the 4 bar case. Based on

the measured data trend for the load capacity it again may be concluded that the orifice model by Holster coincides best with the measurement data. Therefore, the Holster air bearing model is used in the remaining of this study.

5.3 Frequency response experiments

To investigate the gap height frequency response a modal hammer analysis is performed. The air bearing is excited by hitting the levitated mass with a modal hammer in the downward direction. Figure 5.2 shows the location of the modal hammer excitation. The modal hammer has a force transducer in the tip that measures the applied force over time. The average excitation peak force is approximately 10 N. The displacement sensors are used to simultaneously measure the gap height displacement. This measurement is performed for two different masses, $M = 3.6$ kg and $M = 4.45$ kg using the $\hat{H}_1$ estimator $\hat{H}_1 = \hat{S}_{xy}/\hat{S}_{xx}$, in which is averaged over 20 records for each mass. The two different masses allow for a measurement on two different equilibrium heights. The obtained signals are used to estimate the system frequency response with a rectangular window, $f_{nyquist} = 50120$ Hz and, $\Delta f = 1.56$ Hz. A more elaborate description on the computation of the frequency response from the measurement data can be found in Appendix D.

The frequency response of the nonlinear model is determined by simulating a sine-sweep. The force input of the simulation is a sine with a frequency starting at 10 Hz with a amplitude of 0.1 N. For this amplitude, the response behavior is almost linear. This sinusoidal force is applied until the displacement response shows a steady-state output. The resulting amplitude is stored and the frequency is increased with 5 Hz in the same simulation. Again, the simulation is continued until a steady-state output is detected and the new response amplitude is stored. This is repeated until a frequency of 1000 Hz is reached. The output amplitude is defined as $\frac{x_{max}(t) - x_{min}(t)}{2}$ where $x(t)$ is the steady-state response of one period. Assuming linear behavior, to obtain the magnitude-frequency response function the found response amplitudes are divided by the force input amplitude of 0.1 N. The phase is determined by computing the phase difference between the input sinusoid and the response sinusoid with the same frequency as the input sinusoid.

Figure 5.20 shows the frequency response of the measurement for the air bearing with the parameters given in Table 5.1 with a mass of 3.6 kg and a supply pressure of 4 bar of the measurement and the model. As can be seen, the resonance observed at approximately 110 Hz is modeled quite well. The the difference in amplitude is approximately 7 %. Also the simulated phase shows good agreement with the measured phase.

Several resonance peaks are seen in the measurements that are not predicted by the model at 55 Hz, 65 Hz, and 85 Hz. These resonance peaks are caused by the movement of the displacement sensors due to the excitation of the system with the hammer. This indicates that the fixtures holding the displacement sensors are not stiff enough causing the resonances of these fixtures to appear in the frequency response measurement. This is explained in more detail in Appendix D. Further, a deviation of approximately $1.3 \cdot 10^{-7}$ m/N (20 %) in magnitude is noticed between the simulated and the measured FRF for low frequencies. This difference is probably due to a static stiffness of the test setup which is not captured by the model or due to the observed tilt between the bearing surfaces.

Figure 5.21 shows the coherence of the FRF of the air bearing with $M = 3.6$ kg. The coherence is about 1 until 300 Hz except for the frequencies where resonances are visible and at multiples of the net frequency (50 Hz). The coherence deteriorates for frequencies larger than 300 Hz due to a bad signal-to-noise ratio. Overall, the coherence is good in the frequency range of interest which indicates that the behavior is linear.

Figure 5.23 shows the frequency response measurement for an air bearing with a mass of $M = 4.45$ kg and a supply pressure of 4 bar and the corresponding model sine-sweep result. As can be seen the resonance at 115 Hz coincides well with the measurement. The error at this frequency is $0.25 \cdot 10^{-7}$ m/N which is approximately 6 %. Again a difference is noticed in the FRF magnitude for low frequencies of approximately $1 \cdot 10^{-7}$ m/N. The resonance peaks due to the unmodeled flexibility of the test setup are also visible again. Figure 5.22 shows a good coherence at the
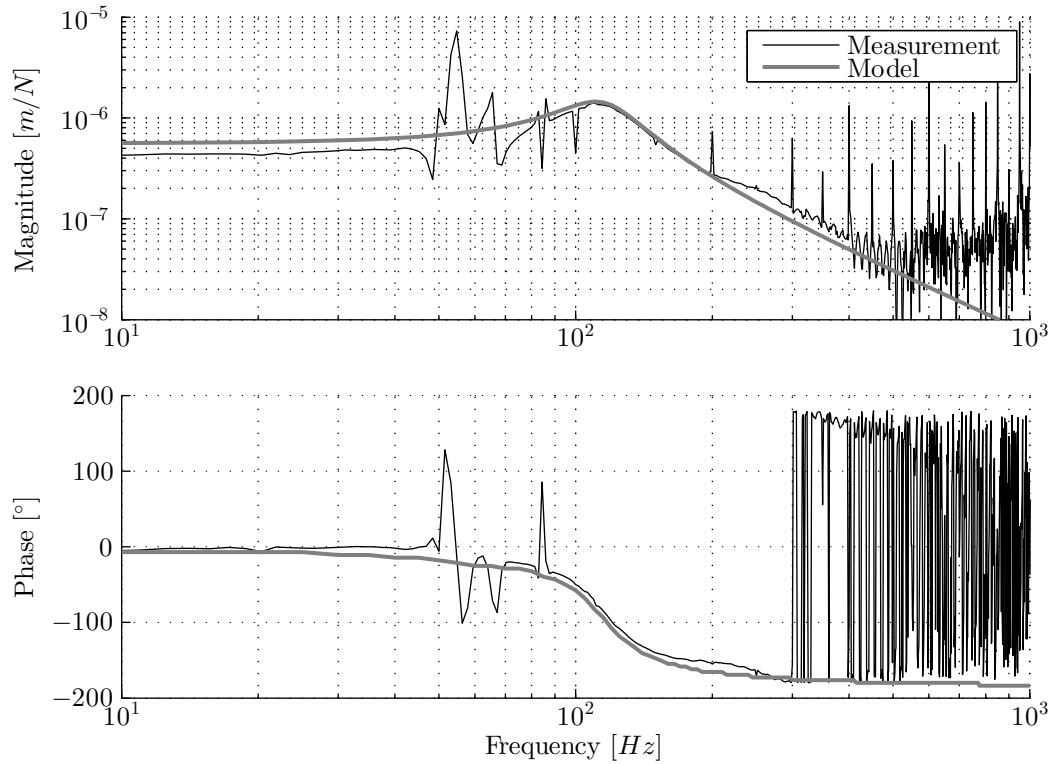
Figure 5.20: Frequency response measurement from the force at the air bearing mass to the gap height for $p_s = 4$ bar, $M = 3.6$ kg.
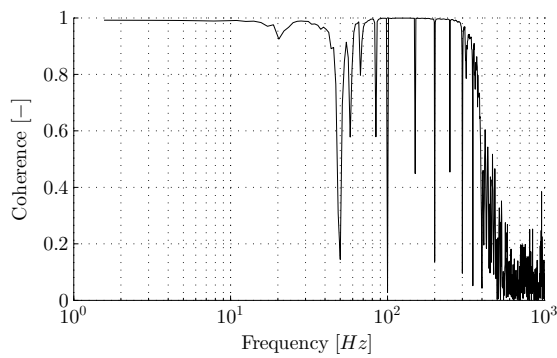
Figure 5.21: Coherence of the frequency response measurement from the force at the air bearing mass to the gap height for $p_s = 4$ bar, $M = 3.6$ kg.
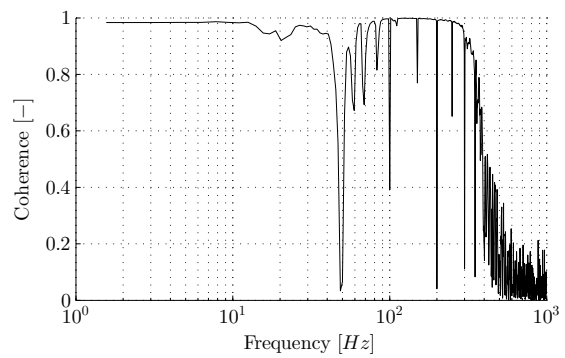
Figure 5.22: Coherence of frequency response measurement from the force at the air bearing mass to the gap height for $p_s = 4$ bar, $M = 4.45$ kg.

resonance frequency and for low frequencies.

If Figure 5.23 is compared with Figure 5.20 it is noticed that the frequency of the resonance has increased from 110 Hz to 115 Hz. For a linear system it is expected that the resonance frequency should decrease because of an increase in mass. However, because the mass is increased the static bearing height is decreased and from Figure 5.13 it can be seen that the stiffness increases if the
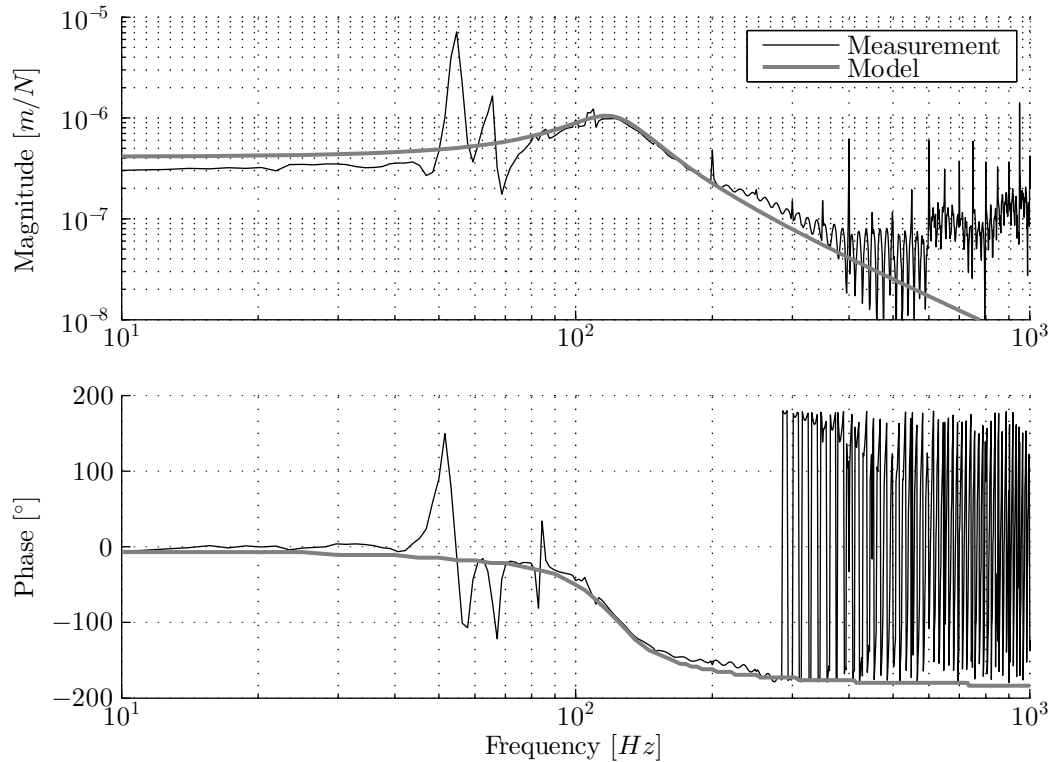
Figure 5.23: Frequency response measurement from the force at the air bearing mass to the gap height for $p_s = 4$ bar, $M = 4.45$ kg.

load is changed from 36 N to 44.5 N. This increase in stiffness is probably higher than the decrease in mass resulting in an increase in the resonance frequency. Appendix D.4 numerically confirms this. In this Appendix, eigenfrequencies of the air bearing used in the experiments are computed for the Holster orifice model and a supply pressure of $p_s = 4$ bar for an air bearing mass of 3.6 kg and 4.45 kg. This is done by computing the stiffness based on the computed load capacity shown in Figure 5.4. It follows that the computed eigenfrequency for the bearing masses 3.6 kg and 4.45 kg are approximately 113 Hz and 119 Hz, respectively. These eigenfrequencies are of the same order as the the observed resonances in Figures 5.20 and 5.23.

5.4 Impulse experiments

In this experiment, starting from a static equilibrium, the moving mass is subjected to an impulse force by hitting the moving part of the setup with a modal hammer. The location of the hammer excitation is again given in Figure 5.2. The air bearing has a moving mass of $M = 3.6$ kg or $M = 4.45$ kg as preload. The moving part of the experimental setup is hit 20 times with a modal hammer in the downward direction. The transient response from the displacement sensors and modal hammer force are recorded. From the 20 measurements the average transient displacement and force is determined. The measured force is used as excitation signal of the Holster air bearing model.

Figure 5.24 shows the measured and simulated gap height response of the air bearing with $M = 3.6$ kg subjected to the measured impulsive force depicted in Figure 5.25. As can be seen, the the equilibrium gap height between the modeled response and measurement differ approximately

Figure 5.24: Impulse measurement results for $p_s = 4$ bar, $M = 3.6$ kg.
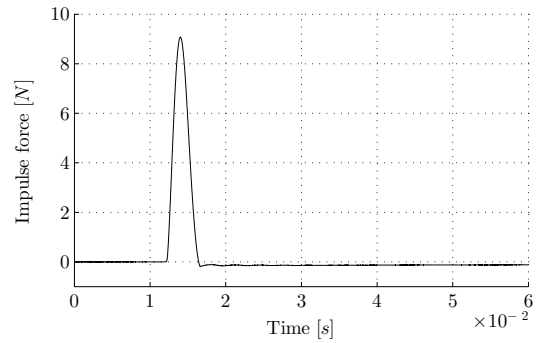
Figure 5.25: Measured input impulse force for $p_s = 4$ bar, $M = 3.6$ kg.

6.5 μm. The observed difference is mainly due to the difficulty in determining the zero position of the air bearing gap as was explained in section 5.2. Figure 5.24 shows also the modeled response with a displacement shift of 6.5 μm (The gray dash-dotted line). The initial response of the measurement is captured well in the model. The error between the minimal gap height of the measurement and the shifted model is 0.16 μm. This is approximately 3 % of the maximum amplitude of the response. The model starts to deviate from the measurement for $t > 3$ s. This is due to the unmodeled resonance at 55 Hz and 65 Hz resonance in the displacement sensor fixtures.

Figure 5.26: Impulse measurement results for $p_s = 4$ bar, $M = 4.45$ kg.
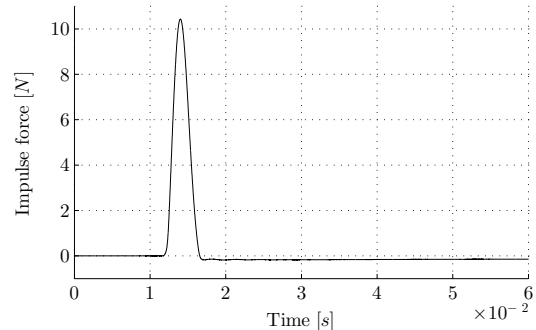
Figure 5.27: Measured input impulse force for $p_s = 4$ bar, $M = 4.45$ kg.

Figure 5.26 shows the simulated and measured impulse response for a mass of $M = 4.45$ kg with the measured force impulse depicted in Figure 5.27. It can be seen that due to the increased mass the nominal gap height is decreased. The modeled gap height is again 6.5 μm higher than the measured gap height. Shifting the model 6.5 μm down shows that the initial response of the model coincides well with the measurement. The error in the maximum amplitude of the response between the shifted model and the measurement is approximately 3 %. Also in this case the model and measurement start to deviate for longer times due to the 55-65 Hz components in the measurement.

The observed error of 3 % in the response magnitude is probably larger than measured. This is because the resonances at 55 and 65 Hz will also contribute to the measured response. The exact contribution is difficult to predict because the magnitudes of these frequency components are determined by the force input and it is difficult to predict at which time these components become dominant.

The time between the minimum gap height and the first peak is approximately $0.5 \cdot 10^{-2}$ s. This corresponds to a period time of $1 \cdot 10^{-2}$ s and a frequency of approximately 100 Hz. This frequency is of the same order as seen in the frequency response measurements, as expected.

5.5 Step experiments

The experiments to validate a step response due to a step load are performed as follows. The zero position of the air bearing gap is first determined. Then the air bearing is pressurized with a supply pressure of 4 bar. subsequently, the moving mass of the experimental setup is lifted manually approximately 5 μm from the equilibrium position and then released. The response is then recorded with the displacement sensors and this is repeated 20 times. The average lift height is determined form the averaged response and used as initial condition for the model simulation. Figure 5.28 shows the gap height response starting from the lifted position for a mass of $M = 3.6$ kg. As can be seen, the moving part of the air bearing returns back to an equilibrium position after release. It is clearly seen that the measured response is heavily damped compared to the modeled response. Based on the observations of the impulse response measurements it is expected that the step response should show a similar response. From the impulse response and the modeled step response the gap reaches the nominal gap height again within 0.05 seconds. It is imaginable that the bearing cannot be perfectly released by hand within 0.05 seconds. As a result, the damped response is possibly caused by friction between the hand of the experimenter and the air bearing. Figure 5.29 plots the gap height difference for a mass of $M = 4.45$ kg. The same observation can be made as for the $M = 3.6$ kg case. Based on these results it is useless to compare the model response with the measurement because an invalid experimental method was used. It is suggested to build a test setup that is able to release the moving mass quickly enough, or develop a setup that is able to apply a step force on the bearing in order to validate the step response of the model.
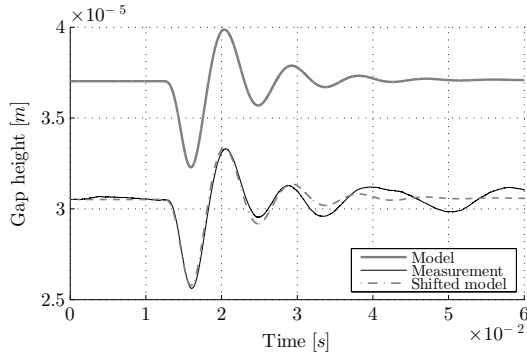

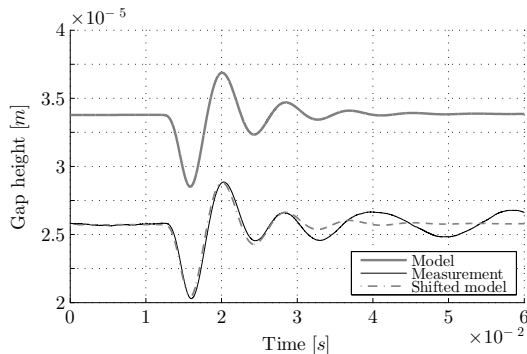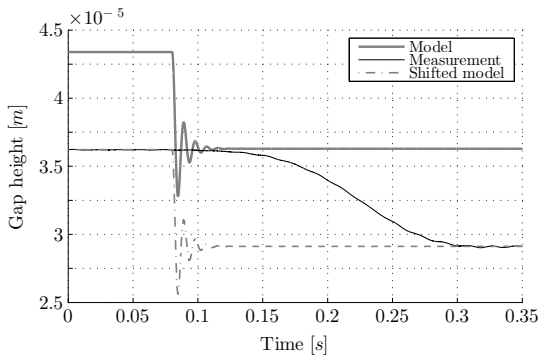Figure 5.28: Step measurement results for $p_s = 4$ bar, $M = 3.6$ kg.
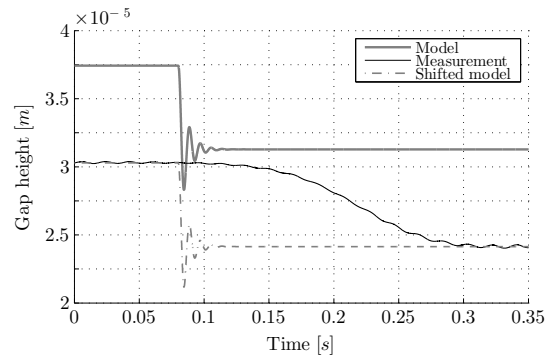
Figure 5.29: Step measurement results for $p_s = 4$ bar, $M = 4.45$ kg.

5.6 Summary

Several experiments were conducted to validate the developed thrust air bearing model. First the gap height as function of a static force was considered. Gap heights were measured which were 5 μm lower than predicted by the model. Further, the measured maximum load capacity was significantly lower than predicted by the model. It was difficult to determine the zero reference gap height during the experiments and therefor there is a large uncertainty in the measured gap height. This is mainly caused by roughness of the bearing pad, unmodeled stiffness in the experimental setup, and an observed tilt between the two bearing surfaces. The observed tilt can

also be responsible for the deviation seen in the maximum load capacity between the model and the measurements.

The frequency response measurements showed a good agreement with the sine-sweep results from the model except for unmodeled setup resonances. The lowest modeled resonance frequency corresponded well with the measurements, with an error in the magnitude of the resonance peaks of about 7 %. Also the measured phase behaved as expected.

After shifting, the maximum displacements as a result of an impulsive force input in the measured and modeled air bearing responses showed a difference of approximately 3 %. This difference is probably higher because the fixtures of the displacement sensors also start to move and this deteriorates the measurement accuracy during the impulse.

The measured step response was qualitatively different compared to the step response predicted by the model. This is probably caused by not quickly enough releasing the air bearing from the initial position. The step response measurements can be improved by using a different releasing method that is quick enough.

Chapter 6

Comparison of models

The developed non-linear model in section 4.4 was validated with experimental results in the previous chapter. In this chapter, this model and the model in section 4.3 are compared with two other alternative air bearing models. The first model is based on an Ansys element that has been developed by Philips to compute the static load capacity of air bearings. The second model is based on the interpolated coefficients method where dynamic coefficients of the air bearing, i.e. linear stiffness and damping coefficients, are retrieved from a database during the simulation. The dynamic coefficients are computed with a FEM Sepran routine developed by Philips. More information on this model can be found in appendix F. Section 6.1 compares the static load capacity predicted by the developed model in section 4.3 and the Ansys model. In section 6.2, the transient gap height response of an air bearing predicted by the developed model in section 4.4 and by the interpolated coefficients model are compared. In this chapter, the parameter values mentioned in Table 6.1 are used.

Table 6.1: Model properties used in simulations.

Parameter symbol	Value	Unit	Quantity
R_1	$2 \cdot 10^{-4}$	m	Orifice radius
R_2	$4 \cdot 10^{-2}$	m	Air bearing radius
p_s	$2 \cdot 10^5$	N/m^2	Supply pressure
p_a	10^5	N/m^2	Ambient pressure
T	293	K	Temperature
μ	$1.8205 \cdot 10^{-5}$	kg/(ms)	Viscosity
R_s	287	J/(kgK)	Specific gas constant
κ	1.405	–	Adiabatic expansion coefficient
M	3.5	kg	Air bearing mass (section 6.2)
g	9.81	m/s^2	Gravitational constant (section 6.2)
I	1000	–	Number of intermediate spatial intervals
J	1000	–	Number of intermediate time intervals (section 6.2)
t_{end}	0.035	s	End time of simulation (section 6.2)

6.1 Static load carrying capacity comparison

Figure 6.1 shows the computed load curve of the air bearing with the Bernoulli orifice model, the orifice model by Holster[14] and the Ansys model. As can be seen, the Bernoulli orifice model deviates from the Ansys and Holster model. It is seen that the Holster orifice model coincides well with the Ansys model, especially for gap heights below 50 μm. For the Ansys model it is known that also the Holster orifice model is implemented, hence this is expected. Considering

---

the complete height range, the RMS of the error in force between the Holster and Ansys model is approximately 0.4 N.
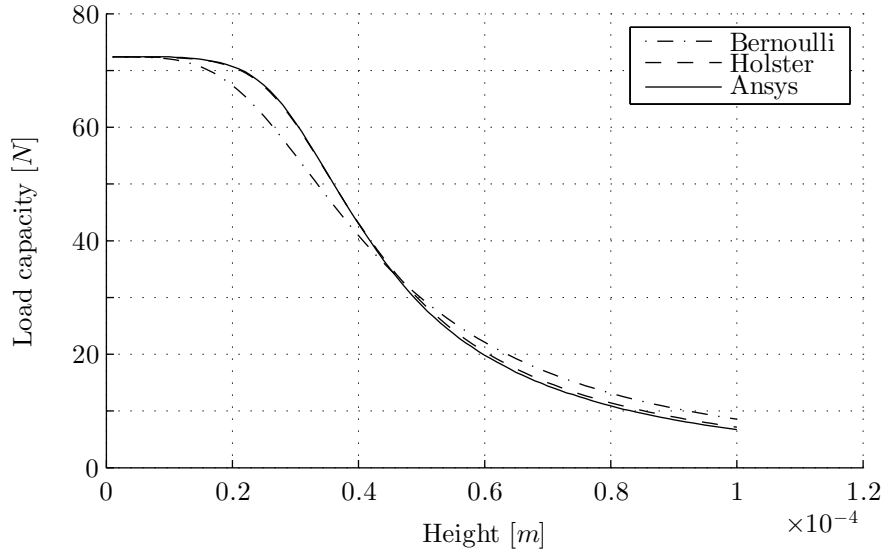
Figure 6.1: Air bearing load curve for Bernoulli orifice model, Holster orifice model, and Ansys model.

6.2 Transient gap height comparison

A transient gap height response due to an impulsive force is calculated with the developed model, a model that uses interpolated coefficients, and with a model linearized around the static equilibrium point. Figure 6.3 shows the impulsive force as a function of time. For the results obtained in this section the values $\hat{F} = 100$ N and $t_{im} = 0.01$ s are used. Appendix F gives more information on the computation of the solution with the interpolated coefficients model. The linearized model uses the stiffness and damping coefficients that are computed at the initial static equilibrium height for the weight $Mg \approx 35$ N. The computation of these coefficients is also explained in appendix F. Figure 6.2 shows the impulse responses for the developed non-linear model, the interpolated coefficients model, and the linearized model respectively. As can be seen, the height in the linearized model is decreasing much further than in the non-linear model and the interpolated coefficients model. The linearized model even predicts that the two bearing surfaces collide and penetrate which is physically impossible. However, the results of the non-linear and the interpolated coefficients model predict that the bearing surfaces will not touch. Furthermore, the initial gap height is recovered after about 0.02 s of the start of the force impulse. This is faster than for the linearized model. The response of the non-linear model and interpolated coefficients model almost coincide. Both models predict that the maximum downward displacement is 29 μm. The difference between these two models in the maximum downward displacement is 0.3 %. The overall RMS error between the non-linear model and the interpolated coefficients model is 1.1 μm.

The computation times for the full non-linear model, interpolated coefficients model, and linearized model are 208 s, 0.05 s and 0.05 s, respectively, for an Intel i7-3537U CPU. Hence, the interpolated coefficients model is faster than the full non-linear model. However, the interpolated coefficients model needs the dynamic coefficients to be computed in advance. For this specific simulation case the computation time of the dynamic coefficients is approximately 2 hours. The dynamic

coefficients are computed for a gap height of 2-50 μm with steps of 1 μm and for 70 frequencies between 1 Hz and $5.6 \cdot 10^7$ Hz on each gap height. These dynamic coefficients can be reused if the load case changes but need to be recomputed if one of the air bearing parameters changes. The above computation time analysis suggests that the choice to use the full non-linear model or the interpolated coefficients model depends on the number of load cases that need to be computed. If a great number of load cases for one bearing configuration need to be computed, it is advised to use the interpolated coefficients model. In other cases the full non-linear model is preferred. The above computation times are specific for the impulisve load case under consideration and can vary greatly for other load cases. Further, the computation time is depending on the time discretization and spatial discretization of the problem. Hence, the computation time break even point between the two models depends on the load case, bearing configuration, and discretization of the problem and needs to be found by trail and error.
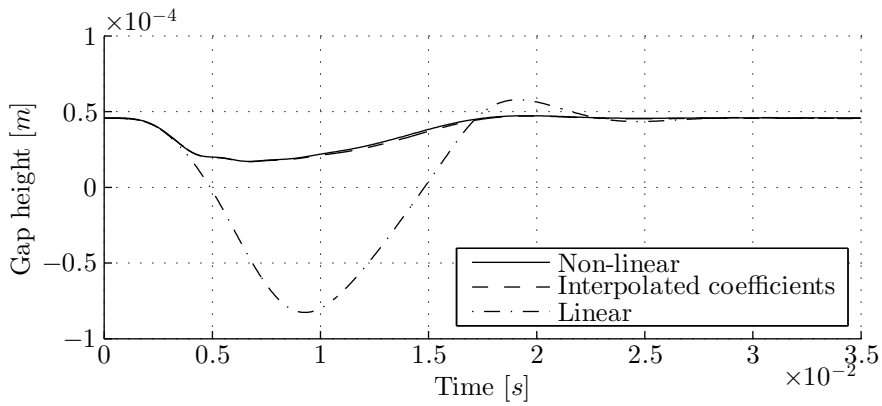
Figure 6.2: Gap height response for air bearing model subjected to an impulse with $\hat{F} = 100$ N and $t_{im} = 0.01$ s.
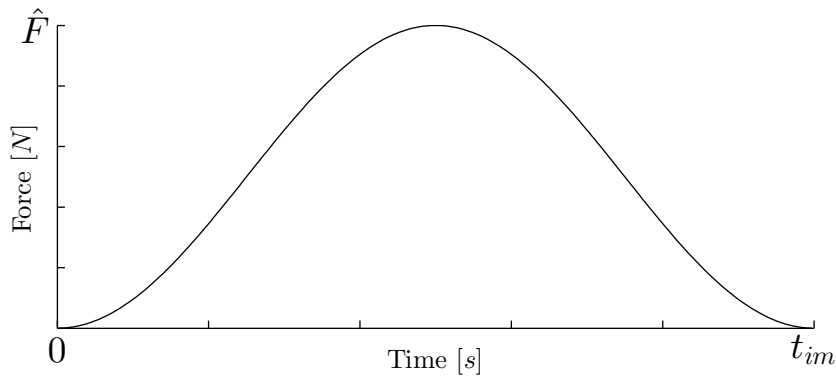
Figure 6.3: Force impulse $F = \hat{F}(\frac{1}{2}\sin(\frac{2\pi}{t_{im}}t - \frac{\pi}{2}) + \frac{1}{2})$ with amplitude $\hat{F}$ and duration t_{im}.

Chapter 7

Conclusions and recommendations

This study aims to develop and validate a thrust air bearing model that can predict the transient behavior of the gap height if the bearing is subjected to a sudden change in load force. The Reynolds equation has been used to model the lubrication film and is coupled to a dynamic solid model to obtain a complete thrust air bearing model. Simulated gap height responses based on this model have been compared with experimental data. Also, the gap height responses based on the proposed model have been compared with responses based on an Ansys FEM model and with responses based on a model that uses interpolated dynamic coefficients. The project objectives mentioned in Chapter 1 are repeated below.

1. Develop a mathematical model to determine the time dependent bearing gap in the air bearing when the applied load changes from a steady-state to a time dependent load, using the transient non-linear Reynolds equation for lubricant flow.

2. Extend the developed mathematical model with the effect of the inertia of the bearing parts on their motion.

3. Validate the developed model experimentally for static loads, harmonic loads, impulsive loads, and step loads.

4. Assess the accuracy of the approximation method that uses interpolated dynamic coefficients for an impulsive load case by comparing the response with the response based on the full non-linear model, see objectives 1 and 2.

First, the conclusions from the present study will be presented. Subsequently, recommendations for future studies will be given.

7.1 Conclusions

A thrust air bearing model has been developed that is able to model the transient behavior of the air bearing gap height. The model consists of a lubricant film model, represented by the Reynolds equation, and the equations of motion for the solid bearing parts. The spatial and time derivatives have been approximated by finite differences. Discretization errors in the calculated gap heights have been assessed and behaved as expected. Hence, the implementations of the numerical solution methods are assumed to be correct.
Load carrying capacity experiments of an thrust air bearing have been performed in which the gap heights resulting from loads have been measured. Measured gap heights are approximately 5 μm smaller than predicted by the model. This difference may be explained by the fact that it is difficult to determine a reference position for the zero gap height. Possible causes are the roughness of the bearing pad surface, a not modeled stiffness in the experimental setup, and tilt between the two bearing surfaces. Despite the observed differences, the trends seen in the load curve measurement

correlated well with the model results. Further, the measured maximum load capacity at small gap heights is smaller than the model result. The exact reason for this is unknown, but a possible cause is the observed tilt in the experimental setup. With the presently developed simulation model it is not possible to determine the effect of tilt on the load carrying capacity of the thrust bearing. Another possible cause is the relative large roughness of the bearing pad which may have a significant effect on the load capacity for small gap heights.

Frequency response measurements have been compared with sine-sweep results from the model. Some unmodeled frequencies have been seen in the measurements and it has been found that these were caused by movement of the fixtures holding the displacement sensors. Apart from the unmodeled frequencies, the measured frequency response coincides well with the frequency response of the model.

Also, the modeled maximum displacement due to an impulsive force agrees well with the measurement. After longer periods of time the measured and modeled impulse response do not coincide due to the experimentally observed frequency components that are caused by the lack of stiffness in the displacement sensor fixtures. The actual difference in the maximum displacement between the model and experimental setup may be larger than observed because of these frequency components.

Comparison of the step response measurements and simulation results shows that the transient behavior does not coincide. Most likely, the attempt to apply a neat step load in the experiment failed. The moving air bearing part is lifted out of the equilibrium position by hand and then released. During this release the gap height response is presumably damped due to interaction between the hand of the experimenter and the moving bearing part.

The static model results have been compared with the model results from an Ansys model where the orifice model is also based on the work of Holster [14]. The static responses are almost similar, indicating that the static part of the developed models has been implemented correctly.

Further, transient responses based on the developed air bearing model have been compared with those obtained by a model that uses interpolated dynamic coefficients, using the same impulsive force. For this analysis, the difference between the transient response results obtained by the developed model and the interpolated coefficient model are very small. This difference is much smaller than the difference between the results obtained from the measurements and the developed simulation model. Therefore, based on this result, it is concluded that the interpolated coefficients model can be used to study the thrust bearing gap height behavior. Because the difference between the full non-linear model and the interpolated coefficients model is small, the choice for one of these models may depend on the computation time. In that case the choice between one of these models depends on the load case, the number of load cases to be computed, the air bearing parameters, and the discretization of the problem.

Despite the differences between the model results and the experimental results it can be concluded that the developed complete non-linear model is able to predict the thrust air bearing gap behavior for a given time dependent force input. All the major differences seen may be caused by error sources in the experimental setup or in the measurement method. In order to obtain a better validation, more experimental research is needed on these error sources.

7.2   Recommendations

The static load carrying capacity measurement data shows a large difference with the model predictions. This is probably caused by difficulties that were encountered during the experiments to determine a reliable zero reference gap height. It is recommended to develop a measurement method that is able to find a reliable zero reference. In this way, the measurements can be made more accurate and a more reliable model validation can be conducted. Furthermore, a tilt is observed between the two bearing surfaces during the measurements and it was seen that the bearing pad surface was relative rough. The influence of this tilt and roughness on the load capacity is unknown and can possibly explain the difference seen in the maximum load capacity. Therefore, it is recommended to develop and analyze a model that includes tilt and roughness

effects in the bearing surfaces Alternatively, it is recommended to polish the bearing surfaces such that the influence of the surface roughness decreases during the measurements.

The values of the discharge coefficients in the orifice models are based on observations of Holster [14]. The simulated mass flow and load carrying capacity may correspond better to the measurement data if a more valid approximation is made of these discharge coefficients. Therefore, it is recommended to investigate if the discharge coefficients can be approximated better.

The frequency response measurements show that the fixtures supporting the displacement sensors are vibrating significantly and affected the transient measurements. It is unknown how large the influence of these vibrations is for other dynamic load situations, e.g. the influence on the maximum impulse response. It is recommended to investigate this by repeating the experiments with stiff fixtures for the sensors.

The measured transient response did not coincide with the simulated response for the case of step loading. This is probably caused by unavoidable interaction between the hand of the experimenter and the air bearing. The step loading experiments can be improved if a method is found that releases the moving bearing part fast enough.

Bibliography

[1] Dal A. and Karaçay T. On dynamics of an externally pressurized air bearing with high values of clearance: Effect of mass flow rate. *Proceedings of the World Congress on Engineering 2014*, 2, 2014.

[2] R.A. Adams. *Calculus: A complete course.* Pearson Addison Wesley, 2006.

[3] Mishra A.K. Dynamic behaviour of aerostatic rectangular thrust bearings. *Wear*, 63:219–229, 1980.

[4] Kendall E. Atkinson. *An introdution to numerical analysis.* John Wiley & Sons, 1978. ISBN: 0-471-02985-8.

[5] Majumdar B.C. Dynamic characteristics of aerostatic thrust bearings with porous inserts. *Journal Mechanical Engineering Science*, 22(2):55–58, 1980.

[6] Cuvelier C., Segal A., and Steenhoven A.A. van. *Finite Element Methods and Navier-Stokes Equations.* D.Reidel Publishing Company, 1986. ISBN: 90-277-2148-3.

[7] Wang C. Bifurcation and nonlinear dynamic analysis of united gas-lubricated bearing system. *Computers and Mathematics with Applications*, 64:279–738, 2012.

[8] Kraker B. de. *A Numerical - Experimental Approach in Structural Dynamics.* Shaker Publishing, 2013.

[9] Al-Bender F. On the modelling of the dynamic characteristics of aerostatic bearing films: From stability analysis to active compensation. *Precision Engineering*, 33:117–126, 2009.

[10] Lin G., Aoyama T., and Inasaki I. A computer simulation method for dynamic and stability analyses of air bearings. *Wear*, 126(307-319), 1988.

[11] Chen G.S. and Chang J.Y. Chaos in nonlinear dynamics of air bearing slider in contact. *Microsystem Technologies*, 20:1739–1744, 2014.

[12] Yabe H. and Mori H. Tanahashi H. A study on characteristics of externally pressurized gas thrust bearings with surface-restriction compensation. *Bulletin of the JSME*, 25(207):1451–1456, 1982.

[13] Bernard J . Hamrock, Steven R . Schmid, , and Bo O . Jacobson. *Fundamentals of Fluid Film Lubrication.* CRC Press, 2004. ISBN: 978-0-8247-5371-9.

[14] P.L. Holster and J.A.H. Jacobs. Theoretical analysis and experimental verification on the static properties of externally pressurized air-bearing pads with load compensation. *Tribology international*, 20(5):276–289, October 1987.

[15] Powel J.W. A review of progress in gas lubrication. *Review of Physics in Technology*, 1(2):96–129, 1970.

[16] White J.W. and Ponnaganti V. Non-linear air bearing dynamics of a six degrees of freedom magnetic recording slider with head-disk contact/impact. *IEEE Transaction on Magnetics*, 24(6):2757–2759, 1988.

[17] Czolczynski K., Brzeski L., and Kazimierski Z. High stiffness gas journal bearing under the step force. *Wear*, 167(1):49–58, 1993.

[18] P.K. Kundu and I.M. Cohen. *Fluid Mechanics*. Academic Press, second edition edition, 2002.

[19] Wei L. and Ruibo Y. Jing L. Computational fluid dynamics of aerostatic bearings with the finite volume method. *2011 IEEE 5th International Conference on Robotics, Automation and Mechatronics (RAM)*, pages 270–274, 2011.

[20] Liu L.X. and Spakovszky Z.S. Effects of bearing stiffness anisotropy on hydrostatic mirco gas journal bearing dynamic behavior. *Journal of Engineering for Gas Turbines and Power*, 129, 2007.

[21] Chandra M., Malik M., and Sinhasan R. Gas bearings part i: Dynamic analysis and solution method. *Wear*, 88:255–268, 1983.

[22] Hassini M. and Arghir M. A simplified nonlinear transient analysis method for gas bearings. *Journal of tribology*, 134:011704, 2012.

[23] Hassini M. and Arghir M. A new approach for the stability analysis of rtors supported by gas bearings. *Journal of Engineering for Gas Turbines and Power*, 136:022504, 2014.

[24] Hassini M. and Arghir M. A simplified and consistent nonlinear transient analysis method for gas bearing: Extenson to flexible rotors. *Journal of Engineering for Gas Turbines and Power*, 137:092502, 2015.

[25] Mahajan M., Jackson R., and Flowers G. Experimental and analytical investigation of a dynamic gas squeeze film bearing including asperity contct effects. *Tribology Transactions*, 51:57–67, 2008.

[26] Majumder M.C. and Majumder B.C. Non-linear transient analysis for an extrnally pressurized porous gas journal bearing. *Wear*, 132(139-150), 1989.

[27] J.T. McCabe, H.G. Elrod, S. Carfagno, and R. Colsher. Summary of investigations of entrance effects of circular gas bearings. *Gas Bearing Symposium, Southampton*, April 1969.

[28] Bhat N., Kumar S., Tan W., Narasimhan R., and Low T.C. Performance of inherently compensated flat pad aerostatic bearings subject to dynamic perturbation forces. *Precision Engineering*, 36:399–407, 2012.

[29] Rao N.S. and Majumdar B.C. An approximate method for the calculation of dynamic stiffness and damping coefficients of externally pressurized porous gas journal bearings. *Wear*, 61:375–379, 1980.

[30] Reynolds O. On the theory of lubrication and its application to mr. beauchamp tower's experiments, including an experimental determination of the viscosity of olive oil. *Philosophical Transactions of the Royal Society of London*, pages 157–235, 1886.

[31] Milovanova O.B., Cheking O.N., and Dyshl M.S. Dynamic characteristics of air bearings. *Translated from Prikladnaya Mekhanika*, 18(9):84–89, 1982.

[32] Matta P., Arghir M., and Bonneau O. Experimental analysis of cylindrical air-bearing dynamic coefficients. *Tribology Transactions*, 53:329–339, 2010.

[33] Zhicheng P., Shugo W., Qingming L., and Wei C. Theoretical and experimental study of the dynamic transient characteristics of a hydrostatic bearing. *Wear*, 160:27–31, 1993.

[34] Fukui S. and Kaneko R. Analysis of ultra-thin gas film lubrication based on the linearized boltzmann equation. *JSME International Journal*, 30(286):1660–1666, 1987.

[35] Yoshimoto S. Static and dynamic characteristics of aerostatic circular porous thrust bearings (effect of the shape of the air supply area). *Journal of Tribology*, 123:501–508, 2001.

[36] Yoshimoto S., Tamura J., and Nakamura T. Dynamict tilt characteristics of aerostatic rectangular double-pad thrust bearings with compound restrictors. *Tribology International*, 32:731–738, 1999.

[37] Andras Z. Szeri. *Fluid film lubrication: theory and design.* Cambridge University Press, 1998. ISBN: 0-521-48100-7.

[38] Waumans T., Al-Bender F., and Reynaerts D. A semi-analytical method for the solution of entrance flow effects in inherently restricted earostatic bearings. In *Proceedings of GT2008 ASME Turbo Expo 2008: Power for Land, Sea and Air*, 2008.

[39] Stolarski T.A. Numerical modeling and experimental verification of compressible squeeze film pressure. *Tribology international*, 43:356–360, 2010.

[40] Witelski T.P. Dynamics of air bearing sliders. *Physics of fluids*, 10(3):698–708, 1998.

[41] Hua W., Yu S., Zhou W., and Myo K.S. A fast implicit algorithm for time-dependent dynamic simulations of air bearing sliders. *Journal of Tribology*, 134:031901, 2012.

[42] Shapiro W. and Colsher R. Implementation of time-transient and step-jump dynamic analyses of gas-lubricated bearings. *Journal of Lubrication Technology*, 1970.

[43] Gross W.A., Matsch L.A., Castelli V., Eshel A., Vohr J.H., and Wildmann M. *Fluid film lubrication.* John Wiley & Sons, New York, 1980.

[44] Choir W.C., Shin Y.H., and Choi C.W. Influences of the restrictor design parameter and opterating conditions of aerostatic bearings on its dynamic characteristics. *JSME International Journal Series C*, 2001.

[45] Smith W.R. Computational results of a dynamic simulation of the conforming shell gas journal bearing. *Tribology International*, 30:151–162, 1997.

[46] Chen X. and Ye Y. Influences of the restrictor design parameter and opterating conditions of aerostatic bearings on its dynamic characteristics. *2009 IEEE/ASME International Conference on Advanced Intelligent Mechatronics*, pages 516–521, 2009.

[47] Haruyama Y., Moir A., Mori H., Mikami F., and Aikawa H. Effects of gas inertia forces on dynamic characteristics of externally pressurized gas-lubricated thrust bearings. *JSME International Journal Series III*, 32(2):303–307, 1989.

[48] Ono Y., Yoshimoto S., and Miyatake M. Impulse-load dynamics of squeeze filme gas bearings for a linear motion guide. *Journal of Tribology*, 131:041706, 2009.

[49] Otsu Y., Miyatake M., and Yoshimoto S. Dynamic characteristics of aerostatic porous journal bearings with a surface-restricted layer. *Journal of Tribology*, 133(011701), 2011.

[50] Yap Y.K. A galerking finite element scheme for the rectangular gas-lubricated slider bearing - the transient case. *Wear*, 105:109–122, 1985.

[51] Ye Y.X., Chen X.D., Hu Y.T., and Luo X. Effects of recess shapes on pneumatic hammering in aerostatic bearings. *Proceedings of the Institution of Mechanical Engineers, Part J: Journal of Engineering Tribolgoy*, 224(3):231–237, 2010.

Appendix A

Literature search

A.1 Introduction

In high precision system equipment often air bearings are used to support movable parts (stages) of the machine. If for some reason a temporarily external force is applied to the movable part of the high precision machine, the air bearing functions as a squeeze damper. The distance between the surfaces of the air bearing decreases and air is squeezed out of the bearing gap. The squeeze motion results in a reaction force by the air on the bearing surfaces and hence the load carrying capacity of the air bearing increases. Depending on the magnitude of the temporarily external force, the movable part of the air bearing is accelerated towards the other bearing surface. The extra load carrying capacity generated by the squeeze motion determines whether the bearing surfaces will touch each other and damage the bearing surfaces. An air bearing design must be such that the bearing surfaces never touch each other. Furthermore, the time needed for the air bearing system to regain a steady state (settling time) must be small for the accuracy of the high precision machine.

This literature review attempts to give answer to the following question: *What models are used in literature to model gas bearings that are valid for large displacements.*

It is preferable that the gas bearing model is applied on a dynamical model and that the bearing is a cylindrical thrust gas bearing. These criteria were not used in the literature review because they would restrict the literature search to much. The following inclusion criteria were used to obtain a set of selected articles:

- The bearing under consideration must be a gas bearing.

- Linearized models are excluded.

- The study is presented in English.

A.2 Data Collection

The databases used to search for literature are:

- Focus (Database of Eindhoven Univesity of Technology),

- Web of Science,

- Scopus.

Because a dynamical model is preferably sought the following search terms were initially used (Air OR Gas OR Aerostatic*) AND Bearing* AND Dynamic*. This resulted in 211 hits in Focus, 381 in Scopus and 240 in Web of Science. The found hits were removed from duplicates and 28 hits were selected based on title and abstract. After scanning the papers the search

---

terms were adapted in order to obtain more papers about the transient behavior of gas bearings resulting in the following search terms (Air OR Gas OR Aerostatic*) AND Bearing* AND (transient OR "large displacement"*. These search terms were used in Web of Science and Scopus resulting in 392 hits in Scopus and 283 hits in Web of Science. After removing duplicates 586 hits remained. From these hits the title and abstract were scanned and this resulted in 8 additional papers. This brings the total selection of papers on 36.

A.3   Data evaluation

Table A.1 gives an overview of the used bearings, governing equations to describe them, solution method to solve the governing equation, if the dynamic coefficients were computed and if there was obtained a full solution.

Air bearing are first of all classified in hydrodynamic and hydrostatic. Hydrodynamic bearings are bearings that generate a lubrication layer due to the relative motion of the two bearing surfaces. If the two bearing surfaces do not move with respect to each other there is also no lubrication layer and no load capacity. Hydrostatic bearings however, use an external lubrication source to create a lubrication layer and can carry loads even if the two bearing surface do not experience relative motion.

Most air bearing types can be hydrostatic or hydrodynamic. Thrust bearings are hydrostatic bearings that make a linear motion while carrying a load. Such a bearing has one or multiple supply holes that supplies the lubricant to the bearing gap with pressure p_{or}, as shown in figure A.1. Due to the pressure difference between the orifice pressure p_{or} and the ambient pressure p_a, a lubricate flow Q and pressure profile will exist. The increased pressure under the bearing pad exerts a force that makes it possible for the bearing to carry a load. In this literature search 11 studies were found that analyze this type of bearing. Herein 8 studies analyzed circular shaped bearings and 3 studies investigated rectangular bearings. Sliders are hydrodynamic linear bearings that have a wedge form as depicted in figure A.2. The wedge forces the lubricant into a small gap due to the relative motion between the bearing surfaces. Because the lubricant is forced under the wedge an increased pressure p_w will occur that exerts a force on the slider. This principle is applied in the design of hard disk drives (HDD) read heads to ensure that the read head hovers above the hard disk. 5 studies with this type of bearing were found. Another hydrodynamic linear bearing is the squeeze film bearing. This type of air bearing has a flexible bearing surface that can be actuated in a vibrating motion, creating a positive pressure across the bearing pad. 3 studies treat this type of bearing. In two instances the squeeze film bearing was rectangular and in the other circular.

Journal bearings allow rotational motion and carry load perpendicular to the rotational axis. Hydrodynamic journal bearings consist of a circular bushing and shaft where the center axis of these components are generally aligned with a small eccentricity ε as shown in figure A.3. Due to the eccentricity the lubrication height varies across the shaft circumference with the minimum height in the direction of the eccentricity. The relative motion between shaft and bushing pressurizes the lubricant in the minimum gap height causing a load carrying capable force. Hydrostatic journal bearings are used if hydrodynamic bearings are not able to support the load, a precise radial position of the bearing is need or to reduce instabilities [43]. These bearings have lubrication sources distributed across the circumference of the bearing as shown in figure A.4. A total of 15 studies were found that investigated journal bearings. In one study they investigated an air mount which is not within the scope of this study. In another paper a general study to air bearings performed by finding a solution of the Reynolds equation for lubrication. This is classified as general under Type in table A.1.

The governing equations to model an air bearing is derived in two parts, The lubrication film model and the dynamical model. The lubrication film models the pressure distribution in the bearing and this is used as input for the dynamical model. The dynamical model models the displacement of the air bearing masses. The Reynolds equation is most used in the modeling of the lubrication film. This partial differential equation is encountered 26 times. The Reynolds
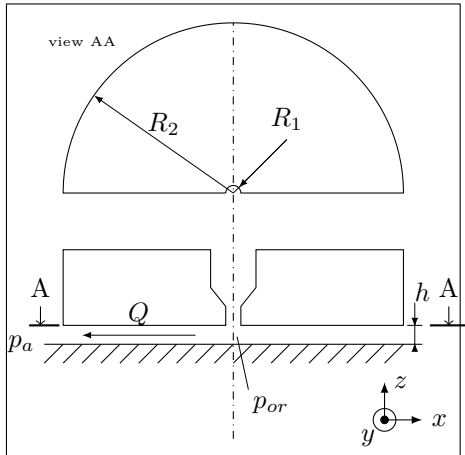
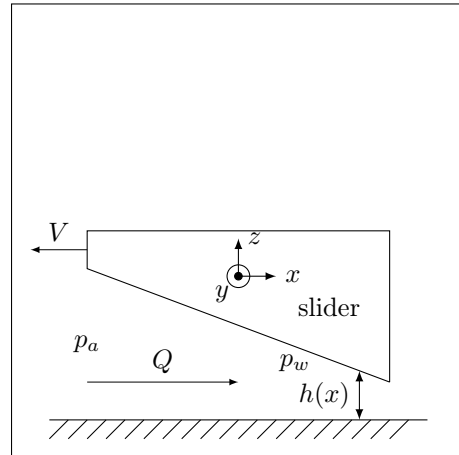Figure A.1: Schematic drawing of a hydrostatic thrust bearing.

Figure A.2: Schematic drawing of a hydrodynamic thrust bearing.
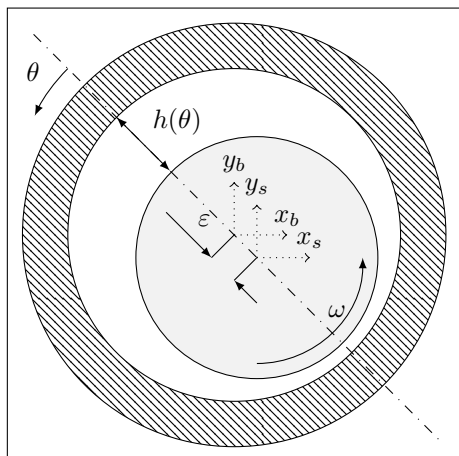

Figure A.3: Schematic drawing of a hydrostatic journal bearing.
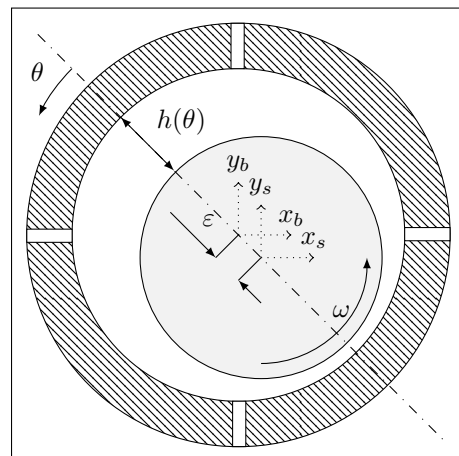

Figure A.4: Schematic drawing of a hydrodynamic journal bearing.

equation was first derived by Osborne Reynolds in 1886 to model thin lubrication films. In 2 instances the Linearized Boltzmann equation is used. In 1 paper the Navier-Stokes equations, equation of continuity and the ideal gas law is used to model the thin film with fluid inertia forces [47]. These are omitted in the Reynolds equation. [20] only uses the dynamic model with stiffness coefficients derived from a lubrication film model. It is not mentioned which equation governs this lubrication model. [32] describes a test setup for journal bearings and does not model the bearing at all. [31] models and air mount and is not further investigated. [49] and [36] use the equation of continuity and resistance network method (RNM) to model the lubrication film. [19] uses the continuity equation, momentum equation and energy equation to model the lubrication film. It is not clear what lubrication model [33] used.

All lubrication models were described by partial differential equations. Different methods were encountered to solve these equations. The most used method in this literature search was the small perturbation method that was used 10 times. This method was used to find the height and frequency dependent dynamic coefficients, stiffness and damping. In 8 cases the finite difference method was used to find a numerical solution and 6 times the finite element method (FEM). Other methods that were encountered are the finite volume method (FVM) and modified averaging approach (MAA). Also computation fluid dynamics (CFD) is used to solve the governing equations. An interesting approach is proposed by Hassini [22]. In this study linear approximations of the frequency and height dependent stiffness and damping coefficients were used to model a journal bearing for large displacements. Every linear approximation is valid for certain bearing height region. If the bearing leaves this region, there is switched to a new linear approximation that is valid.

This study is interested in the dynamic behavior of a single orifice compensated thrust bearing for large displacements. The solution of such problem is often referred to as the full solution in literature. 14 papers were found that modeled the full solution. In 6 cases the finite difference method was used. Three papers by Hassini [22] [23] [24] use his method. Further 2 times the FEM and one times the FVM were used. The other two methods are unknown where one is the time-transient analysis mentioned by [42]. None of the papers described above model the full solution of a single orifice compensated thrust bearing. Most full solutions were found for journal bearings.

Table A.1: Properties of found literature

Reference	Type	Shape	Governing equation	Solution method	Dynamic coefficients	Full solution
Al-Bender 2009 [9]	thrust	circular	Reynolds Equation	Small perturbation	yes	no
Bhat 2012 [28]	thrust	rectangular	Reynolds Equation	FEM	yes	no
Chandra 1983 [21]	journal	circular	Reynolds Equation	FEM	yes	no
Chen 2009 [46]	thrust	circular	Reynolds Equation	Small perturbation	yes	no
Chen 2014 [11]	HDD slider	rectangular	Linearized Boltzmann Equation	FEM	no	no
Choi 2001 [44]	journal	hemi-spherical	Reynolds Equation	FDM	no	no
Czolczynski 1993 [17]	journal	circular	Reynolds Equation	FDM	no	yes
Dal 2014 [1]	journal	circular	Reynolds Equation	FDM	no	yes
Haruyama 1989 [47]	thrust	circular	Navier-Stokes and ideal gas law	MAA	yes	no

Table A.1: (continued)

Reference	Type	Shape	governing equation	Solution method	Dynamic coefficients	Full solution
Hassini 2012 [22]	journal	circular	Reynolds Equation	Hassini-method	no	yes
Hassini 2014 [23]	journal	circular	Reynolds Equation	Hassini-method	no	yes
Hassini 2015 [24]	journal	circular	Reynolds Equation	Hassini-method	no	yes
Hua 2012 [41]	HDD slider	rectangular	Linearized Boltzmann Equation	FVM	no	yes
Lin 1988 [10]	General	N/A	Reynolds Equation	FEM	no	yes
Liu 2007 [20]	journal	circular	Equations of motion	unknown	yes	no
Mahajan 2008 [25]	squeeze film	circular	Reynolds Equation	FDM	no	yes
Majumdar 1980 [5]	thrust	circular	Reynolds Equation	Small perturbation	yes	no
Majumder 1989 [26]	journal	circular	Reynolds Equation	FDM	no	yes
Matta 2010 [32]	journal	circular	Experimental	Experiment	yes	no
Milovanova 1982 [31]	air mount	N/A	N/A	N/A	N/A	N/A
Mishra 1980 [3]	thrust	rectangular	Reynolds Equation	Small perturbation	yes	no
Ono 2009 [48]	squeeze film	rectangular	Reynolds Equation	FDM	yes	yes
Otsu 2011 [49]	journal	circular	Equation of continuity+RNM	Small perturbation	yes	no
Rao 1980 [29]	journal	circular	Reynolds Equation	Small perturbation	yes	no
Shapiro 1970 [42]	journal	circular	Reynolds Equation	Time-transient	yes	yes
Smith 1997 [45]	journal	circular	Reynolds Equation	FEM	no	yes
Stolarski 2010 [39]	squeeze film	rectangular	Reynolds Equation	FDM	no	no
Wang 2012 [7]	journal	circular	Reynolds Equation	FDM	no	yes
Wei 2011 [19]	thrust	circular	Equation of continuity	CFD	yes	no
White 1988 [16]	HDD slider	rectangular	Reynolds Equation	unkown	no	yes
Witelski 1998 [40]	HDD slider	rectangular	Reynolds Equation	Small perturbation	yes	no
Yabe 1982 [12]	thrust	circular	Reynolds Equation	Small perturbation	yes	no
Yap 1985 [50]	slider	rectangular	Reynolds Equation	FEM	no	no

Table A.1: (continued)

Reference	Type	Shape	governing equation	Solution method	Dynamic coefficients	Full solution
Yoshimoto 1999 [36]	thrust	rectangular	Equation of continuity+RNM	Small perturbation	yes	no
Yoshimoto 2001 [35]	thrust	circular	Reynolds Equation	Small perturbation	yes	no
Zhicheng 1993 [33]	thrust	circular	unkown	FRF linearization	no	no

Table A.2: Overview of found literature

Reference	Bearing type	Goal	Method	Result
Al-Bender 2009 [9]	Nominally flat, circular, centrally fed air bearing pad.	Overview of methods to model dynamic characteristics of aerostatic films (chapter 3). How to use these models for dynamic stability analysis. How to use these models for active dynamic compensation.	âĂIJStatic characteristics, load capacity, stiffness and mass flow are obtained from the Reynolds equation in the viscous flow part of the film together with the feed and entrance flow problems [2-4].âĂİ âĂIJThe time dependent flow problem has to be solved to obtain the dynamic pressure and hence the dynamic force.âĂİ Overview of possible methods to do this are given. A mathematical formulation of the linearized time-dependent Reynolds equation is given and experimentally verified. This mathematical problem is solved by converting the problem in two initial-value problems, forward integration and using superposition. The air film is modeled as a non-linear spring-damper element with a dynamic stiffness. This model is used to assess stability. The purposed models are used to design and verify an air bearing active compensation system.	The linearized time-dependent Reynolds equation shows a good agreement with the experimental data. The models purposed in this paper can be used for the design of air bearings. The purposed model based on small amplitude perturbations can be used to design an active control system to improve the dynamic stiffness characteristics. The methods purposed can easily be extended to other types of air bearings.

Table A.2: (continued)

Reference	Bearing type	Goal	Method	Result
Bhat 2012 [28]	Inherently compensated orifice based rectangular flat pad air bearings.	Analyse static and dynamic characteristics of inherently compensated orifice based flat pad air bearing systems.	Steady state characteristics are studied with the use of the Reynolds equations and the mass conservation equation for incompressible flow. Dynamic characteristics are studied using the same equations but then for compressible flow. With the dynamical model the effect on the frequency dependent stiffness and damping is investigated for varying orifice diameter, supply pressure, gap height, amount of perturbation and L/B ratio. A test setup is used to verify the theoretical load capacity and pressure distribution with experimental data.	The theoretical data coincides well with the experimental data. The dynamic characteristic noticed for varying air bearing parameters investigated in this study can be used to design stable inherently compensated air bearings under perturbation forces.
Chandra 1983 [21]	Circular journal bearings and lobed journal bearings.	Gives a dynamic analysis and solution scheme to obtain dynamic characteristics of an air bearing.	The Reynolds equation for a gas bearing are presented and FEM is used to solve pressure distribution from these equations. This is used to find the frequency dependent stiffness and damping.	FEM solution scheme.

Table A.2: (continued)

Reference	Bearing type	Goal	Method	Result
Chen 2009 [46]	Annual aerostatic bearing.	Load capacity, stiffness and damping are studied numerical.	Reynolds equation is used to numerically calculate the load capacity, stiffness and damping. Also small perturbation of the gap height is used to numerically compute FRFâĂŹs. Variation of the gas supply pressure, air-gap clearance, orifice diameter, orifice height and chamber depth is considered.	Numerical model coincides well with experimental data. It is concluded that the influence of the gas supply pressure, air-gap clearance and orifice diameter to the dynamical performance is greater than that of orifice height and chamber depth.
Chen 2014 [11]	Air bearing slider for hard disk drive	Characterization of nonlinear dynamic properties based on numerical simulation.	The linearized Boltzmann equation is used to compute the bearing force. This equation is solved with FEM. Also a probability model is added to simulate surface roughness.	It is found that system response exhibit chaos features under certain conditions.
Choi 2001 [44]	Self-acting spiral grooved hemispherical air bearing.	Studies the effects of out-of-sphericity errors on the radial stiffness of the bearing.	Steady-state Reynolds equation is used and numerically solved with the finite difference method. The linear equations were solved using TDMA (Tri-Diagonal Matrix Algorithm) and circular TDMA.	It is conclude that out-of-sphericity errors can increase the stiffness due to a decrease in the air gap clearance and a increased in pressure.
Czolczynski 1993 [17]	Gas journal bearing.	Describe transient behavior after step load of gas journal bearing and assess stability.	Reynolds equation is used to determine the pressure and is solved by rewriting to the finite difference form and applying the alternating direction implicit scheme (ADI).	Eccentricity Error plots versus time were obtained for the gas journal bearing.

Table A.2: (continued)

Reference	Bearing type	Goal	Method	Result
Dal 2014 [1]	Aerostatic journal bearing.	Studies the effect on the dynamics of the bearing with an increased clearance.	The Reynolds equation modified with a mass flow term is fully solved with the use of alternating direction implicit scheme. The computed force is substituted in the equations of motion of the bearing rotor to obtain a full solution of the shaft motions.	Increasing the number of orifices, supply pressure and orifice diameter increases the load capacity and stiffness.
Haruyama 1989 [47]	Externally pressurized, gas-lubricated, circular thrust bearing.	The dynamic performance of the air bearing is analysed with the use of a modified averaging approach.	The reduced Navier-Stokes equations, equation of continuity and ideal gas law are used to determine the dynamic stiffness and damping coefficient. The main difference is that the used Navier-Stokes equation is able to take the influence of fluid inertia forces into account (which are neglected in the Reynolds equation). A modified averaging method is used to solve the above mentioned equations. A small harmonic vibration of the air-gap clearance was assumed.	It was concluded that the conventional averaging approach gives a good approximation and that the âĂIJfirst-order solution of the perturbation method becomes inaccurate as the unsteadiness becomes highâĂİ.

Table A.2: (continued)

Reference	Bearing type	Goal	Method	Result
Hassini 2012 [22]	Gas journal bearing.	Develop a method that is faster than solving the full Reynolds equation to simulate large displacement eccentricities of a journal gas bearing.	Describes a method that uses the frequency and eccentricity dependent dynamic coefficients to solve subsequent sets of linear equations to describe large displacements. This method should be faster than solving the full Reynolds equations.	The proposed method solves the eccentricity of a gas journal bearing with enough accuracy compared with the full Reynolds solution. The simulation time with this method is halved. However, if characteristic parameters of the bearing change new dynamic coefficients have to be determined which increases the simulation time.
Hassini 2014 [23]	Gas journal bearing.	Develop a method to assess the stability of the air bearing model proposed in [22].	The poles following from a linear model obtained from the frequency and eccentricity dependent dynamic coefficients are determined. These poles are used to obtain Campbell diagrams that takes the variation of the dynamic coefficients with the excitation frequency into account.	The proposed stability assessment method is compared with the stability analysis of a full Reynols equation solution and it is concluded that the proposed method is appropriate for stability assessments.
Hassini 2015 [24]	Gas journal bearing.	Elaborate how the proposed method of previous papers can be applied to a multiple degrees of freedom system.	See comments on Hassini 2012 [22].	The proposed method can be used to model complex gas bearing systems.

Table A.2: (continued)

Reference	Bearing type	Goal	Method	Result
Hua 2012 [41]	Air bearing hard disk drive slider	Development of an implicit algorithm for the dynamic simulations based on the Finite Volume Method for air bearing sliders.	The time-dependent linearized Boltzmann equation is solved with the use of the Finite Volume Method and the Crank-Nicolson integration scheme.	The algorithm shows a good numerical accuracy, robust convergence and high speed.
Lin 1988 [10]	Air bearings in general.	Proposal of FEM to analyze the stability and dynamics of air bearings	A modified Reynolds equation is solved with the use of the Finite Element Method. How the Finite Element Method is applied is explained in some detail. Also a scheme is given to simulate a step response.	It is concluded that the proposed Finite Element Method solution can be used to analyze the dynamics and stability of various air bearings.
Liu 2007 [20]	Axial-flow hydrostatic micro gas bearing.	Investigate the impact of anisotropic in the hydrostatic stiffness on the dynamic behavior of the bearing. Further describe the physical mechanisms and describe performance and design implications.	A full mechanical analysis is made of this kind of air bearing. The hydrostatic dynamics were extracted from previous work. Also, no information is given on which numerical methods were used to solve the non-linear mechanical equations.	From the analysis it is concluded that an anisotropic hydrostatic stiffness can extend the stable operating range and the stable operation speed can be increased by a factor 5.

Table A.2: (continued)

Reference	Bearing type	Goal	Method	Result
Mahajan 2008 [25]	Circular squeeze film bearing.	Study the dynamic behavior of a squeeze film bearing.	The Reynolds equation is used to determine the pressure which is solved with the Finite Difference method. This is substituted in the equations of motion of the bearing and those are solved with the Runge-Kutta method. The equations of motion contains the force due to the pressure, gravity and asperity forces.	A dynamical model of a squeeze film air bearing is developed with asperity contacts. The experimental results do not match the theoretical model quantitatively because it is not possible to model the experimental setup perfectly. Qualitatively the results show a good agreement with the numerical results.
Majumdar 1980 [5]	Circular thrust bearing with porous restrictor.	Investigate if a circular thrust bearing with a partial porous restrictor can be used in dynamic conditions.	Combining Reynolds equation with equation of mass conservation. This last equation is used to find a relation between pressure and height to make it possible to obtain a stiffness. The Reynolds equation is linearized with the use of harmonic variations. The obtained partial differential equation is solved with the finite difference method. Finally the dynamic stiffness and damping ratio is obtained.	It is concluded that a higher supply pressure improves the static load and stiffness but decreases the damping. Stiffness and damping show a small decrease with an increase in porosity. It is concluded that the found results coincide with the results of conventional circular aerostatic thrust bearing.

Table A.2: (continued)

Reference	Bearing type	Goal	Method	Result
Majumder 1989 [26]	Porous gas journal bearing.	Study stability with non-linear transient method.	Reynolds equation together with continuity equation for porous layers is solved with the Finite Difference Method and the Successibe Over-Relaxation scheme.	Eccentricity plots were obtained for certain initial conditions.
Matta 2010 [32]	Aerodynamic journal bearing.	Design test rig to determine experimentally the static and dynamic characteristics of an journal air bearing.	Not further investigated. Not interesting for present study. Maybe in future if a test rig has to be developed.	Asynchronous stiffness and damping coefficients are identified. All modal frequencies of the test rig should be avoided. The experimental data coincides well with theory. Direct coefficients are larger than theory.
Milovanova 1982 [31]	Structural air bearing	Report about an air mount and not an air bearing. This paper is further excluded	-	-

Table A.2: (continued)

Reference	Bearing type	Goal	Method	Result
Mishra 1980 [3]	Aerostatic rectangular thrust air bearing with 4 supply holes.	To make a theoretical analysis to predict the stiffness and damping coefficients.	The Reynolds equation is used as governing equation. Linearized with small perturbation theory. With the mass conservation equation a first estimate is made of the pressure underneath the orifice restrictor. With the use of the Finite Difference Method and Successive Over-Relaxation scheme the differential equations are solved. The computed pressure is used to calculate the load capacity and this is used to determine the stiffness and damping coefficients.	Different characteristics of the stiffness and damping are given as function of the squeezenumber, dimensionless restrictor parameter , feed parameter and pressure.
Ono 2009 [48]	Rectangular squeeze film gas bearing.	Develop numerical vibration model of the linear motion guide Investigate the dynamic behaviour of the guide numerically and experimentally under impulse load Elaborate on the dynamic characteristics of squeeze film gas bearings.	Reynolds equation is used to calculate the pressure under the air bearing with the Finite Difference Method. A dynamic model of linear guide in vertical direction is made and solved with the use of the Euler method.	If the bearing clearance is decreased the impulse response of the linear guide becomes more oscillatory. The table position gradually recovers to its initial position after a large decrease in bearing clearance due to an impulse load. Dynamic stiffness is different from static and is ten times larger. The numerical model can predict well the dynamic behavior of the linear guide.

Table A.2: (continued)

Reference	Bearing type	Goal	Method	Result
Otsu 2011 [49]	Aerostatic porous journal bearings.	The dynamic characteristics of an aerostatic porous journal bearing is investigated numerically and experimentally for a porous layer of graphite and metal.	DarcyâŽs law is used to compute the mass flow through the porous layer. The pressure distribution was computed with the equation of continuity and resistance network method. These Differential Equations were solved numerically with the Finite Difference Method.	The maximum static stiffness can be obtained with this type of bearing. This type of bearing generally increases the dynamic stiffness and damping coefficients. This is seen both in numerical calculations as in experiments. The numerical method used is accurate in predicating the dynamic characteristics.
Rao 1980 [29]	Porous gas journal bearings.	Describe method to compute the dynamic stiffness and damping coefficients of externally pressurized porous gas journal bearings.	DarcyâŽs law is used to compute the mass flow through the porous layer. Reynolds equation is used to compute the pressure underneath the bearing and small perturbation method is applied to eliminate the time-dependent terms. Finite Difference Method is eventually applied to compute the pressure. Dynamic load is computed and stiffness and damping are derived from this.	Stiffness increases with squeeze number and damping decreases fast.

Table A.2: (continued)

Reference	Bearing type	Goal	Method	Result
Shapiro 1970 [42]	Gas journal hydro-dynamic bearing.	Compare the time-transient and step-jump method to test stability of gas bearings.	Time-transient: solving Reynolds equation with dynamic model with Finite Difference Method and forward integration. Step-jump: Linearization of Reynolds equation and add small perturbation to assess stability.	Time-transient method provides the most information on the bearing behaviour but is less economical while step-jump method is economical but only usable to assess stability.
Smith 1997 [45]	Shell gas journal bearing.	Study the stability of a shell gas journal bearing.	Equations of motion are derived. Reynolds equation is used to compute the pressure force component. These equations are solved numerically with FEM and Newton's Method.	Three factors limit the operation of such a bearing. Dynamic instabilities, violation of minimum clearance and component separations of the bearing.
Stolarski 2010 [39]	Rectangular squeeze film gas bearing.	Investiage the transient film pressure of this bearing.	Reynolds equation is used to model the film pressure and written in the implicit the Finite Difference Form. The equation was solved with the Newton-Raphson method and the over-relaxation technique.	The pressure solutions show a good agreement with CFD results for small amplitude vibrations. Measured pressure profiles were smaller than theoretically predicted.
Wang 2012 [7]	United gas-lubricated bearing.	Study of bifurcation and nonlinear behavior with numerical methods	Three numerical methods are used and compared. 1. Successive over relation and FDM 2. Differential transformation method and FDM 3. Small perturbation method Numerical results are used to construct power spectra, Poincare maps and bifurcation diagrams.	SOV&FDM and DTM&FDM coincide up to 4 decimal points. The purposed numerical method DTM&FDM numerical method shows a good agreement with analytic solutions.

Table A.2: (continued)

Reference	Bearing type	Goal	Method	Result
Wei 2011 [19]	Circular thrust air bearing.	Study the air flow in the air bearing lubrication film.	A combination of computational fluid dynamics and the finite volume method is applied to solve the Partial differential equations that describe the air bearing. The PDE is derived from the equation of mass, energy, state and momentum conservation.	The most interesting result is the load vs gap height curve that is obtained. This is for a static situation. No transient effects were taken in account.
White 1988 [16]	Hard disk drive slider air bearing.	Develop theoretical and computational model for dynamic air bearing simulation.	Equations of motion of slider are derived. The influence of the air bearing is modeled with the use of the Reynolds equation. A Runge-Kutta scheme is used for integrating the equations of motion. Then the Reynolds equation is solved and the slider position is recomputed.	A model is presented but not verified in any way.
Witelski 1998 [40]	Hard disk drive slider air bearing.	presented analytic solutions for the full dynamics of a one-dimensional slider bearing.	Equations of motion for the one dimensional slider bearing are derived with the use of a mechanical model and the Reynolds equation. These are linearized to study the stability of the slider bearing.	It is shown that convective influence can produce flow-induced damping and instability with a non-trivial parameter dependence. It is shown that there are many coexisting stable finite amplitude limit cycles for slider oscillations.

Table A.2: (continued)

Reference	Bearing type	Goal	Method	Result
Yabe 1982 [12]	Externally pressurized circular thrust gas bearing with surface restriction	Find expressions for the dynamic stiffness and damping coefficient for two types of bearing models.	The surface restrictor consists of radial grooves. Dividing the bearing surface in 3 parts, inlet, grooved part, flat part. Modal A uses the Reynolds equation for an equivalent recessed bearing and neglects the circumferential flow in the flat part of the bearing surface. The pressure in this region is averaged.	The experimental results were compared with the theoretical ones and showed a âĂIJcomparatively good qualitative and quantitative agreement for bearing stiffnessâĂİ and a âĂIJfairly good agreement for damping coefficientâĂİ.
Yap 1985 [50]	Rectangular gas slider bearing	Present a finite element method for the computation of pressures and load-bearing characteristics of gas-lubricated slider bearings.	Reynolds equation is solved with FEM.	No clear conclusion is given. Only numerical results.
Yoshimoto 1999 [36]	Aerostatic rectangular double-pad thrust bearing with compound restrictor.	Determine the dynamic stiffness and damping coefficient for tilt motion for this type of bearing, theoretical and experimental.	Resistance network method is used to obtain the numerical dynamic tilt characteristics. Details about this method are not given. From what can be seen it seems that it is a combination of the Reynolds equation and finite difference method results in an equation containing the pressure and bearing clearance. Further the small perturbations method is applied to obtain an expression for the dynamic tilt stiffness and damping coefficients.	Double row bearings have a higher static and dynamic tilt stiffness than single row bearings Increased groove depth reduced the damping coefficient at the optimum bearing clearance for static tilt stiffness. The squeeze effect has a major effect on the dynamic characteristics, primarily at smaller bearing gaps.

Table A.2: (continued)

Reference	Bearing type	Goal	Method	Result
Yoshimoto 2001 [35]	Aerostatic circular thrust porous thrust bearing.	Investigate the influence of two methods to supply the porous layer of air on the dynamic characteristics.	Uses the Reynolds equation and Darcyâ ĂŹs law. Finite Difference method is used to solve this and small perturbation method is used to find the dynamic characteristics.	Static stiffness increases if the supply area increases. Various characterisations of influences of design parameters on the dynamic characteristics were obtained.
Zhicheng 1993 [33]	hydrostatic circular thrust bearing.	Investigate the transient characteristics of a hydrostatic bearing subjected to a step load.	The paper makes not clear which method is used to model the lubrication film. The equations of motion of the bearing are transferred to the frequency domain in order to assess the transient behavior.	sensitive oil supply line should be as short as possible. If the initial gap height decreases the maximum displacement response decreases but the settling time becomes longer. The dynamic viscosity of oil effects the duration of the transient behavior but not the maximum displacement response. The maximum air bearing loud can be increased by using a higher supply pressure.

Appendix B

Coordinate transformation of Reynolds equation

To illustrate how the Reynolds equation for lubrication is written in cylindrical coordinates the simplified equation

$$\frac{\partial}{\partial x}\left(\frac{\partial p}{\partial x}\right) + \frac{\partial}{\partial y}\left(\frac{\partial p}{\partial y}\right) = 0 \tag{B.1}$$

is considered. The method described can also be applied to the general Reynolds equation or simplification thereof to transform that equation into cylindrical coordinates.

The following relations between the Cartesian (x, y) and cylindrical (r, ϕ) coordinates are used:

$$x = r\cos\phi,$$
$$y = r\sin\phi,$$
$$r = \sqrt{x^2 + y^2},$$
$$\phi = \arctan 2(x, y).$$

For the first derivative of p to x holds

$$\frac{\partial p}{\partial x} = \frac{\partial p}{\partial r}\frac{\partial r}{\partial x} + \frac{\partial p}{\partial \phi}\frac{\partial \phi}{\partial x} \tag{B.2}$$

with the above relations between the coordinates, the coordinate derivatives are

$$\frac{\partial r}{\partial x} = \frac{x}{\sqrt{x^2 + y^2}} = \frac{x}{r} = \cos(\phi), \tag{B.3}$$

$$\frac{\partial \phi}{\partial x} = -\frac{y}{x^2 + y^2} = -\frac{y}{r^2} = -\frac{\sin(\phi)}{r}. \tag{B.4}$$

Substitution of (B.3) and (B.4) in (B.2) this results in

$$\frac{\partial p}{\partial x} = \cos(\phi)\frac{\partial p}{\partial r} - \frac{1}{r}\sin(\phi)\frac{\partial p}{\partial \phi}. \tag{B.5}$$

The second derivative will then become

$$\frac{\partial}{\partial x}\left(\cos(\phi)\frac{\partial p}{\partial r} - \frac{1}{r}\sin(\phi)\frac{\partial p}{\partial \phi}\right) \tag{B.6}$$

$$= \cos(\phi)\frac{\partial}{\partial r}\left(\cos(\phi)\frac{\partial p}{\partial r} - \frac{1}{r}\sin(\phi)\frac{\partial p}{\partial \phi}\right) - \frac{1}{r}\sin(\phi)\frac{\partial}{\partial \phi}\left(\cos(\phi)\frac{\partial p}{\partial r} - \frac{1}{r}\sin(\phi)\frac{\partial p}{\partial \phi}\right) \tag{B.7}$$

$$= \cos(\phi)\left(\cos(\phi)\frac{\partial^2 p}{\partial r^2} + \frac{1}{r^2}\sin(\phi)\frac{\partial p}{\partial \phi} - \frac{1}{r}\sin(\phi)\frac{\partial^2 p}{\partial r \partial \phi}\right) \tag{B.8}$$

$$- \frac{1}{r}\sin(\phi)\left(-\sin(\phi)\frac{\partial p}{\partial r} + \cos(\phi)\frac{\partial^2 p}{\partial \phi \partial r} - \frac{1}{r}\cos(\phi)\frac{\partial p}{\partial \phi} - \frac{1}{r}\sin(\phi)\frac{\partial^2 p}{\partial \phi^2}\right). \tag{B.9}$$

The same process is applied to the y derivative

$$\frac{\partial p}{\partial y} = \frac{\partial p}{\partial r}\frac{\partial r}{\partial y} + \frac{\partial p}{\partial \phi}\frac{\partial \phi}{\partial y}. \tag{B.10}$$

The coordinate derivatives are

$$\frac{\partial r}{\partial y} = \frac{y}{\sqrt{x^2 + y^2}} = \frac{y}{r} = \sin(\phi), \tag{B.11}$$

$$\frac{\partial \phi}{\partial y} = \frac{x}{x^2 + y^2} = \frac{x}{r^2} = \frac{1}{r}\cos(\phi). \tag{B.12}$$

And thus

$$\frac{\partial p}{\partial y} = \sin(\phi)\frac{\partial p}{\partial r} + \frac{1}{r}\cos(\phi)\frac{\partial p}{\partial \phi}. \tag{B.13}$$

The second derivative then becomes

$$\frac{\partial^2 p}{\partial y^2} = \frac{\partial}{\partial y}\left(\sin(\phi)\frac{\partial p}{\partial r} + \frac{1}{r}\cos(\phi)\frac{\partial p}{\partial \phi}\right) \tag{B.14}$$

$$= \sin(\phi)\frac{\partial}{\partial r}\left(\sin(\phi)\frac{\partial p}{\partial r} + \frac{1}{r}\cos(\phi)\frac{\partial p}{\partial \phi}\right) + \frac{1}{r}\cos(\phi)\frac{\partial}{\partial \phi}\left(\sin(\phi)\frac{\partial p}{\partial r} + \frac{1}{r}\cos(\phi)\frac{\partial p}{\partial \phi}\right) \tag{B.15}$$

$$= \sin(\phi)\left(\sin(\phi)\frac{\partial^2 p}{\partial r^2} - \frac{1}{r^2}\cos(\phi)\frac{\partial p}{\partial \phi} + \frac{1}{r}\cos(\phi)\frac{\partial^2 p}{\partial r \partial \phi}\right) \tag{B.16}$$

$$+ \frac{1}{r}\cos(\phi)\left(\cos(\phi)\frac{\partial p}{\partial r} + \sin(\phi)\frac{\partial^2 p}{\partial \phi \partial r} - \frac{1}{r}\sin(\phi)\frac{\partial p}{\partial \phi} + \frac{1}{r}\cos(\phi)\frac{\partial^2 p}{\partial \phi^2}\right). \tag{B.17}$$

Substituting both second derivatives in (B.1) results in

$$\frac{\partial^2 p}{\partial x^2} + \frac{\partial^2 p}{\partial y^2} = \frac{\partial^2 p}{\partial r^2} + \frac{1}{r}\frac{\partial p}{\partial r} + \frac{1}{r^2}\frac{\partial^2 p}{\partial \phi^2}. \tag{B.18}$$

If it is assumed that p is constant in ϕ, hence if an axial symmetric fluid bearing is considered, (B.18) reduces to

$$\frac{\partial^2 p}{\partial x^2} + \frac{\partial^2 p}{\partial y^2} = \frac{\partial^2 p}{\partial r^2} + \frac{1}{r}\frac{\partial p}{\partial r} = 0. \tag{B.19}$$

This can be rewritten as:

$$\frac{r}{r}\frac{\partial^2 p}{\partial r^2} + \frac{1}{r}\frac{\partial r}{\partial r}\frac{\partial p}{\partial r} = \frac{1}{r}\frac{d}{dr}\left(r\frac{dp}{dr}\right) = 0. \tag{B.20}$$

The Reynolds equation in for an axial symmetric fluid bearing is thus

$$\frac{1}{r}\frac{d}{dr}\left(r\frac{dp}{dr}\right) = 0. \tag{B.21}$$

Appendix C

Additional modeling results

C.1 Incompressible fluids without orifice restriction

Figure C.1 shows the height $h(t)$ for the numeric and analytic solution for a initial height $h_0 = 50 \cdot 10^{-6}$ m and an external force of $F_{ex} = 300$ N. It is seen that the height decreases much faster compared with the same simulation for $F_{ex} = 68.67$ N as figure 4.5 shows. Figure C.2 shows the according pressure distribution. As can be seen, the pressure first increases to above the supply pressure before it drops to the ambient pressure at the outer boundary. The fluid is in this situation squeezed out of the air bearing gap and streams even back into the supply line.
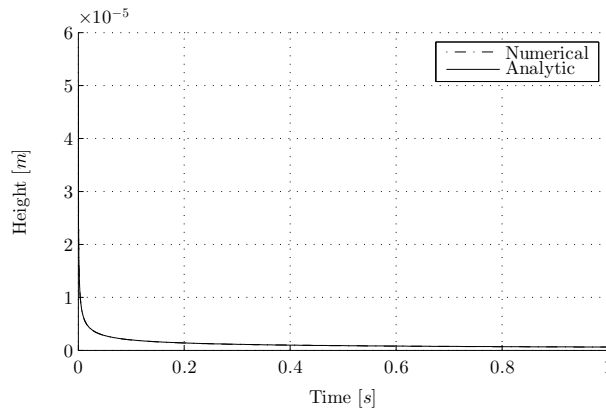
Figure C.1: Numeric solution of $h(t)$ for $h_0 = 50 \cdot 10^{-6}$ m, $F_{ex} = 300$ N, $I = 1000$, $J = 1000$.
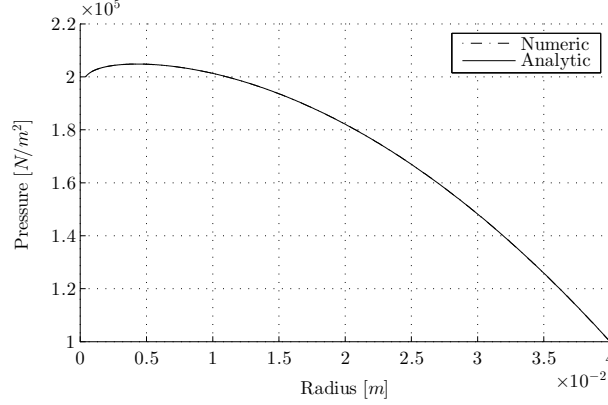
Figure C.2: Numeric solution of $p(r)$ for $h_0 = 50 \cdot 10^{-6}\ m$, $F_{ex} = 300\ N$, $I = 1000$.

C.2 Compressible fluids

Figure C.3 shows the gap height response for the compressible and incompressible model for an external force 20 N larger than the static load capacity. In Figure 4.17 it can be seen that the static pressure distributions is not equal for the compressible and incompressible case. Hence, the static load capacity is also different. The load capacity for the incompressible and compressible case, for bearing under consideration is 55 N and 72 N, respectively. This means that in figure C.3 the external force is respectively 75 N and 92 N for the incompressible and compressible case. This 20 N step was applied gradually over $1 \cdot 10^{-6}\ s$ as can be seen in figure C.4. In figure C.3 it can be seen that the height decrease between the two models coincide well. However, if the gap height response is observed during the application of the step force a relative large difference between the compressible and incompressible case is seen. This is shown by figure C.5. The initial rapid decrease in height for the compressible case is caused by compressibility of the fluid.

This can also be seen in the discretized Reynolds equation used and repeated here as

$$\nabla \cdot \left(\frac{\rho h^3}{12\mu} \nabla p \right) = \frac{p_{j+1} h_{j+1} - p_j h_j}{\Delta t} \tag{C.1}$$

where j denotes the current time instant. The pressure p is directly coupled to the external applied force due to the force balance. This means that the pressure increases directly if the force is increased. The left hand side is the divergence of the mass flow which can be assumed finite. If Δt is small enough and the pressure makes a relative large step this means that the height also has to make a step in order to let (C.1) hold. Physically, this means that due to the step in the force the pressure increases and therefore also the density due to the compressibility. Because the fluid is not flowing yet directly after the impulse, the mass of the fluid underneath the bearing is preserved and the density can only increase by a decrease of the volume and thus a rapid decrease of the height. After the compression the fluid starts to flow out of the bearing gap and the height decreases at a less fast rate.

If the incompressible Reynolds equation is considered, repeated here as

$$\nabla \cdot \left(\frac{h^3}{12\mu} \nabla p \right) = \frac{h_{j+1} - h_j}{\Delta t}, \tag{C.2}$$

then can be seen that the height is not linked to the pressure and a more steady height decrease will be seen after a step in the pressure.
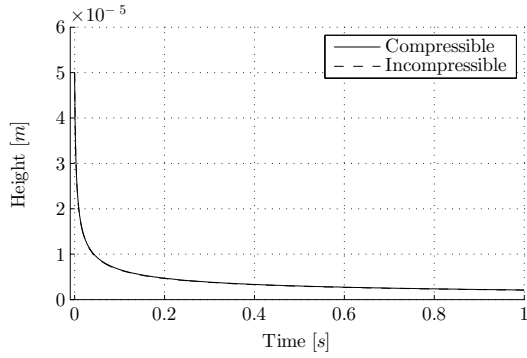
Figure C.3: Gap height response from $h_0 = 50 \cdot 10^{-6}$ m for compressible and incompressible case.
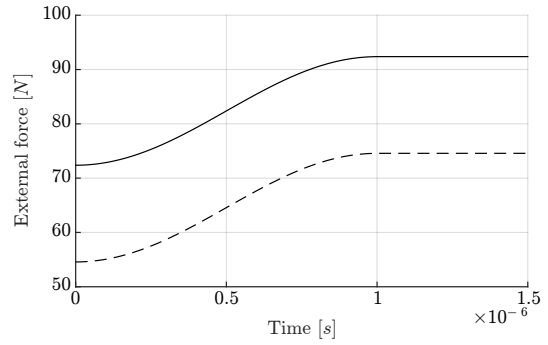
Figure C.4: Step force input $F_{ex} = 75$ N
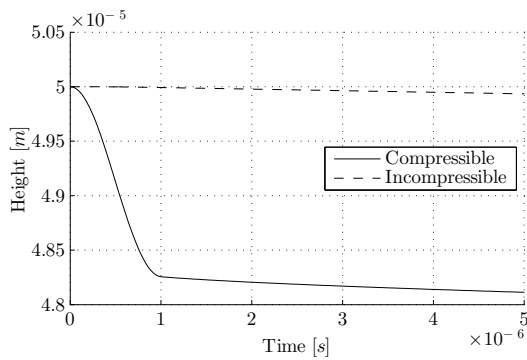
Figure C.5: Gap height response from $h_0 = 50 \cdot 10^{-6}$ m for compressible and incompressible case until $t = 5 \cdot 10^{-6}$ s.

C.3 Compressible fluids with orifice restrictor

In section 4.3 several equations to describe the mass flows in the air bearing are given. These are combined with the Reynolds equation and solved with Newton's method. To apply Newton's method the derivative of these equations has also to be known. These derivatives are given below. The partial derivatives with respect to $\frac{\partial \dot{m}}{\partial p_e}$ and $\frac{\partial \dot{m}}{\partial p_b}$ of (4.109) are computed as follows. First

$$A = \frac{2\kappa}{\kappa - 1} \left(\left(\frac{p_e}{p_b} \right)^{\frac{2}{\kappa}} - \left(\frac{p_e}{p_b} \right)^{\frac{\kappa+1}{\kappa}} \right) \tag{C.3}$$

is defined to shorten notation. The derivative of A with respect to p_e is

$$\frac{\partial A}{\partial p_e} = \frac{2\kappa}{\kappa - 1} \left(\frac{2}{\kappa p_b} \left(\frac{p_e}{p_b} \right)^{\frac{2-\kappa}{\kappa}} - \frac{\kappa + 1}{\kappa p_b} \left(\frac{p_e}{p_b} \right)^{\frac{1}{\kappa}} \right). \tag{C.4}$$

The derivative of A with respect to p_b is

$$\begin{aligned}
\frac{\partial A}{\partial p_b} &= \frac{\partial}{\partial p_b} \left(\frac{2\kappa}{\kappa - 1} \left(\left(\frac{p_b}{p_e} \right)^{-\frac{2}{\kappa}} - \left(\frac{p_b}{p_e} \right)^{-\frac{\kappa+1}{\kappa}} \right) \right) \\
&= \frac{2\kappa}{\kappa - 1} \left(-\frac{2}{\kappa p_e} \left(\frac{p_b}{p_e} \right)^{-\frac{2+\kappa}{\kappa}} + \frac{\kappa + 1}{\kappa p_e} \left(\frac{p_b}{p_e} \right)^{-\frac{2\kappa+1}{\kappa}} \right)
\end{aligned} \tag{C.5}$$

If $\left(\frac{2}{\kappa+1} \right)^{\frac{\kappa}{\kappa-1}} \leq \frac{p_e}{p_b} \leq 1$, then

$$\frac{\partial \dot{m}}{\partial p_e} = \frac{C_d A_{eff} p_b}{\sqrt{R_s T}} \frac{1}{2\sqrt{A}} \frac{\partial A}{\partial p_e} \tag{C.6}$$

and

$$\frac{\partial \dot{m}}{\partial p_b} = \frac{C_d A_{eff}}{\sqrt{R_s T}} \sqrt{A} + \frac{C_d A_{eff}}{\sqrt{R_s T}} p_b \frac{1}{2\sqrt{A}} \frac{\partial A}{\partial p_b}. \tag{C.7}$$

The same can be done for negative mass flows. Let

$$B = \frac{2\kappa}{\kappa - 1} \left(\left(\frac{p_b}{p_e} \right)^{\frac{2}{\kappa}} - \left(\frac{p_b}{p_e} \right)^{\frac{\kappa+1}{\kappa}} \right) \tag{C.8}$$

then

$$\begin{aligned}
\frac{\partial B}{\partial p_e} &= \frac{\partial}{\partial p_e} \left(\frac{2\kappa}{\kappa - 1} \left(\left(\frac{p_e}{p_b} \right)^{-\frac{2}{\kappa}} - \left(\frac{p_e}{p_b} \right)^{-\frac{\kappa+1}{\kappa}} \right) \right) \\
&= \frac{2\kappa}{\kappa - 1} \left(-\frac{2}{\kappa p_b} \left(\frac{p_e}{p_b} \right)^{-\frac{2+\kappa}{\kappa}} + \frac{\kappa + 1}{\kappa p_b} \left(\frac{p_e}{p_b} \right)^{-\frac{2\kappa+1}{\kappa}} \right)
\end{aligned} \tag{C.9}$$

and

$$\frac{\partial B}{\partial p_b} = \frac{2\kappa}{\kappa - 1} \left(\frac{2}{\kappa p_e} \left(\frac{p_b}{p_e} \right)^{\frac{2-\kappa}{\kappa}} - \frac{\kappa + 1}{\kappa p_e} \left(\frac{p_b}{p_e} \right)^{\frac{1}{\kappa}} \right). \tag{C.10}$$

If $1 < \frac{p_e}{p_b} \leq \left(\frac{2}{\kappa+1} \right)^{-\frac{\kappa}{\kappa-1}}$, then

$$\frac{\partial \dot{m}}{\partial p_e} = -\frac{C_d A_{eff}}{\sqrt{R_s T}} \sqrt{B} - \frac{A_{eff}}{\sqrt{R_s T}} p_e \frac{1}{2\sqrt{B}} \frac{\partial B}{\partial p_e} \tag{C.11}$$

and

$$\frac{\partial \dot{m}}{\partial p_b} = -\frac{C_d A_{eff}}{\sqrt{R_s T}} p_e \frac{1}{2\sqrt{B}} \frac{\partial B}{\partial p_b}. \tag{C.12}$$

This results in the following piecewise derivatives

$$\frac{\partial \dot{m}(p_b, p_e)}{\partial p_e} = \begin{cases} 0 & \text{if } \frac{p_e}{p_b} < \left(\frac{2}{\kappa+1}\right)^{\frac{\kappa}{\kappa-1}} \\ \frac{C_d A_{eff} p_b}{\sqrt{R_s T}} \frac{1}{2\sqrt{A}} \frac{\partial A}{\partial p_e} & \text{if } \left(\frac{2}{\kappa+1}\right)^{\frac{\kappa}{\kappa-1}} \le \frac{p_e}{p_b} \le 1 \\ -\frac{C_d A_{eff}}{\sqrt{R_s T}} \sqrt{B} - \frac{C_d A_{eff}}{\sqrt{R_s T}} p_e \frac{1}{2\sqrt{B}} \frac{\partial B}{\partial p_e} & \text{if } 1 < \frac{p_e}{p_b} \le \left(\frac{2}{\kappa+1}\right)^{-\frac{\kappa}{\kappa-1}} \\ -\left(\frac{2\kappa}{\kappa+1}\right)^{\frac{1}{2}} \left(\frac{2}{\kappa+1}\right)^{\frac{1}{\kappa-1}} & \text{if } \frac{p_e}{p_b} > \left(\frac{2}{\kappa+1}\right)^{-\frac{\kappa}{\kappa-1}} \end{cases} \tag{C.13}$$

$$\frac{\partial \dot{m}(p_b, p_e)}{\partial p_b} = \begin{cases} \left(\frac{2\kappa}{\kappa+1}\right)^{\frac{1}{2}} \left(\frac{2}{\kappa+1}\right)^{\frac{1}{\kappa-1}} & \text{if } \frac{p_e}{p_b} < \left(\frac{2}{\kappa+1}\right)^{\frac{\kappa}{\kappa-1}} \\ \frac{C_d A_{eff}}{\sqrt{R_s T}} \sqrt{A} + \frac{C_d A_{eff}}{\sqrt{R_s T}} p_b \frac{1}{2\sqrt{A}} \frac{\partial A}{\partial p_b} & \text{if } \left(\frac{2}{\kappa+1}\right)^{\frac{\kappa}{\kappa-1}} \le \frac{p_e}{p_b} \le 1 \\ -\frac{C_d A_{eff}}{\sqrt{R_s T}} p_e \frac{1}{2\sqrt{B}} \frac{\partial B}{\partial p_b} & \text{if } 1 < \frac{p_e}{p_b} \le \left(\frac{2}{\kappa+1}\right)^{-\frac{\kappa}{\kappa-1}} \\ 0 & \text{if } \frac{p_e}{p_b} > \left(\frac{2}{\kappa+1}\right)^{-\frac{\kappa}{\kappa-1}} \end{cases} \tag{C.14}$$

The derivatives of (4.118) with respect to $p_{0,j}$ and $p_{1,j}$ are

$$\frac{\partial \dot{m}_{gap}}{\partial p_0} = \frac{\pi h^3 R_1}{6\eta R_s T(r_1 - r_0)} p_0 \tag{C.15}$$

and

$$\frac{\partial \dot{m}_{gap}}{\partial p_1} = -\frac{\pi h^3 R_1}{6\eta R_s T(r_1 - r_0)} p_1. \tag{C.16}$$

The derivatives needed for Newton's method of (4.128) and (4.129) are derived as follows. Equation (4.128) is also a function of p_{th}. This parameter can be eliminated by substituting (4.122) in (4.128) with K according to (4.123) and Re as defined in 4.124 with $\dot{m}_{in} = \dot{m}_{gap}$ The jacobian of the set of equations (4.128) and (4.129) is equal to

$$\underline{J}_o(p_{in}, p_o) = \begin{bmatrix} \frac{\partial f_1}{\partial p_o} & \frac{\partial f_1}{\partial p_{in}} & \frac{\partial f_1}{\partial p_{in+1}} \\ \frac{\partial f_2}{\partial p_o} & \frac{\partial f_2}{\partial p_{in}} & \frac{\partial f_2}{\partial p_{in+1}} \end{bmatrix} \tag{C.17}$$

Herein

$$\frac{\partial f_1}{\partial p_o} = -\frac{\partial \dot{m}_{in}(p_o, p_{th}(p_o, p_{in}))}{\partial p_o} = -\frac{\partial \dot{m}_{in}}{\partial p_o} - \frac{\partial \dot{m}_{in}}{\partial p_{th}} \frac{\partial p_{th}}{\partial p_o} \tag{C.18}$$

with

$$p_{th} = p_o - \frac{(p_o - p_{in})}{K(p_{in})} \tag{C.19}$$

and

$$\frac{\partial p_{th}}{\partial p_o} = 1 - K^{-1}. \tag{C.20}$$

$$\frac{\partial f_1}{\partial p_{in}} = \frac{\dot{m}_{gap}(p_{in})}{\partial p_{in}} - \frac{\partial \dot{m}_{in}}{\partial p_{th}} \frac{\partial p_{th}}{\partial p_{in}} \tag{C.21}$$

where

$$\frac{\partial p_{th}}{\partial p_{in}} = K^{-1} + \frac{(p_o - p_{in})}{K^2} \frac{\partial K(\dot{m}_{gap}(p_{in}, p_{ib+1}))}{\partial p_{in}} \tag{C.22}$$

$$= K^{-1} + \frac{(p_o - p_{in})}{K^2} \frac{\partial K(\dot{m}_{gap})}{\partial \dot{m}_{gap}} \frac{\partial \dot{m}_{gap}}{\partial p_{in}} \tag{C.23}$$

---

with

$$\frac{\partial K}{\partial \dot{m}_{gap}} = \frac{\partial}{\partial \dot{m}_{gap}} \left(0.2 + 0.5 \left(1 - e^{-\frac{\dot{m}_{gap}}{1200\pi R_1 \eta}} \right)^2 \right)$$
$$= \left(\left(1 - e^{-\frac{\dot{m}_{gap}}{1200\pi R_1 \eta}} \right) \frac{\partial}{\partial \dot{m}_{gap}} \left(1 - e^{-\frac{\dot{m}_{gap}}{1200\pi R_1 \eta}} \right) \right) \tag{C.24}$$
$$= \left(\left(1 - e^{-\frac{\dot{m}_{gap}}{1200\pi R_1 \eta}} \right) \left(-e^{-\frac{\dot{m}_{gap}}{1200\pi R_1 \eta}} \left(-\frac{1}{1200\pi R_1 \eta} \right) \right) \right).$$

$$\frac{\partial f_2}{\partial p_o} = -\frac{\partial \dot{m}_o}{\partial p_o}. \tag{C.25}$$

$$\frac{\partial f_2}{\partial p_{in}} = \frac{\partial \dot{m}_{gap}}{\partial p_{in}}. \tag{C.26}$$

If these equations are combined with the finite difference form of the Reynolds equation also the derivative with respect to p_{in+1} has to be calculated. The derivative of f_1 with respect to p_{in+1} is

$$\frac{\partial f_1}{\partial p_{in+1}} = \frac{\partial \dot{m}_{gap}}{\partial p_{in+1}} - \frac{\partial \dot{m}_{in}}{\partial p_{th}} \frac{\partial p_{th}}{\partial p_{in+1}}, \tag{C.27}$$

where

$$\frac{\partial p_{th}}{\partial p_{in+1}} = \frac{(p_o - p_{in})}{K^2} \frac{\partial K(\dot{m}_{gap})}{\partial \dot{m}_{gap}} \frac{\partial \dot{m}_{gap}}{\partial p_{in+1}} \tag{C.28}$$

and for f_2 this is

$$\frac{\partial f_2}{\partial p_{in+1}} = \frac{\partial \dot{m}_{gap}}{\partial p_{in+1}}. \tag{C.29}$$

Note that for $\frac{\partial \dot{m}_{in}}{\partial p_o}$, $\frac{\partial \dot{m}_{in}}{\partial p_{th}}$, $\frac{\partial \dot{m}_{gap}}{\partial p_{in}}$, $\frac{\partial \dot{m}_o}{\partial p_o}$ and $\frac{\partial \dot{m}_o}{\partial p_{in}}$, (C.13) and (C.14) can be used.

C.4   Full air bearing model

In this section, some additional simulation results are shown that were obtained with the full air bearing model.

Figure C.6 shows the gap height response for the air bearing subjected to a temporary increased force. The force on the air bearing is initially $F_s = Mg = 49.05\ N$ due to gravity. At $t = 0\ s$ the force is increased to $F_s = 150\ N$ and decreased again at $t = 0.025\ s$ to $F_s = 49.05\ N$. As can be seen, the gap height decreases from the initial static height until the increased force is reduced again. After that, the height is recovering to the initial position. The non-linear character of this model is clearly visible in the response. The shape of the decreasing trajectory is different from the increasing trajectory. This indicates that the superposition property does not hold. Further, it is clearly seen that the 'eigenfrequency' changes if the gap height changes.

Figure C.7 shows several frequency sine-sweep results for different amplitudes and increasing and decreasing frequencies. The air bearing model was statically loaded by a gravitational force of $Mg = 49.05\ N$ and additionally subjected to a static external sinusoidal force with am amplitude of $A\ N$ and a frequency between $10\ Hz$ and $1000\ Hz$. Each simulation was started with the sinusoidal force frequency at $10\ Hz$ or $1000\ Hz$. Initially, there was simulated long enough until the steady-state amplitude was reached. Then, the steady-state height amplitude was registered and the frequency was increased or decreased in the same simulation. This was repeated until the maximum or minimum frequency was reached. The frequency step changes for low frequencies were smaller than for large frequencies because it was expected that the height amplitude response changed more for low frequencies. The steady-state amplitude was defined as $\frac{x_{max}(t) - x_{min}(t)}{2}$ where x only consists of the one steady-state period. As can be seen the shape of the amplitude-frequency response changes if the sinusoidal force increases. In the case of $A = 25\ N$ even a small resonance peak occurs.
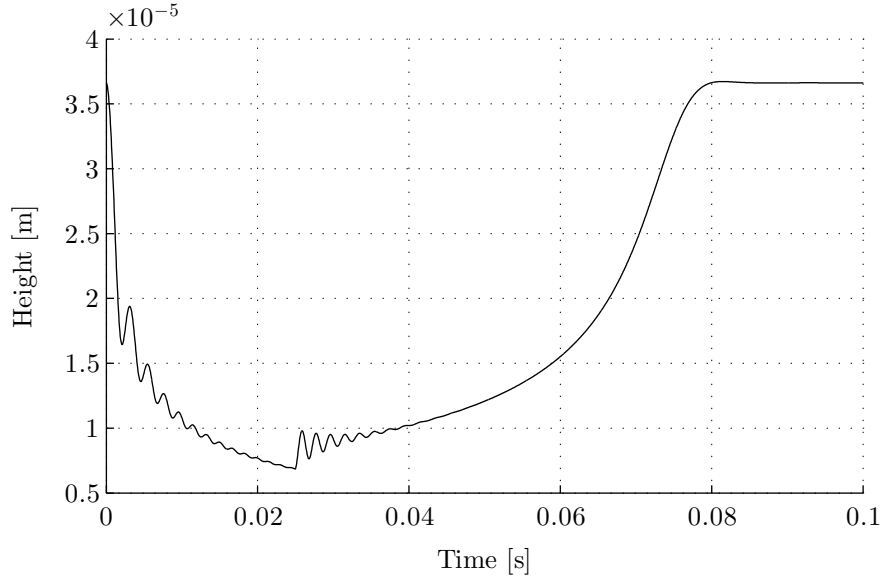
Figure C.6: Gap height response of bearing subjected to temporary increased force with amplitude of 150 N and a duration of 0.025 s for an air bearing with mass $M = 5$ kg.
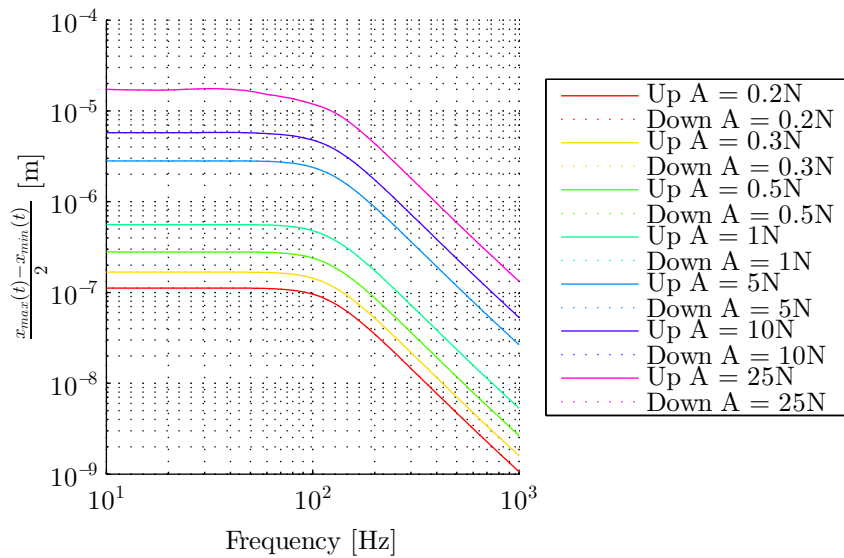

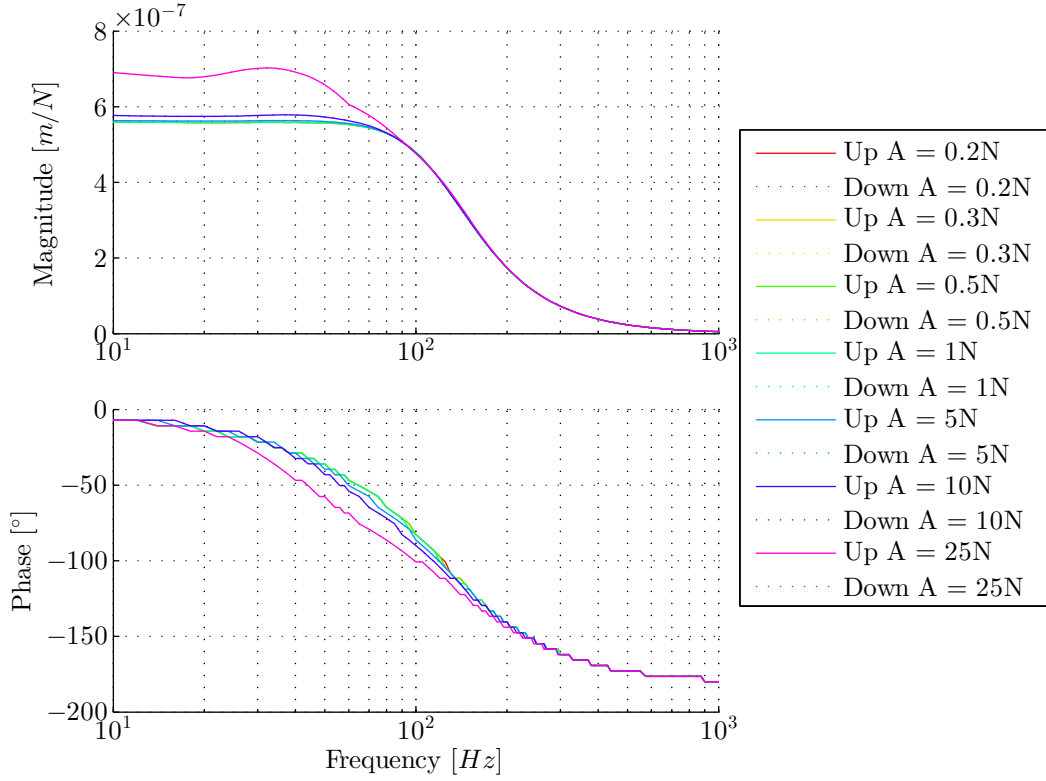Figure C.7: Frequency sine-sweep results for $M = 5$ kg ($h_0 = 36.6$ μm).

Figure C.8: Frequency response bode diagram derived from sine-sweep results for $M = 5$ kg ($h_0 = 36.6$ μm).

If linear theory is applied and it is assumed that the steady-state height response consist only of a sinusoid with amplitude $\frac{x_{max}(t) - x_{min}(t)}{2}$ and inputted excitation frequency, a frequency response bode diagram can be derived. Figure C.8 shows this bode diagram where the magnitude is $\frac{x_{max}(t) - x_{min}(t)}{2A}$ and the phase is the phase difference between the sinusoidal input frequency and the corresponding sinusoidal output.

As can be seen, the magnitude and phase remain constant for small amplitudes up to 0.3 N. For large amplitudes the magnitude starts to gradually change and for the extreme case of 25 N even a resonance peaks occurs. The phase seems to decrease with an increase in the magnitude. This indicates that the system response becomes more delayed compared to the input for large input amplitudes. The effects seen in the amplitude-frequency response is indicates that the system behaves non-linear for large displacements, as expected.

Appendix D

Additional experimental results

In this appendix a more elaborated description of the experimental setup is given. Further, a broader description on the frequency response results is given.

D.1 Experimental setup

Figure 5.2 shows the used experimental setup schematically. The setup consist of a T-sloted base table where on top a large steel block is mounted. On the steel block a Kistler 9061A force transducer is placed with on top of the force transducer the bearing mount plate (see table D.1 for specifications). The air bearing pad to be investigated is mounted with four bolts on the bearing mount plate. The bearing pad is depicted in figure D.1. On the bearing pad a bearing counter surface is placed (see figure D.2). One side of the counter surface block is flat to make the creation of an air lubrication film possible between the counter surface and the bearing pad. The other side of the bearing pad has a large radius. On top of this radius a concave bearing pad is placed which is rigidly fixed to a linear guide. The concave bearing pad creates an air lubrication film between the guide and the counter surface and acts like an air lubricated pivot. The supply lubrication holes of the pivot bearing pad are visible in figure D.3. The pivot corrects for tilt errors and ensures a parallel gap between the air bearing pad and the flat counter surface. The linear guide is air lubricated and contains a piston pressure chamber. The pressure in this chamber can be increased to apply an extra load via a piston on the air bearing pad. Figures D.4 and D.5 show the linear guide and the piston pressure chamber respectively. A total picture of the experimental setup is shown in figure D.6.

Two Lion C7-C capacitive displacement sensors are placed with fixtures above the bearing counter surface as shown in figure **??** to measure the air bearing gap height (see table D.2) for specifications). The fixtures are mounted with magnets on the large steel block. Further, a Alicat Scientific M-10SLPM-D mass flow meter (table D.3) and a Fluke 700PD7 (table D.4) pressure module are used to measure the fluid mass flow and pressure. For modal hammer experiments an Endevco model 2302-100 modal hammer (table D.5) is used.

Figure 5.3 shows a one-dimensional dynamical model of the test setup. In this model it is assumed that the steel block can be seen as the rigid world. The load cell has a stiffness which is used to measure the force between the rigid world and the bearing mount plate but this stiffness is $1.4 \cdot 10^{10} [N/m]$ and therefore the load cell link is seen as a rigid connection. M_{cs} represents the counter surface mass and is equal to 0.55 kg. This mass is linked via the air bearing lubrication layer to the rigid world. M_g is the mass of the linear guide and is linked by the pivot lubrication layer to the counter surface. M_g is equal to 0.55 kg. The mass of the counter surface M_{cs} and of the guide M_g are used to preload the bearing and give the bearing a nominal gap height for a certain supply pressure. The mass of the guide can be increased, or the piston pressure chamber can be pressurized to adjust the nominal gap height.
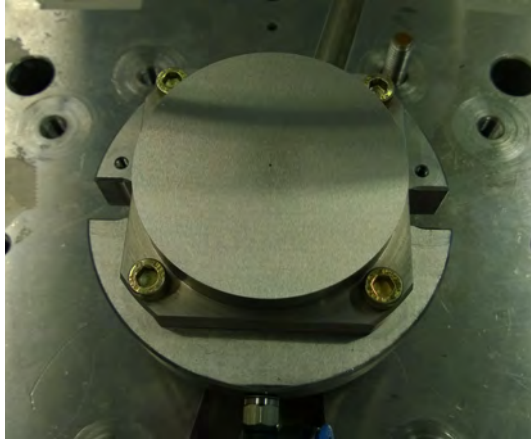
Figure D.1: Bearing pad mounted on mountingplate
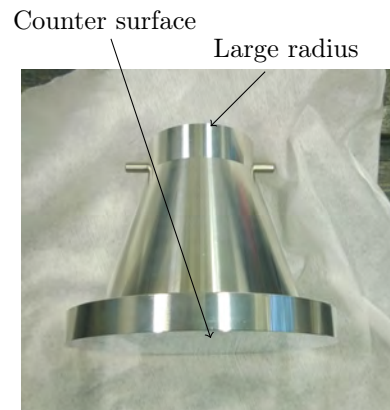
Figure D.2: Bearing counter surface.
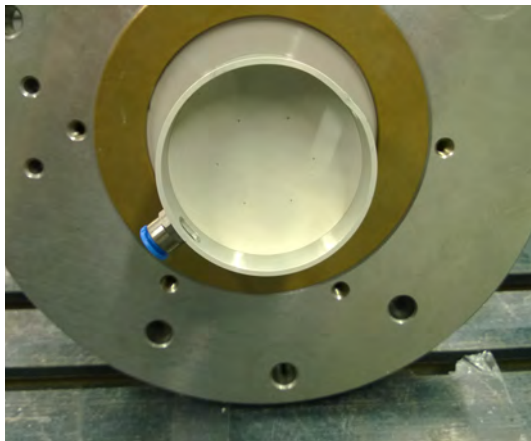
Figure D.3: Concave pivot bearing pad.

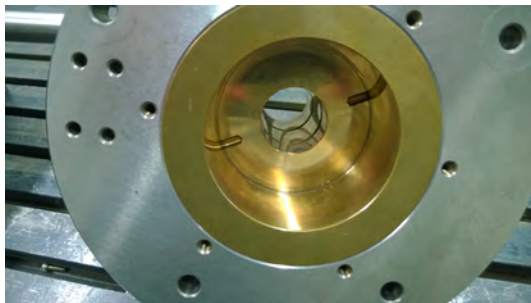Figure D.4: Linear guide with pivot bearing pad.

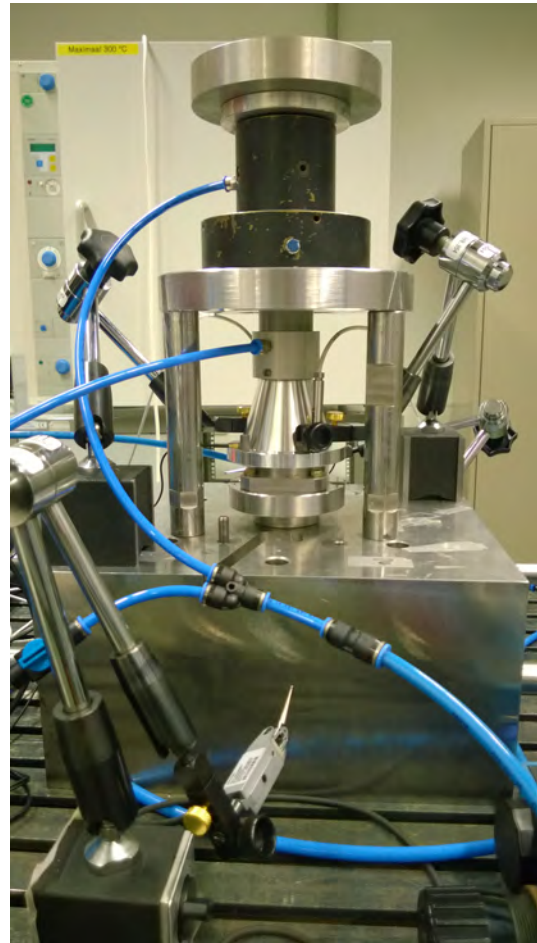Figure D.5: Inside of linear guide support.

Figure D.6: Picture of test setup.

Table D.1: Manufacture data of Kistler 9061A force transducer.

Property	Value	Unit
Range	0-200	kN
Calibrated partial range	0-20	kN
Overload	240	kN
Max. Bending moment	$\leq \pm 830$	Nm
Rigidity	≈ 14	$kN/\mu m$
Capacity	≈ 148	pF
Weight	160	g
Sensitivity	≈ -4.3	pC/N
Threshold	≤ 0.01	N
Operating temperature range	-196-200	$^{\circ}C$
Linearity	$\leq \pm 1$	% FSO
Hysteresis	< 0.5	% FSO
Insulation resistance	≥ 10	$T\Omega$
Temperature coefficient	-0.02	$\%/^{\circ}C$

Table D.2: Manufacture data of Lion C7-C capacitive displacement sensor.

Property	Value	Unit
Range	75-125	μm
Resolution	3.5	nm RMS
Sensor diameter	1.7	mm
Maximum error	0.5	% F.S.
Bandwidth	20	kHz

Table D.3: Manufacture data of Alicat Scientific M-10SLPM-D mass flow meter.

Property	Value	Unit
Accuracy	$\pm$ (0.8% of Reading + 0.2% of Full Scale)	
Repeatability	$\pm$ 0.2	% F.S.
Operating Range	1 to 100	% F.S.
Operating Temperature	-10 to +50	$^{\circ}C$
Zero shift	0.02	% F.S. / $^{\circ}C$ / Atm.
Span shift	0.02	& F.S. / $^{\circ}C$ / Atm.
Humidity Range	0 - 100	%
Measurable Flow Rate	128	% F.S.
Maximum Pressure	145	PSIG

Table D.4: Manufacture data of Fluke 700PD7 pressure module.

Property	Value	Unit
Range	1 - 14	Bar
Total Uncertainty	0.07	% F.S.
Temperature range	0-50	$^{\circ}C$

Table D.5: Manufacture data of modal hammer 2302-100.

Property	Value	Unit
Range	220	N
Sensitivity	22.7	mV/N
Maximum force	4448	N
Resonance frequency	50	kHz
Frequency range	8	kHz
Head mass	100	$grams$
Head diameter	19	mm
Impact tip diameter	6.4	mm
DC output bias	9-10	Vdc
Output impedance	<100	$Ohms$
Full scale output	±5	V
Supply voltage	18-24	Vdc
Supply current	2-10	mA
Temperature range	-55 - 125	$^\circ C$

D.2 Airbearing surface roughness measurement

Figures D.8 till D.15 shows the measured roughness in 8 different directions. Figure D.7 shows schematically these directions on the air bearing surface. The mean of each measurement is located at height zero. The large spike and standard deviation in figure D.12 is due to the measurement over the air bearing inlet hole.
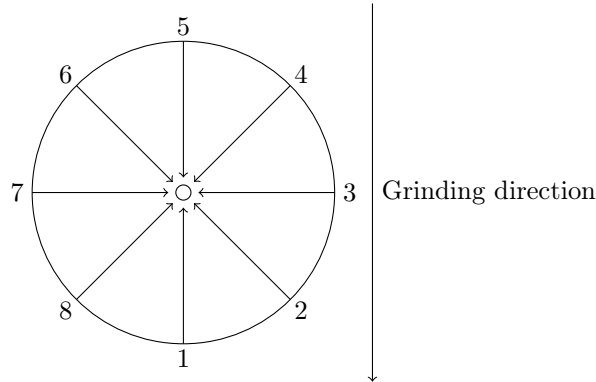
Figure D.7: Air bearing surface with grinding direction.
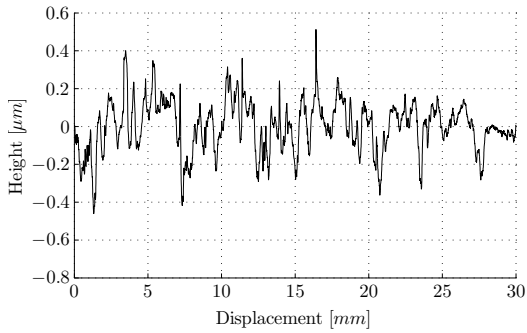
Figure D.8: Surface roughness measurement in direction 1 with standard deviation of $\sigma = 0.32 \ \mu m^2$.
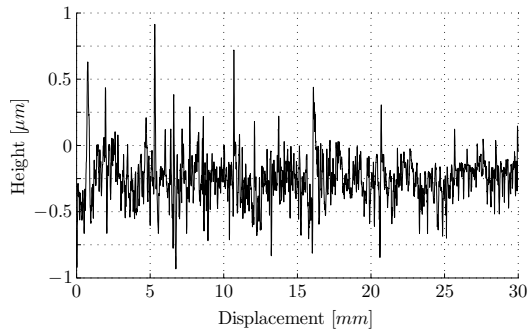
Figure D.9: Surface roughness measurement in direction 2 with standard deviation of $\sigma = 0.32 \ \mu m^2$.
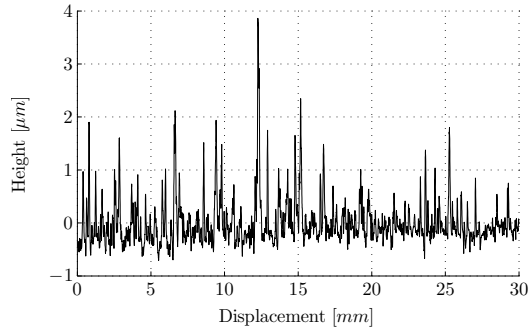
Figure D.10: Surface roughness measurement in direction 3 with standard deviation of $\sigma = 0.54 \ \mu m^2$.
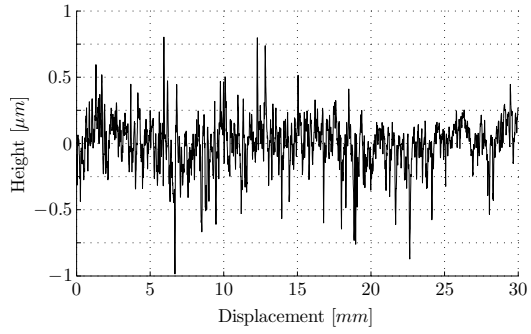
Figure D.11: Surface roughness measurement in direction 4 with standard deviation of $\sigma = 0.33 \ \mu m^2$.
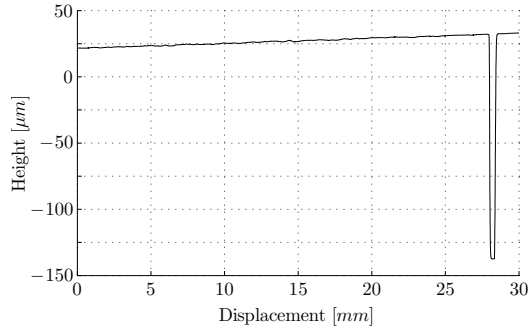
Figure D.12: Surface roughness measurement in direction 5 with standard deviation of $\sigma = 2 \ \mu m^2$.
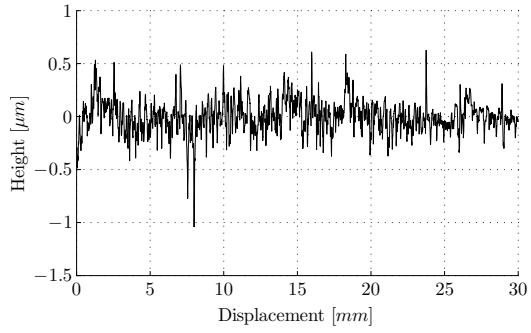
Figure D.13: Surface roughness measurement in direction 6 with standard deviation of $\sigma = 0.34 \ \mu m^2$.
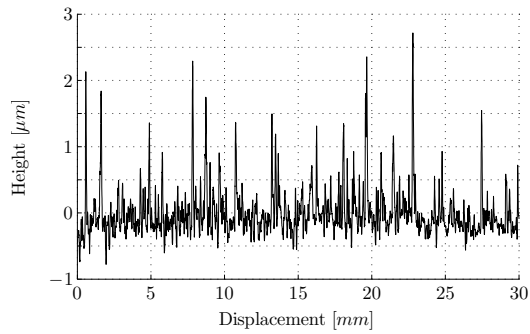
Figure D.14: Surface roughness measurement in direction 7 with standard deviation of $\sigma = 0.49 \ \mu m^2$.
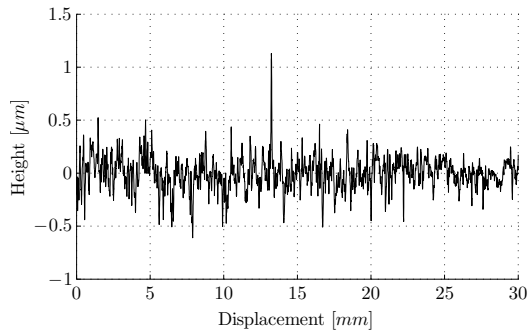
Figure D.15: Surface roughness measurement in direction 8 with standard deviation of $\sigma = 0.33 \ \mu m^2$.

D.3 Frequency response measurements

To investigate the gap height response to an input force in the frequency domain a modal hammer analysis was performed. The air bearing was excited by hitting the levitated mass with a model hammer, that has a force transducer mounted on the tip. This way, a time response from the force is obtained. The displacement sensors were used to simultaneously obtain a time response for the gap height. The sampling frequency was set to $102400\ Hz$ and the Nyquist frequency is thus $51200\ Hz$. Each excitation of the levitating mass with the modal hammer is seen as one measurement sample and 20 samples were taken. Each sample had a duration of $T = 0.64s$ resulting in a frequency resolution of $1/0.64 = 1.5625Hz$. The impulse was applied at $0.064\ s$ of the sample. This prevents the effect of signal leakage. The high sampling frequency prevents aliasing.

The discrete time samples $x[k]$ were transformed into the frequency domain with the use of the Fast Fourier Transform algorithm in MATLAB defined as

$$\underline{X}[n] = \sum_{k=0}^{N-1} \underline{x}[k]W^{kn} \quad n = 0, 1, \ldots, N - 1. \tag{D.1}$$

Herein $W = e^{(-2\pi i)/N}$, where N is the number of equal inter distant intervals of $x[k]$ [8]. The unit of $\underline{X}[n]$ is $[x]/Hz$. The estimator of the auto power spectral density is defines as

$$\hat{S}_{xx}[n] = \frac{1}{NT} \sum_{k-1}^{N} \underline{X}_k^*[n]\underline{X}_k[n] \tag{D.2}$$

Where $N = 20$ is the number of measurement samples, $\underline{X}_k^*[n]$ is the complex conjugate of $\underline{X}_k[n]$. The estimator of the cross power spectral density is defined as

$$\hat{S}_{xy}[n] = \frac{1}{NT} \sum_{k-1}^{N} \underline{X}_k^*[n]\underline{Y}_k[n] \tag{D.3}$$

where $\underline{Y}_k$ is another measurement sample. A estimation of the frequency response function $\hat{H}_{xy}$ from the hammer force to the displacement output was computed by using the H_1 estimator

$$\hat{H}_{xy} = \frac{\hat{S}_{xy}}{\hat{S}_{xx}}. \tag{D.4}$$

Herein, $\underline{X}$ was the Fourier transformed hammer force signal and $\underline{Y}$ the Fourier transformed displacement signal. The coherence is computed as follows

$$\gamma_{xy}^2 = \frac{|S_{xy}|^2}{S_{xx}S_{yy}}. \tag{D.5}$$

If the coherence is close to one this indicates that there is a strong linear relation between the input and the output [8].

The frequency response function from the model was obtained by simulating a sine-sweep. The force input of the simulation was a sine with a frequency starting at $10\ Hz$ until $1000\ Hz$ with steps of $5\ Hz$ and a amplitude of $0.1\ N$. Each frequency was simulated until the displacement showed a steady-state output. Then the harmonic displacement amplitude was stored and, in the same transient simulation, the frequency was increased with $5\ Hz$. This was done for all frequencies. The displacement amplitudes were divided by the sine amplitude resulting in the frequency response of the model.

Figure D.16 shows the frequency response of the measurement for the air bearing of table 5.1 with a mass of $3.6\ kg$ and a supply pressure of $4\ bar$ of the measurement and the model. It is seen that the increase in magnitude seen in the model data coincides well with the measurement data. The frequency of this increased magnitude is approximately $110\ Hz$. Besides the modeled magnitude

increase also several resonance peaks are seen in the measurements that are not modeled at 55 Hz, 65 Hz and 85 Hz. Further, a small deviation of approximately $1.3 \cdot 10^{-7} [m/N]$ in magnitude is noticed between the model and the measurements for low frequencies. This difference is probably due to a different static stiffness for the test setup and the model.

Figure D.17 plots the coherence of the measurement shown in figure D.16. As can be seen the coherence is equal to one at the location of the resonance at 110 Hz indicating that the measurement is reliable in this area. For high frequencies the coherence drops towards zero because of a bad signal to noise ratio. Below 110 Hz some drops in the coherence are seen indicating that the displacement output is not caused by the force input, or it is a non-linear effect. This is also seen in the coherence at the non-modeled resonance frequencies of 55 Hz, 65 Hz and 85 Hz.

To investigate if these peaks could be caused by non-linear effects in the air bearing a sine-sweep was modeled with a relative large amplitude of $20N$. The results of this sine-sweep is also shown in figure D.17. It is seen that the magnitude indeed increases at 55 Hz and 65 Hz but the increased magnitude at 110 Hz shifts to 100 Hz. This makes it improbable that the resonances observed at 55 Hz and 65 Hz exist due to non-linear effects.

The displacement sensors were placed above the bearing counter surface with two fixtures. The fixtures were again mounted on the large steel block (see figure **??**). On each fixture a acceleration sensor was placed next to the displacement sensor. Then the same measurements were performed with the modal hammer. Figure D.19 shows the frequency response of the modal hammer force to both fixture accelerations. It can be seen that the displacement sensors accelerate at 55 Hz, 65 Hz and 85 Hz. These are the same frequencies as the non-modeled resonances seen in figure D.16. It can be concluded that these resonance are caused by the moving displacement sensors and not due to movement of the bearing counter surface at these frequencies.

Figure D.20 shows the frequency response measurement for an air bearing with a mass of $M = 4.45\ kg$ and a supply pressure of $4\ bar$ and the corresponding model sine-sweep result. As can be seen the increased magnitude coincides well with the measurement. The error at the maximum magnitude value is $0.25 \cdot 10^{-7}\ m/N$. Again a difference is noticed in the magnitude for low frequencies of approximately $1 \cdot 10^{-7}\ m/N$. The resonance peaks due to the movement of the displacement sensors are also visible. The coherence shown in figure D.21 is equal to 1 at the increased magnitude and for low frequencies.

If figure D.20 is compared with D.16 it is noticed that the frequency of the increased magnitude has increased from 110 Hz to 115 Hz. for a linear system it is expected that the resonance frequency should decrease because of an increase in mass. However, because the mass has increased the static bearing height has decreased and from figure 5.13 it can be seen that the stiffness increased if the load is changed from 36 N to 44.5 N. This change in stiffness is higher than the change in mass resulting in an increase in the resonance frequency.

D.3.1 Additional frequency response measurement

The suggestion that the large resonance below the air bearing resonance were originating from the fixtures followed from a observation in a preliminary measurement. Figure D.22 shows the frequency response result with the hammer force as input and the displacement as output. As can be seen, two non-modeled resonances are visible at approximately 55 Hz and 65 Hz. The coherence, shown in figure D.23, only drops at the location of these resonance peaks and for higher frequencies. But, it is one at the location of the resonance peaks and at low frequencies. Figure D.25 shows the frequency response measurement of the hammer force to the acceleration of the counter surface. The resonances at 55 Hz and 65 Hz noticed in D.22 are not present in this measurement. Thus, these resonances are not present in the counter surface. This indicates that the displacement sensors are exhibiting this resonance.
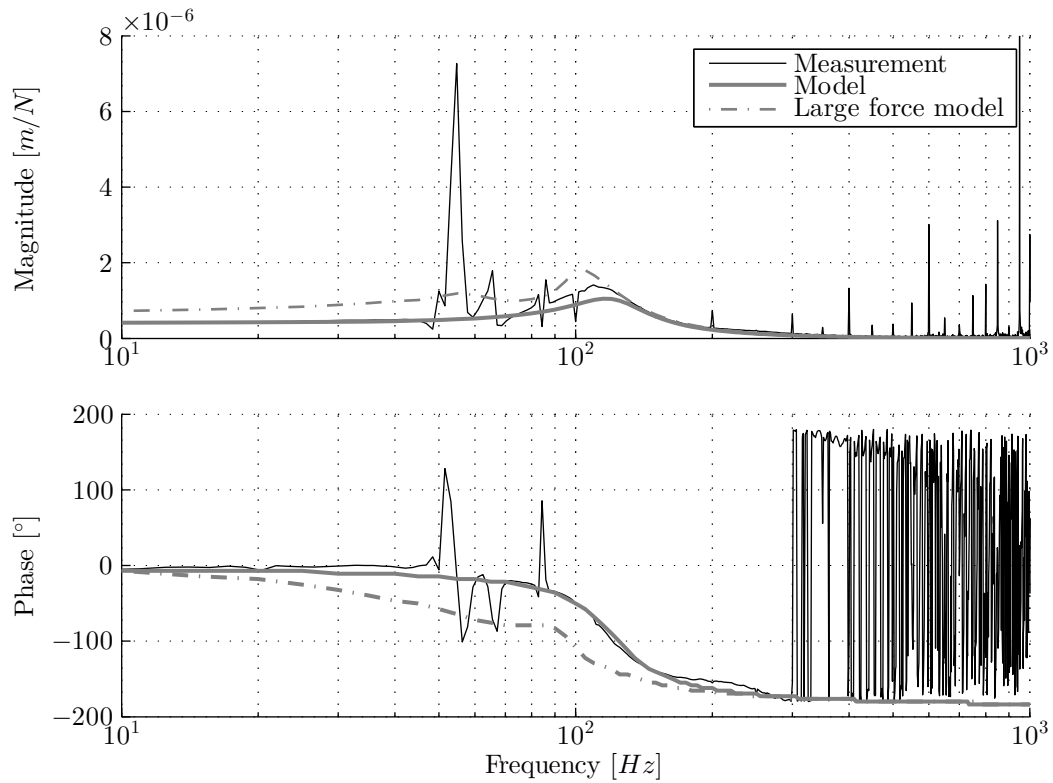
Figure D.16: Frequency response measurement from the force at the air bearing mass to the gap height for $p_s = 4\ bar$, $M = 3.6\ kg$.
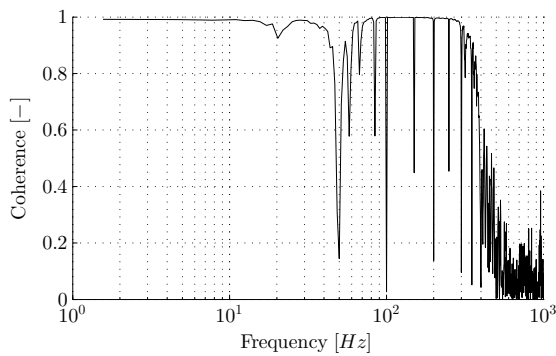

Figure D.17: Coherence of the frequency response measurement from the force at the air bearing mass to the gap height for $p_s = 4\ bar$, $M = 3.6\ kg$.
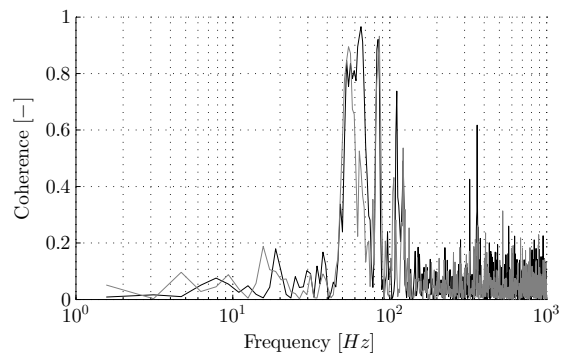
Figure D.18: Coherence of the frequency response measurement from the force at the air bearing mass to the acceleration of the fixtures.
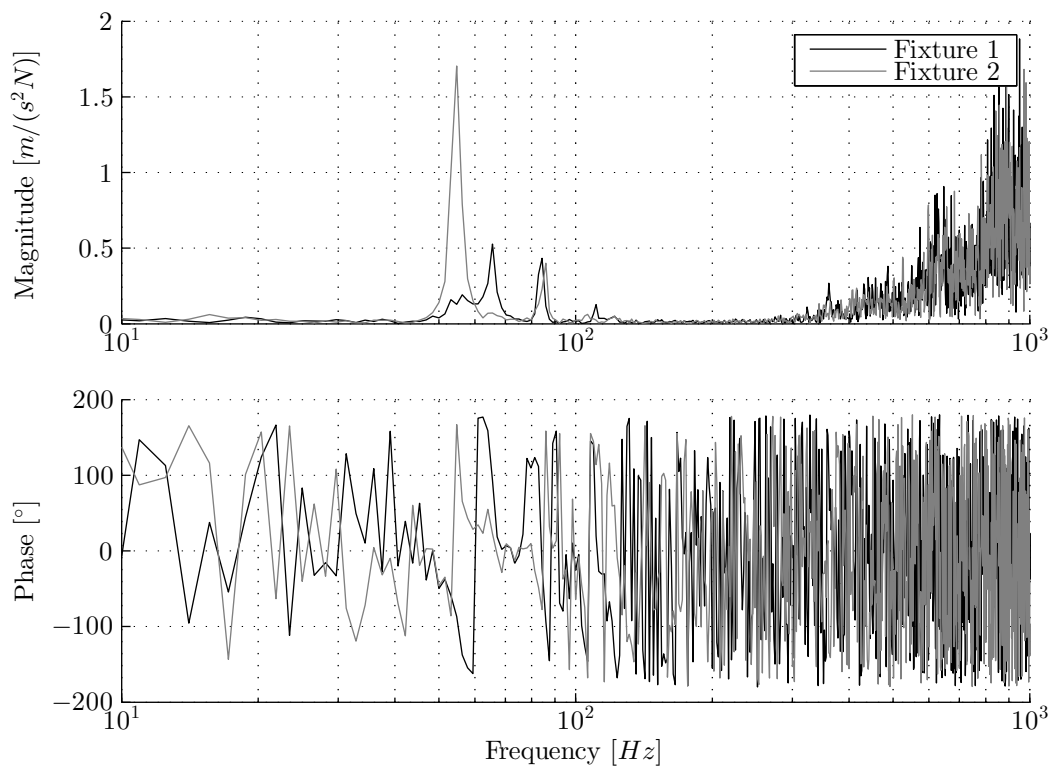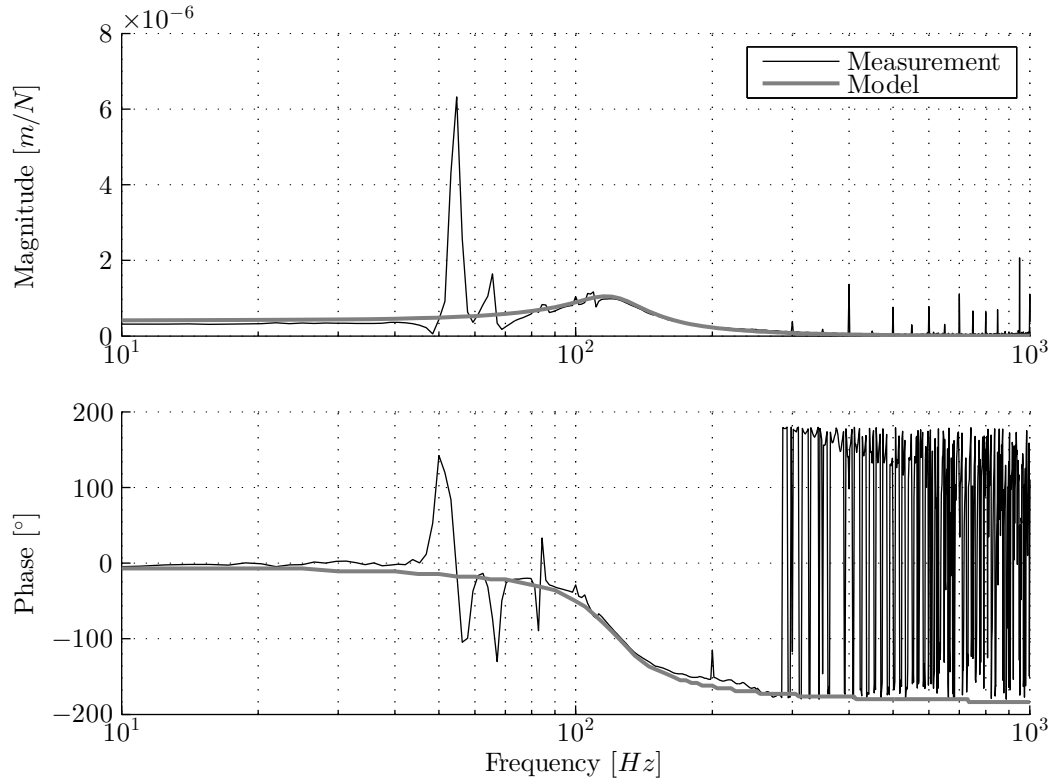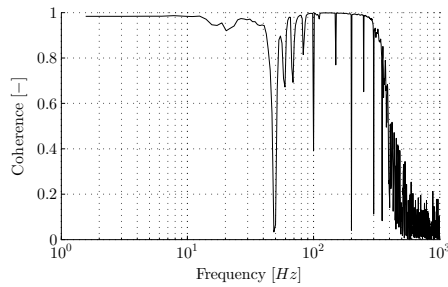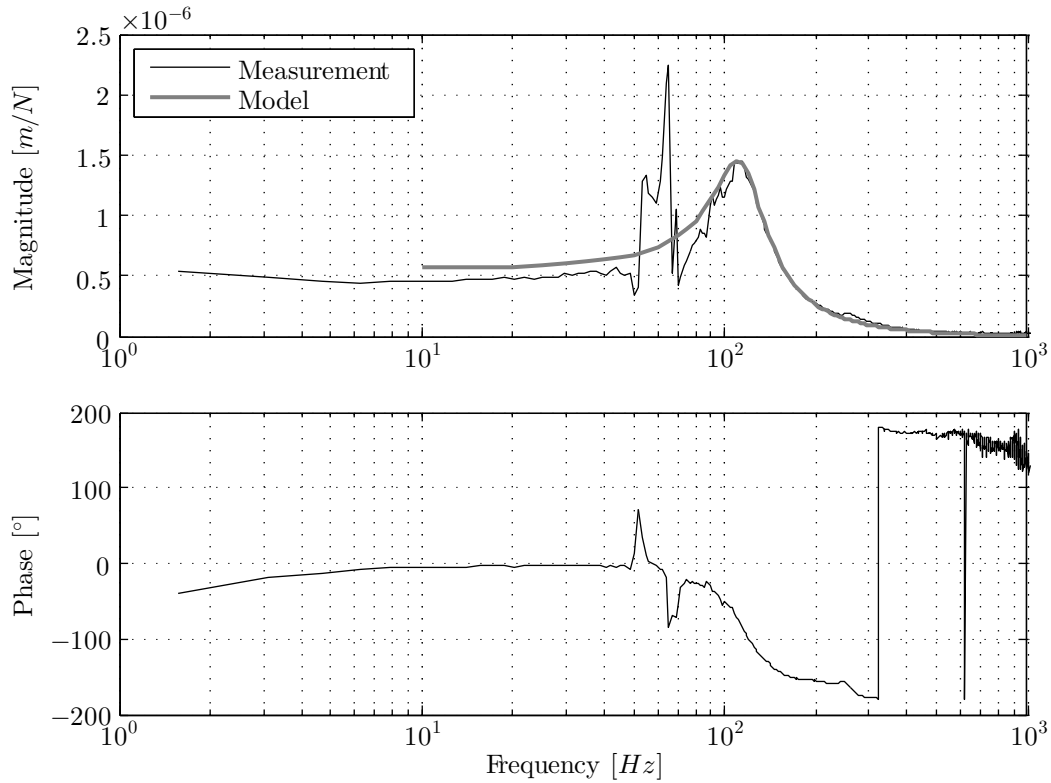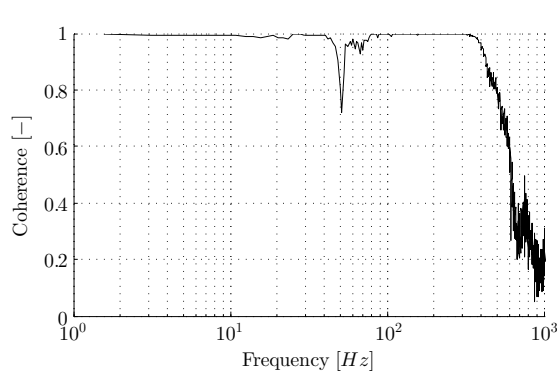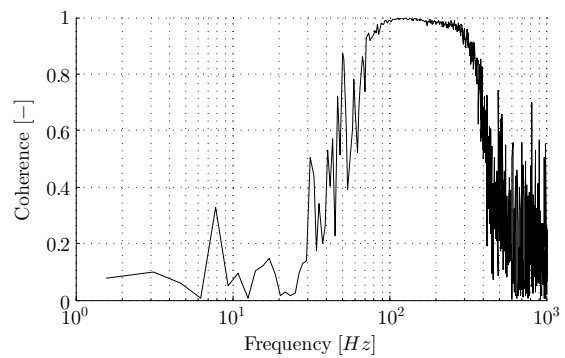
Figure D.19: Frequency response measurement from the force at the air bearing mass to the acceleration of the fixtures.

Figure D.20: Frequency response measurement from the force at the air bearing mass to the gap height for $p_s = 4\ bar$, $M = 4.45\ kg$.

Figure D.21: Coherence of frequency response measurement from the force at the air bearing mass to the gap height for $p_s = 4\ bar$, $M = 4.45\ kg$.

Figure D.22: Preliminary frequency response measurement from the force at the air bearing mass to the gap height for $p_s = 4\ bar$, $M = 3.6\ kg$.

Figure D.23: Coherence of the preliminary frequency response measurement from the force at the air bearing mass to the gap height for $p_s = 4\ bar$, $M = 3.6\ kg$.

Figure D.24: Coherence of the preliminary frequency response measurement from the force at the air bearing mass to the acceleration of the counter surface for $p_s = 4\ bar$, $M = 3.6\ kg$.
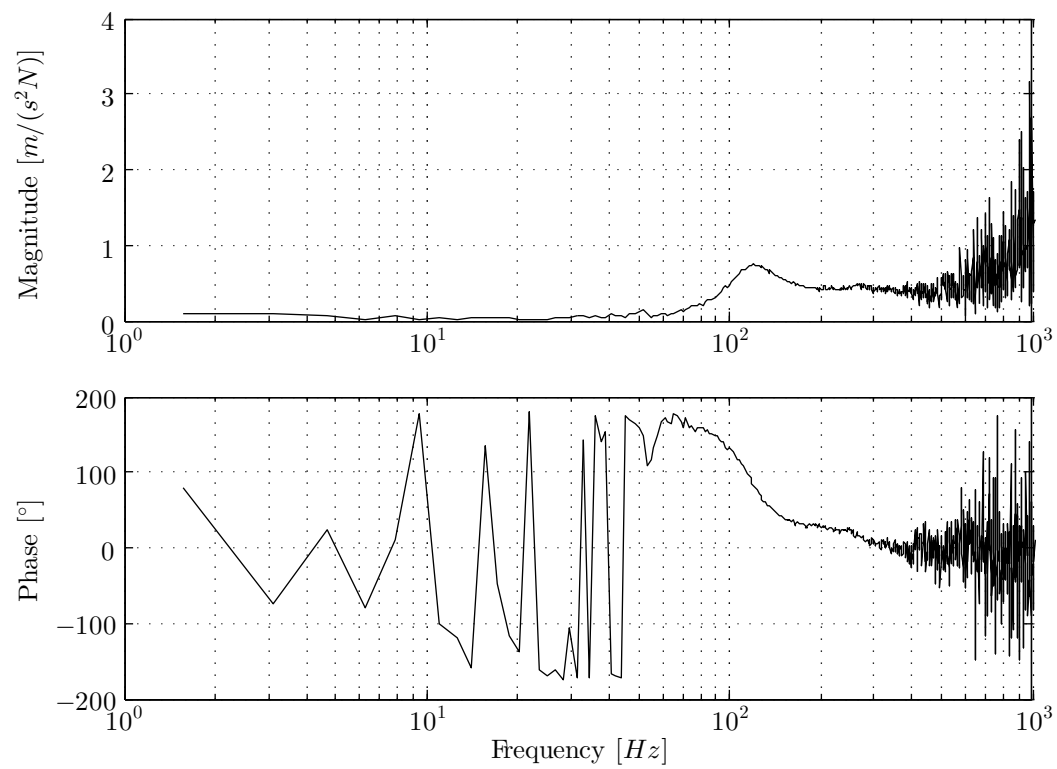
Figure D.25: Preliminary frequency response measurement from the force at the air bearing mass to the acceleration of the counter surface for $p_s = 4\ bar$, $M = 3.6\ kg$.

D.4   Eigenfrequency computation

Using the computed load capacity, the height dependent stiffness can be estimated. Together with the known mass an estimate of the eigenfrequency is made and this is compared with the harmonic results.
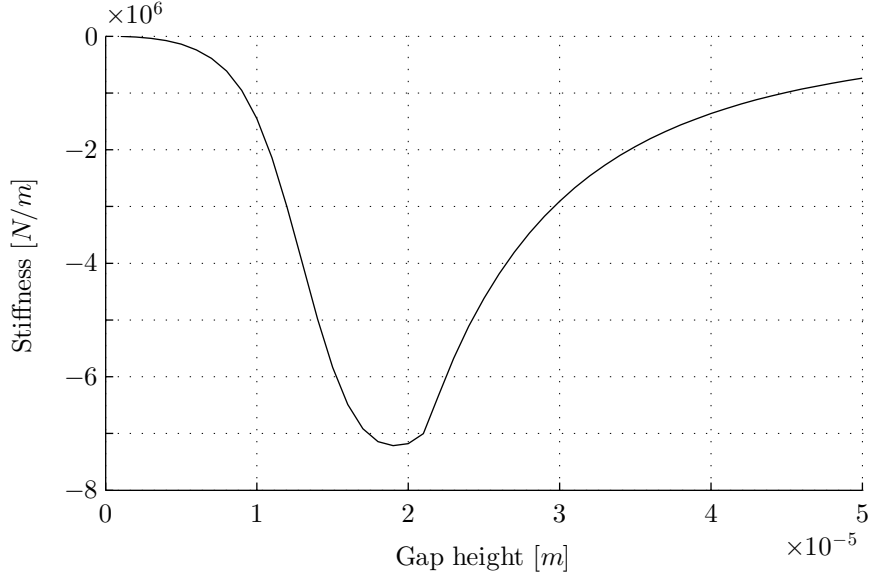
Figure D.26: Simulated stiffness of the air bearing used in the experiments with the Holster orifice model and a supply pressure of $p_s = 4\ bar$.

Figure D.26 shows the computed stiffness of the air bearing under consideration based on the Holster orifice model and a supply pressure of $4\ bar$. From Figure 5.4 it follows that the equilibrium gap height for a bearing mass of $3.6\ kg$ and $4.45\ kg$ is $3.6 \cdot 10^{-5}\ m$ and $3.2 \cdot 10^{-5}\ m$, respectively. Figure D.26 gives the according stiffness then as approximately $1.8 \cdot 10^{6}\ N/m$ and $2.5 \cdot 10^{6}\ N/m$, respectively. The eigenfrequency is computed using

$$f = \frac{1}{2\pi}\sqrt{\frac{S}{M}} \tag{D.6}$$

where S denotes the stiffness and M the moving air bearing mass. Using (D.6) gives, for the air bearing under consideration with the two different masses of $3.6\ kg$ and $4.45\ kg$, an eigenfrequency of $113\ Hz$ and $119\ Hz$, respectively.

If the system behaved linear, it is expected that the eigenfrequency will decrease if the mass increases. However, because in this example the stiffness increases because the gap height decreases due to the increased mass, the effect of the increased stiffness is larger than that of the increased mass. This results in an increased eigenfrequency as computed and seen in the harmonic experiments.

Appendix E

Sensitivity study

In the static load results it is seen that the measurement results are approximately 5 μm lower than the model results and that the trend of the measurements is changing at low gap heights. To investigate if this could be caused by variations of the air bearing parameters the sensitivity of the height at a certain load level is investigated for the different air bearing parameters. The case of a supply pressure of 4 bar is used and it is assumed that the air bearing is loaded with an external force of $F_{ex} = 120$ N because this is the force where the measurement trend starts to deviate from the model. The parameters investigated together with the nominal values are shown in table E.1. With these parameters the equilibrium height of the air bearing according to the model is 17.65 μm, while a height of approximately 12 μm was measured.

Figures E.1 till E.10 show the computed equilibrium heights for values of the investigated parameters that are varied plus and minus 10 % from the nominal values. The computed equilibrium height varies much, more than ± 0.5 μm, for the orifice radius R_1, air bearing radius R_2, supply pressure p_s and ambient pressure p_a. It should be considered that the air bearing radius R_2 was determined with an accuracy of $\pm 0.1 \cdot 10^{-3}$ m while the radius is measured as $\pm 3 \cdot 10^{-3}$ m. According to figure E.2 this measurement inaccuracy results in a maximum height variation of ± 0.04 μm and therefore it is unlikely that an variation in the air bearing radius will have a major contribution to the deviation seen between the model and the measurements. The same holds for the supply pressure p_s and the ambient pressure p_a. Considering figures E.3 and E.4 the sensitivity of these parameters is relatively large but the actual value of these pressures was determined within an accuracy of ± 0.02 bar resulting in a height deviation smaller than ± 0.2 μm. The orifice radius R_1 was hard to measure due to the out-of-roundness of the hole and the tapering of the edge resulting in a measurement accuracy of $\pm 0.1 \cdot 10^{-3}$ m and according to figure E.1 in a height variation of ± 0.4 μm.

Even tough the deviations for the supply pressure, ambient pressure and orifice radius are larger than that of the air bearing radius, none of the computed deviations is large enough to justify the 5 μm seen between the measurements and the model. This indicates that the deviation seen has another source. However, if this major error source can be traced and eliminated, then the sub micrometer deviations remaining could be justified due to parameter deviations between the model and the air bearing used in the experiments.

Table E.1: Parameters investigated in sensitivity study.

Parameter symbol	Value	Unit	Quantity
R_1	$2.5 \cdot 10^{-4}$	m	Orifice radius
R_2	$3 \cdot 10^{-2}$	m	Air bearing radius
p_s	$4 \cdot 10^5$	N/m^2	Supply pressure
p_a	10^5	N/m^2	Ambient pressure
T	293	K	Temperature
μ	$1.8205 \cdot 10^{-5}$	$kg/(ms)$	Viscosity
R_s	287	$J/(kgK)$	Specific gas constant
κ	1.405	$-$	Adiabatic expansion coefficient
C_{in}	0.9	$-$	Discharge coefficient at bearing gap inlet
C_{or}	0.8	$-$	Discharge coefficient of orifice
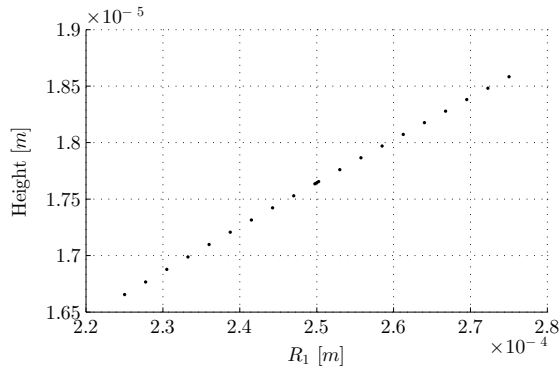
Figure E.1: Height as function of R_1 for $F_{ex} = 120\ N$.
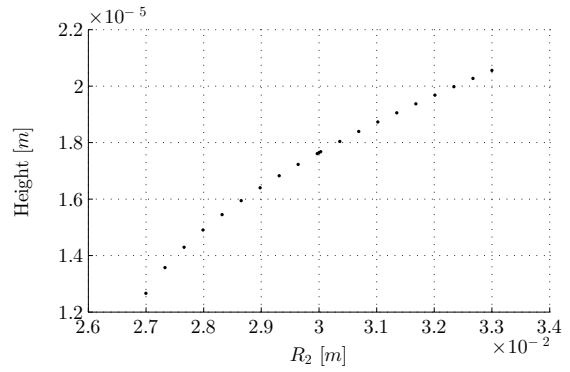
Figure E.2: Height as function of R_2 for $F_{ex} = 120\ N$.
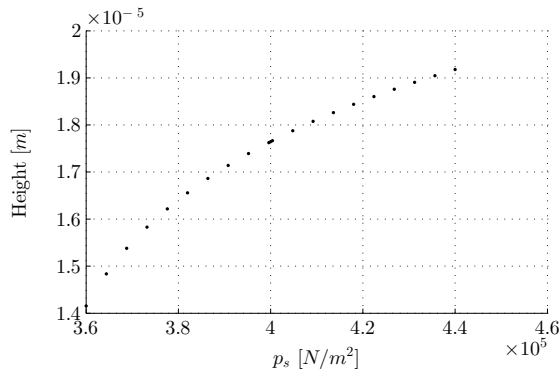
Figure E.3: Height as function of p_s for $F_{ex} = 120\ N$.
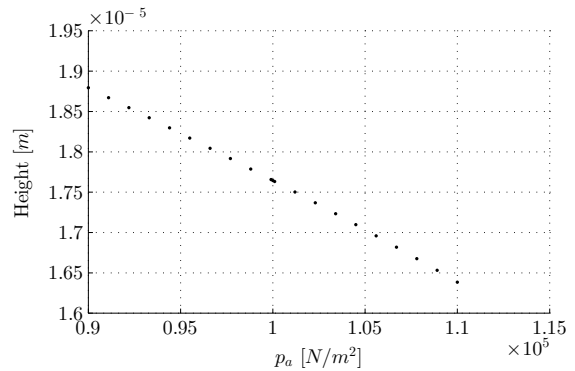
Figure E.4: Height as function of p_a for $F_{ex} = 120\ N$.
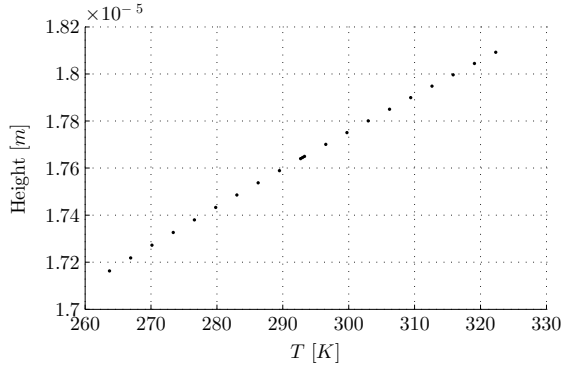
Figure E.5: Height as function of T for $F_{ex} = 120\ N$.
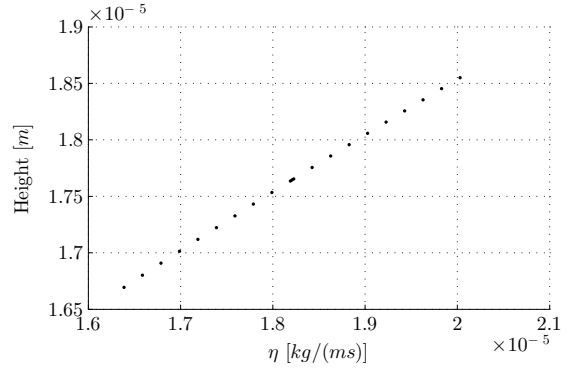
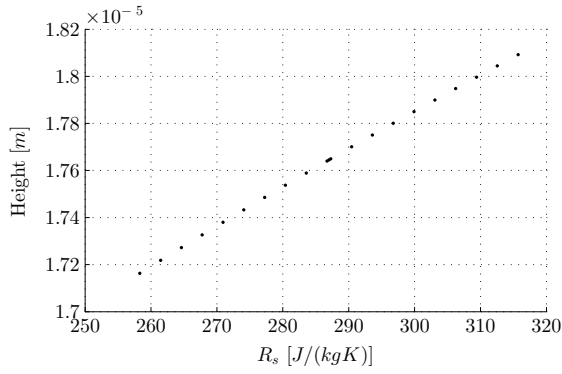Figure E.6: Height as function of η for $F_{ex} = 120\ N$.

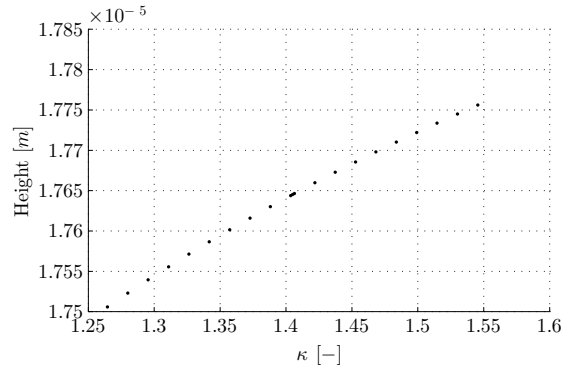Figure E.7: Height as function of R_s for $F_{ex} = 120\ N$.

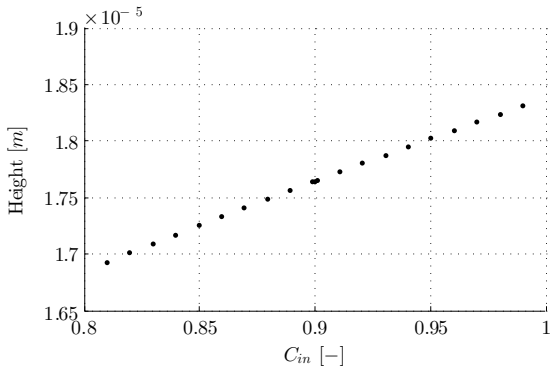Figure E.8: Height as function of κ for $F_{ex} = 120\ N$.

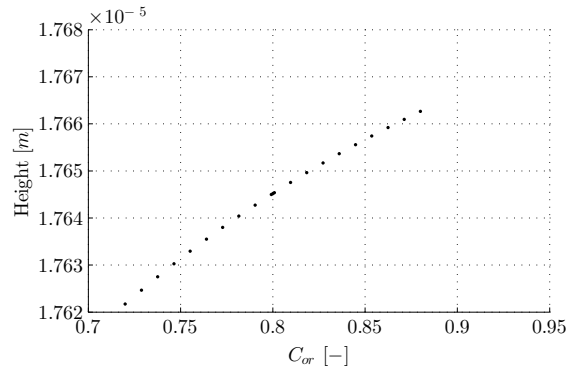Figure E.9: Height as function of C_{in} for $F_{ex} = 120\ N$.

Figure E.10: Height as function of C_{or} for $F_{ex} = 120\ N$.

Appendix F

Interpolated coefficients method

An often used method to assess the dynamic stability of air bearings is to compute the frequency and gap height dependent stiffness and damping coefficients. If the these coefficients are known for a certain gap height the dynamic stability can be assessed by assessing the sign of the damping [9]. For a full assessment the dynamic coefficients have to be computed for multiple gap heights in the working range of the bearing. If these dynamic coefficients in the work range are know, they can be used to compute a transient trajectory of the gap height. In the following the method to compute this transient trajectory is briefly elaborated.

F.1 Transient gap height simulation

The dynamic coefficients of the air bearing for a certain gap height are obtained by assuming a harmonic variation on the pressure and height in the Reynolds equation. The Reynolds equation is then linearized and solved. This results in a static pressure distribution P_0 and a dynamic pressure distribution often denoted by P_1. The static or dynamic load capacity is computed by integrating the corresponding pressure along the bearing area:

$$W_q = \int_A P_q dA, \quad q = \{1, 2\}. \tag{F.1}$$

The frequency dependent dynamic stiffness consist of a real and imaginary part

$$\frac{W_1(\omega)}{h} = K(\omega) = S(\omega) + j\omega B(\omega). \tag{F.2}$$

where $S(\omega)$ is the stiffness coefficient and $B(\omega)$ the damping coefficient.
Figure F.1 and F.2 shows the stiffness and damping coefficients computed with the above described method with the parameters presented in table F.1. To obtain these results the above described method is applied in a FEM Sepran routine developed by Philips.
The total bearing force of the linearized Reynolds equation is

$$W_{tot} = W_0 + W_1\left(\frac{dh}{dt}, h\right). \tag{F.3}$$

This can be rewritten to

$$\begin{aligned} W_{tot} =& W_0 + W_1 \\ =& W_0 + K(\omega)h \\ =& W_0 + S(0, h) \cdot h + \left(B(\omega, h) - \frac{S(\omega, h) - S(0, h)}{\omega} j\right) \frac{dh}{dt}, \\ =& W_s(h) + W_{dv}\left(\frac{dh}{dt}, h, \omega\right). \end{aligned} \tag{F.4}$$
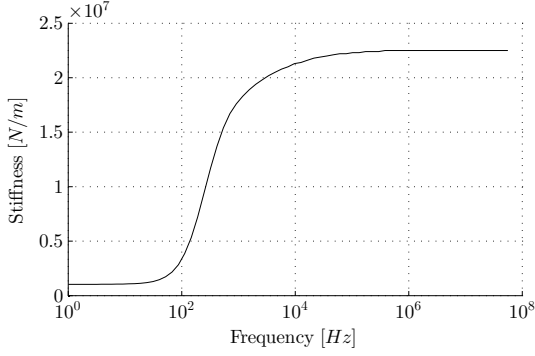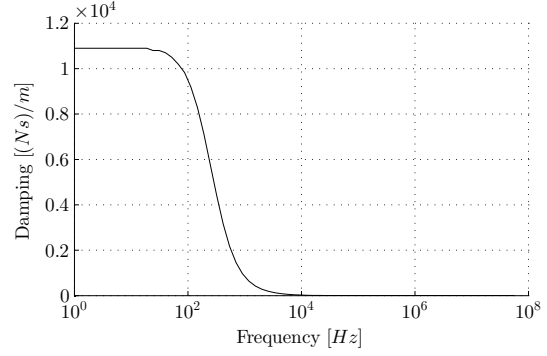

Figure F.1: Frequency dependent stiffness for $h = 25 \ \mu m$.

Figure F.2: Frequency dependent damping for $h = 25 \ \mu m$.

Table F.1: Model quantity values used in simulations.

Parameter symbol	Value	Unit	Quantity
R_1	$2 \cdot 10^{-4}$	m	Orifice radius
R_2	$4 \cdot 10^{-2}$	m	Air bearing radius
p_s	$2 \cdot 10^5$	N/m^2	Supply pressure
p_a	10^5	N/m^2	Ambient pressure
T	293	K	Temperature
μ	$1.8205 \cdot 10^{-5}$	$kg/(ms)$	Viscosity
R_s	287	$J/(kgK)$	Specific gas constant
κ	1.405	$-$	Adiabatic expansion coefficient
M	3.5	kg	Air bearing mass
g	9.81	m/s^2	Gravitational constant
I	1000	$-$	Number of intermediate spatial intervals
J	1000	$-$	Number of intermediate time intervals
t_{end}	0.035	s	End time of simulation

where

$$W_s(h) = W_0 + S(0, h) \cdot h \tag{F.5}$$

and

$$W_{dv}\left(\frac{dh}{dt}, h, \omega\right) = \left(B(\omega, h) - \frac{S(\omega, h) - S(0, h)}{\omega} j\right) \frac{dh}{dt}. \tag{F.6}$$

W_{dv} can be approximated by a first order model given as

$$W_{dv,a} = \left(\frac{B(0, h)}{1 + \frac{B(0,h)}{S(\infty, h) - S(0, h)} s}\right) \frac{dh}{dt}. \tag{F.7}$$

This can be written as a first order differential equation

$$\frac{dW_{dv,a}}{dt} \frac{B(0, h)}{S(\infty, h) - S(0, h)} + W_{dv,a} = B(0, h) \frac{dh}{dt} \tag{F.8}$$

$B(0, h)$, $S(0, h)$ and $S(\infty, h)$ are the asymptotic values of the curves as for example shown in figures F.1 and F.2. These are determined for several gap heights in the working range of the air bearing. Figures F.3 till F.5 show the computed gap height dependent coefficients and load capacity for different gap heights for the air bearing under consideration in this chapter.
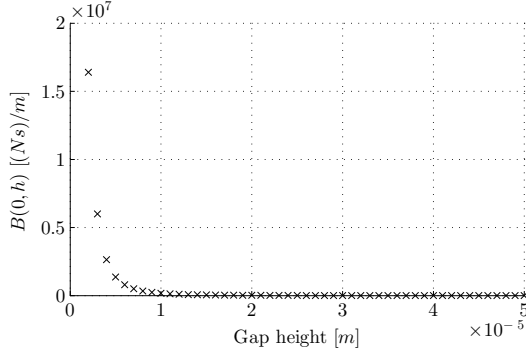
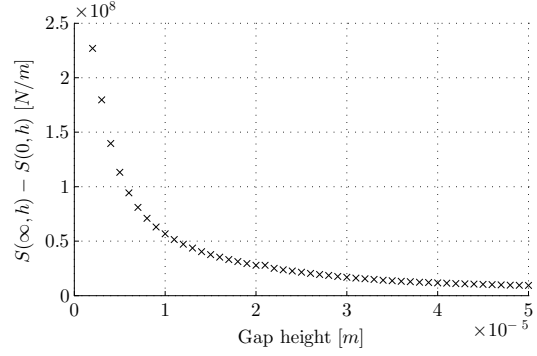Figure F.3: Height dependent damping coefficient.

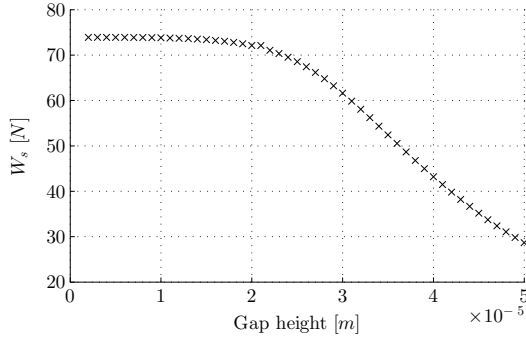Figure F.4: Height dependent stiffness coefficient difference.

Figure F.5: Height dependent load capacity.

The following air bearing model can now be defined

$$M\frac{d^2h}{dt^2} = W_{tot,a} + F_{gravity} + F_{external},$$ (F.9)

where

$$W_{tot,a} = W_s(h) + W_{dv,a}\left(\frac{dh}{dt}, h, \omega\right),$$ (F.10)

$$F_{gravity} = Mg$$ (F.11)

and

$$F_{external} = f(t).$$ (F.12)

Equation (F.9) is solved with a forward integration method resulting in a solution for the gap height $h(t)$. In this study the tool MATLAB Simulink was used. Herein the computed coefficients and load capacity as shown in figures F.3 till F.5 were stored in lookup tables and the data was interpolated to obtain the desired height dependent coefficients during the simulation in MATLAB Simulink.

F.2 Simulation results

In this section the simulation results of the non-linear model, linear model and the model with interpolated coefficients are compared. The linear model uses the dynamic coefficients of the initial

height and these are not adapted if the gap height changes. Figure F.7 shows the force "impulse" defined for this simulation with amplitude $\hat{F}$ and duration t_{im}. Other model parameters are presented in table F.1.

Figure F.6 shows the gap height response for the air bearing subjected to an impulse with $\hat{F} = 15\ N$ and duration $t_{im} = 0.01\ s$. As can be seen the interpolated coefficients model coincides well with the developed non-linear model. The initial height between the interpolated coefficients model and the non-linear model has an error of $0,3\ \mu m$. The dynamic coefficients were determined with the use of an air bearing model developed by Philips that uses the method described above. This difference in initial height is probably caused by different assumptions and numerical techniques between the models. Because of this difference in initial height the error between the maximum response amplitudes is considered. This is defined as the distance form the initial height until the minimum value of the height response. The error in the maximum amplitude between these two models is 0.34 μm. This is approximately 4 % of the maximum response amplitude. The error in the maximum response amplitude between the non-linear and the linear model is approximately 1.2 μm. This is a factor four larger than the error between the non-linear model and the interpolated coefficients method.

Figure F.8 plots the height response for the air bearing subjected to an impulse with $\hat{F} = 100\ N$ and duration $t_{im} = 0.01\ s$. As can be seen, the gap height of the linear model becomes negative. In practice this would mean that the two bearing surfaces would collide. However, the gap height response of the non-linear model an interpolated coefficients method has a minimum gap height of 17 μm. Further, the error in the maximum amplitude response is 0.1 μm which is about 0.3 %. Based on these results it can be concluded that the linear model deviates much from the non-linear model, especially for large displacements as expected. The interpolated coefficients model shows a good correspondence with the non-linear model. In the obtained results it is seen that the error in the maximum amplitude response for the impulse forces modeled is smaller than 4 %. Further, the simulations imply that the air bearing considered is able to withstand impulse force larger than the maximum load capacity. This would not be concluded if only the linear model was used.
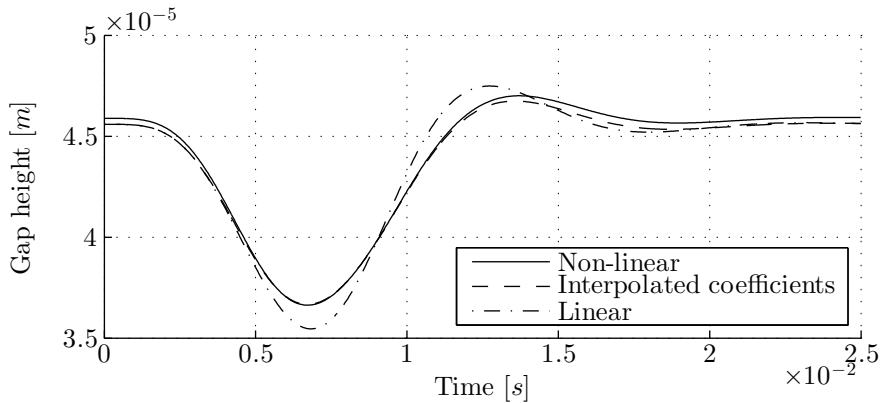

Figure F.6: Gap height response for air bearing model subjected to an impulse with $\hat{F} = 15\ N$ and $t_{im} = 0.01\ s$.
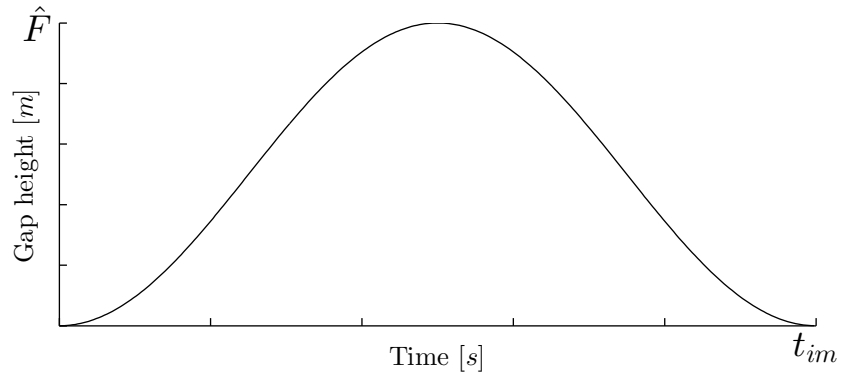
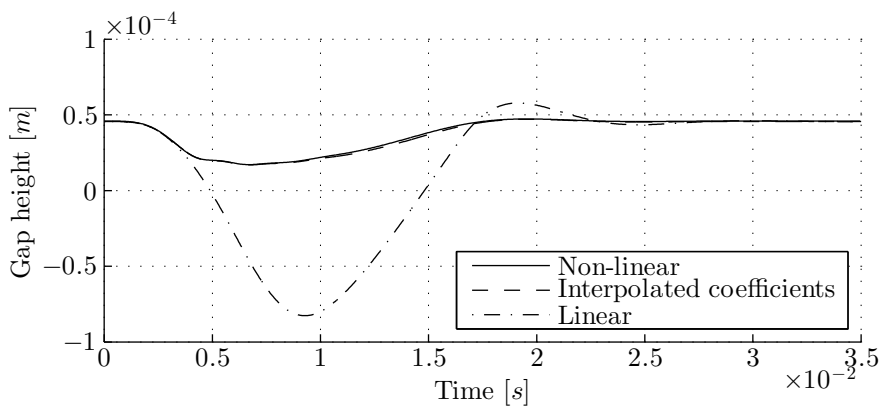Figure F.7: Force impulse with amplitude $\hat{F}$ and duration t_{im}.

Figure F.8: Gap height response for air bearing model subjected to an impulse with $\hat{F} = 100\ N$ and $t_{im} = 0.01\ s$.